LINKING ELASTIC AND PETROPHYSICAL PROPERTIES ASSOCIATED WITH DEFORMATION BANDS

A Thesis Presented to the Faculty of the

Department of Earth and Atmospheric Sciences

University of Houston

In Partial Fulfillment

of the Requirements for the Degree

Master of Science

By

Anna Khadeeva

May 2014

LINKING ELASTIC AND PETROPHYSICAL PROPERTIES ASSOCIATED WITH DEFORMATION BANDS

_____

Anna Khadeeva

APPROVED:

_____

Dr. Michael Murphy, Chairman

_____

Dr. De-hua Han

_____

Dr. Alexander Robinson

_____

Dr. Nicholas Boyd

_____

Dean, College of Natural Sciences and Mathematics

ACKNOWLEDGEMENTS

I would like to thank my Thesis Committee, Dr. Michael Murphy, Dr. De-hua Han, Dr. Nicholas Boyd and Dr. Alexander Robinson, for help and supervision.

During the course of my thesis, I have conducted the field work in New Mexico and have been lucky to spend the time with Dr. Michael Murphy, Yiduo Liu, Kevin O'Keeffe and other members of our group to figure out the geology of the area and set up my experiment. Thank you for your input and help.

I also want to thank the people at UH Rock Physics Lab for providing lab and field equipment and teaching me how to operate it.

Finally, I wish to thank my family for encouraging me to pursue this degree and, particularly, my mother, an amazing petrophysicist, who has helped me make sense out of some of my research findings.

LINKING ELASTIC AND PETROPHYSICAL PROPERTIES ASSOCIATED WITH DEFORMATION BANDS

An Abstract of a Thesis Presented to the Faculty of the

Department of Earth and Atmospheric Sciences

University of Houston

In Partial Fulfillment

of the Requirements for the Degree

Master of Science

By

Anna Khadeeva

May 2014

ABSTRACT

Deformation bands are common structures in faulted porous sandstones and are interpreted to represent zones where petrophysical properties within the band are different from the host rock. Porosity within the deformation band may be enhanced or reduced depending on the band type. Previous studies show that porosity has a negative correlation with rock velocity. This study investigates the relationship between velocity and porosity of sandstones that contain zones of deformation bands. It aims to provide the connection between petrophysical and elastic properties associated with deformation bands. This work incorporates outcrop studies as well as field and laboratory measurements of Jurassic Entrada sandstone in north-central New Mexico. Thin section observations of the deformation bands from the study area show that the bands consist of mostly quartz grains and have the same mineralogical composition as the surrounding rock. The porosity within the band is reduced relative to the surrounding rock. The decrease in size and sorting of the grains within the band is also observed. Previous workers, who have described the deformation bands with similar properties, have explained the formation of these deformation bands through the process of cataclasis which involves grain crushing. To test this assumption, an investigation of the pressure required to crush a quartz grain from published laboratory experiments along with the estimation of regional stresses at the time of the deformation bands' formation in this study area were conducted. From these estimations, it was concluded that the pressures generated during the formation of deformation bands in the study area are insufficient to cause cataclasis. Therefore, an alternative explanation of low-porosity deformation bands' formation under low pressure conditions is proposed in this work. Modeling of rock velocity variation with porosity was performed using the core samples measurements from the study area. The obtained models were used to estimate porosity from acquired outcrop velocity data. Unlike laboratory data, some of the measured outcrop velocities exhibit

anisotropy, meaning the velocity depends on the measurement orientation, associated with the dominant strike direction of deformation bands. Therefore, a correction for the anisotropy observed in these field measurements was applied to the above models.

TABLE OF CONTENTS

FIGURES

1. INTRODUCTION

1.1 Background and Motivation

Deformation bands are the structures that form due to rock displacement along a zone of strain localization and are abundant in faulted porous sandstones. The displacement generated over each deformation band is millimeters to several centimeters thick (Aydin, 1978; Antonellini and Aydin, 1995; Du Bernard et al., 2002a). Deformation band types can be differentiated based on mineral composition, depth of burial, formation fluids and kinematic processes responsible for the formation of the band. The type of a band affects rock porosity and permeability (Fossen et al., 2007). Knowledge of deformation band types and their associated petrophysical properties in conjunction with their orientations and distribution helps determine fluid paths and accumulations within the formation. Such information is useful in hydrocarbon or groundwater exploration for guiding well placement.

The seismic method, which relies on velocity and density contrasts between rock interfaces, is commonly used for subsurface mapping and inferring the rock properties away from wells. Rock porosity is closely associated with velocity. Numerous empirical relationships of linking velocity with porosity have been established in sandstones (e g., Han et al., 1986; Vernik, 1997). Since the porosity within a deformation band changes relative to the surrounding rock, the change in rock velocity associated with deformation bands is expected to be observed.

Seismic anisotropy attributes generated by processing wide-azimuth seismic surveys are used as a common practice in fracture orientation detection (e g., Rich and Ammerman, 2010; Wild, 2011). Anisotropy attributes allow one to visualize horizontal anisotropy (HTI) associated with dominant fracture orientation (Figure 1.1). Velocity decreases as a seismic wave passes through the fracture and is slower perpendicular to the dominant fracture strike. The same

principle is expected to work when applied to deformation bands' detection where different velocities perpendicular and parallel to these features should be recorded.

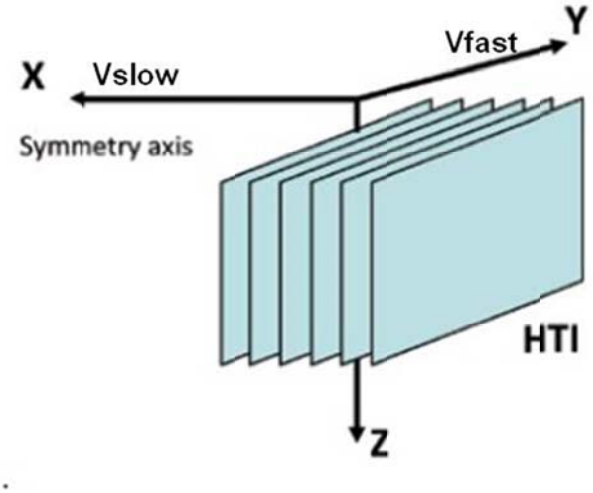

Figure 1.1: HTI anisotropy associated with fractures. Fast velocity is observed parallel to fracture swarms (modified from Wild, 2011).

1.2 Previous Velocity-Porosity Analysis of Sandstones with Deformation Bands

Fredericks et al. (2013) attempted to measure velocity and porosity changes associated with deformation bands in the outcrop and compared them with laboratory data from the same rock. The outcrop data and core samples were collected in different parts of the fault zone. The samples were cored parallel and perpendicular to bedding. A decrease in velocity and an increase in porosity is observed in the direction away from the fault. The range of P-wave velocities under 70 MPa confining pressure were measured between 3500 - 4500 m/s. Velocities perpendicular to bedding are similar or slightly higher than velocities parallel to bedding. The observed field P-wave velocities, however, are significantly lower (600 - 1500 m/s) than the lab measurements and do not correlate with porosity or distance from the fault. The experimental setup for velocity acquisition in the field (Figure 1.2) shows the source and two receivers in line with the source inserted into pre-drilled holes. The issue with such a setup is that it does not insure a complete

instrument coupling with the formation since the hole where the sensor is inserted is wider than the sensor. As a result, the field velocities may be affected by the presence of air between the instrument and formation. An additional reason for the inconsistency between field and laboratory velocity measurements is the confining pressure difference between these two measurements. An increase in confining pressure is known to affect the velocity as the microcracks close under higher pressure which leads to the velocity increase (Khaskar et al., 1999). The laboratory data measured at high confining pressure cannot be directly compared with field results as the confining pressure of a rock exposed to the surface is close to zero. Lab velocities are, therefore, likely to be higher compared to field velocities.

Figure 1.2: Experimental setup for field velocity acquisition in Fredericks et al (2013). Observed lower field velocities could be due to the poor instrument coupling with the formation.

Laboratory data provided by Fredericks et al. (2013) captures changes in velocity and porosity with distance from the fault. Higher porosity and lower velocity are observed in undeformed samples compared to the samples near the fault that exhibit deformation bands. Core

samples are measured parallel and perpendicular to the bedding of the strata where some of the samples perpendicular to bedding show slightly higher velocities. The field velocity measurements are not consistent with laboratory data, possibly due to the experimental setup.

Two issues that are of interest to the current research are identified from the study by Fredericks et al. (2013):

1) The acquired field velocities of rocks do not reflect the velocities measured in laboratory. How to set up an experiment to be able to obtain similar results in field and laboratory conditions?
2) The difference in porosity and velocity between the samples containing deformation bands and the samples of undeformed rock is observed. For the samples containing deformation bands, is there a difference in porosity and velocity parallel and perpendicular to the deformation bands' strikes?

1.3 Research Objectives

The focus of this thesis study is the distribution of deformation bands associated with faulting in the Jurassic Entrada sandstone and their effects on petrophysical properties and velocity of the rocks. The study area is located in Abiquiu Embayment, north-central New Mexico, next to the Cañones fault zone. The study incorporates the following topics:

1) Geologic setting in the study area is addressed in Chapter 2. This chapter reviews the tectonic history of Abiquiu Embayment in relation to the main structures observed in the study area, Cañones fault and monocline. Stratigraphy of the area is reviewed to establish the maximum burial depth of Entrada sandstone.
2) Types of deformation bands and their effect on petrophysical properties are reviewed in Chapter 3. Deformation bands can be either barriers or conduits for fluid flow depending on

their type. An overview of the previously published data is used to define the types of deformation bands and conditions for their formation (burial depth, mineralogic composition, pore fluids). Thin sections of deformation bands in the study area are examined to establish their effect on porosity and permeability.

3) Deformation bands' distribution in the damage zone are discussed in Chapter 4. Fault architecture models where deformation band density and distribution depends on the spatial position relative to the fault slip are introduced. The common features of the fault zones from different published examples are highlighted and compared with acquired deformation band density from the study area.
4) Velocities associated with deformation bands and their link with petrophysical properties from core samples are presented in Chapter 5. Ultrasonic velocity measurement system is described in Appendix A. It ensures a good coupling with formation for in-situ velocity measurements. Obtained velocities are analyzed to determine anisotropy associated with deformation bands. Velocity – porosity trends for the area are established with the help of the model by Vernik and Kachanov (2010). The obtained relationships are used to predict porosity for the in-situ velocity measurements. The relationship between porosity and velocity in core samples are discussed.

Provided analysis of the above outcrop example will serve as a proxy for detection of deformation bands using seismic techniques and prediction of their petrophysical properties from core data.

2. GEOLOGY OF ABIQUIU EMBAYMENT

2.1 Tectonic Setting

The Abiquiu Embayment is bordered by Colorado Plateau to the northwest and Española Basin to the southeast (Figure 2.1). The study area is located on the western margin of Abiquiu Embayment near the Cañones fault zone and is affected by two major tectonic events.

The oldest structures in the area are related to the Laramide Orogeny that initiated 80 - 75 Ma in the Rocky Mountains and continued up to Southern Cordillera where it ended at 35 Ma (Magnani et al., 2005). The prominent Laramide features in the form of thrust faults, folds, and arches striking N-S and NW are observed in San Juan Basin and Sangre de Cristo Mountains north of Abiquiu Embayment (Magnani et al., 2005; Erslev and Koenig, 2009). Laramide-age structures observed in Abiquiu Embayment are not as large and extensive as the ones found to the north. However, they guided later Rio Grande extension where many of the normal faults were initiated along preexisting planes of weakness. Some of the normal faults in the Rio Grande basin area are reactivated Laramide thrust faults (Wawrzyniec et al., 2002; Ingersoll, 2001).

Rio Grande rifting began around 29 Ma, spanning from central Colorado to southern Mexico. The rift consists of N-S elongated en echelon basins where the Abiquiu Embayment is the shallow northwestern edge of Española Basin (Golombek et al., 1983; Biehler et al., 1991; Baldridge et al., 1994). The Abiquiu Embayment is separated from Española Basin by the Embudo transfer zone that strikes ENE. The faulting in Abiquiu Embayment is said to have been active between 10 and 7 Ma (Baldridge et al., 1994).

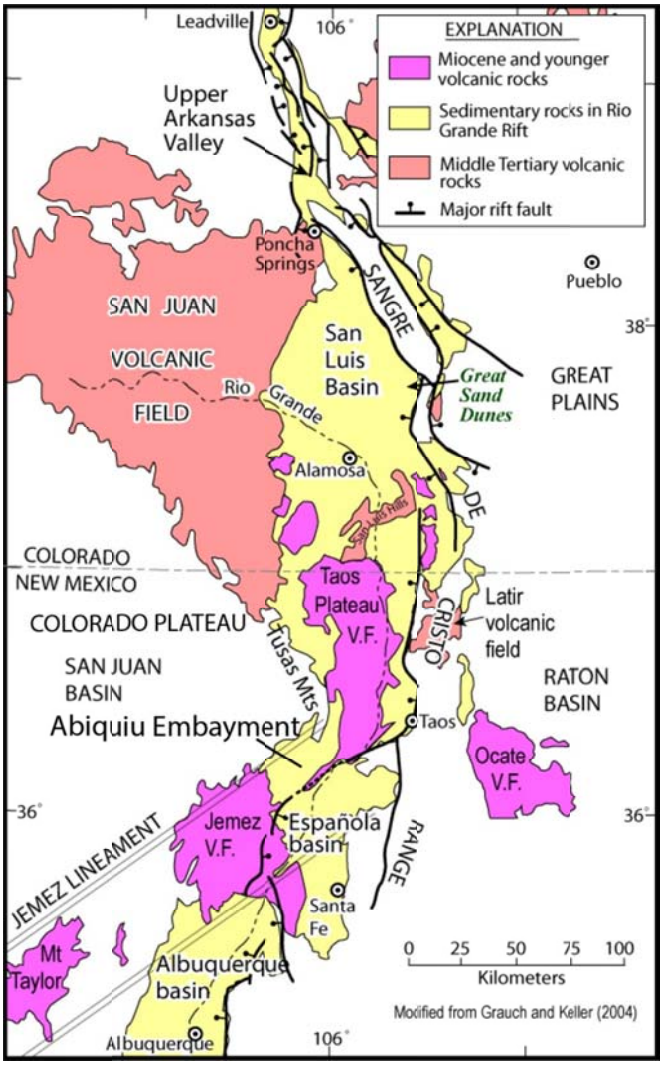

Figure 2.1: General geology and location of Abiquiu Embayment relative to the main sedimentary basins in the area (Modified from USGS Crustal Geophysics and Geochemistry Center, 2013).

A base map with the structures observed in the vicinity of the study area is shown in Figure 2.2. The features not mappable on this scale are shown in blue dots, and their orientations are summarized in Table 2.1. The Cañones fault located in the western corner of Red Wash Canyon is a normal fault related to Rio Grande extension. The strike of the fault measured in the study is approximately N40E which is consistent with previously published data (Maldonado, 2008). A photograph of Cañones fault outcrop in the study area is shown in Figure 2.3. The hanging wall is shown to the left of the white dashed line and incorporates Jurassic rocks of Entrada (Je) sandstone and Todilto (Jt) limestone. The footwall is the Permian Cutler formation (Pcu).

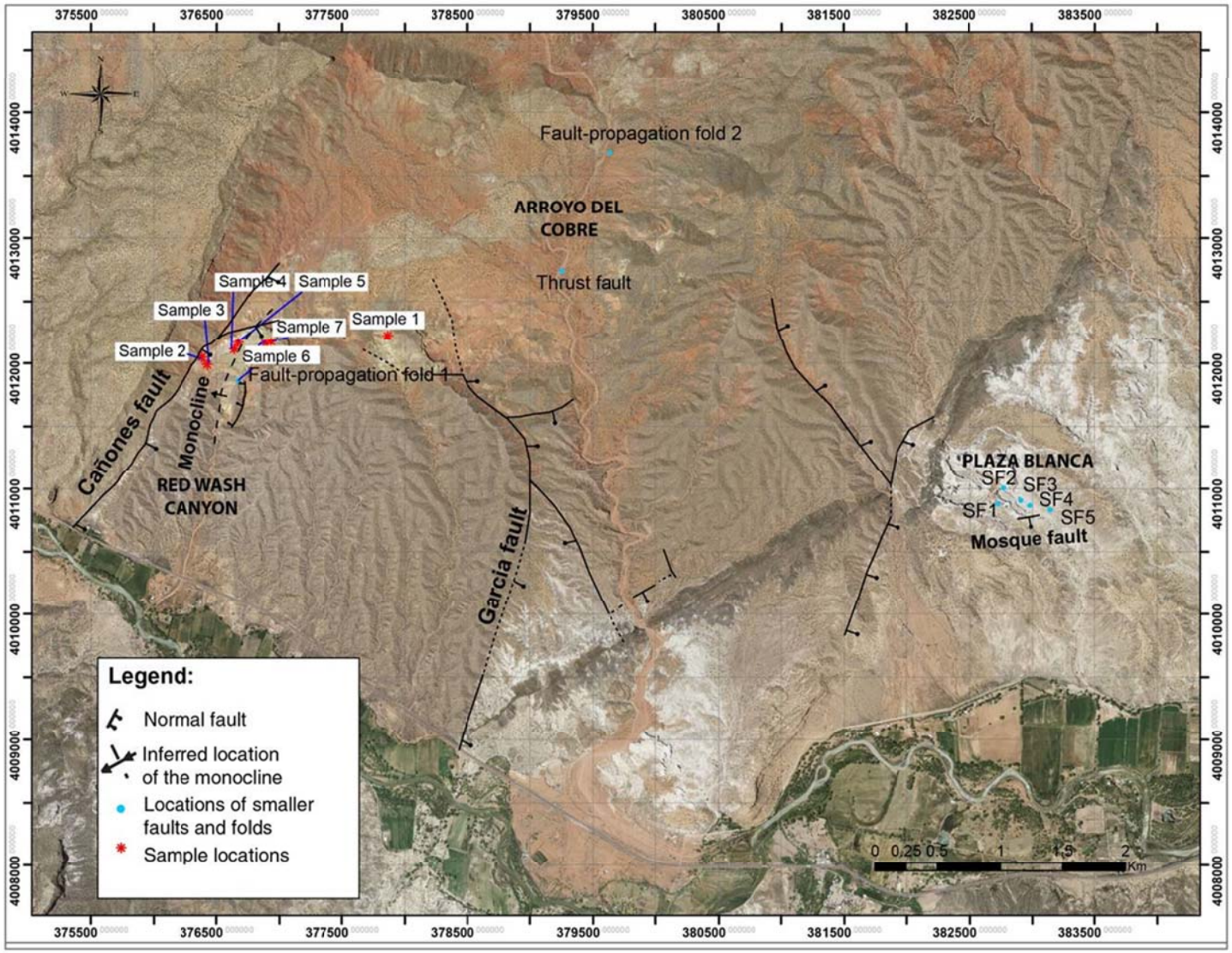

Figure 2.2: Base map of the study area with the structures (faults and folds) and core sample points locations. The structures are dipping NE and NW. The numbers placed vertically and horizontally are the Universal Transverse Mercator (UTM) 13N coordinates defining northing and easting with respect to World Geodetic System (WGS) 84.

Figure 2.3: Photograph of Cañones fault outcrop where Jurassic and Permian units are juxtaposed. Jurassic Entrada sandstone (Je) and Todilto limestone (Jt) are in the hanging wall of the fault. The footwall of the fault is the Permian Cutler formation (Pcu). View is to the south. A person on the hanging wall side of the fault is used for scale.

The other structures related to Rio Grande rifting are the normal faults located to the east of Cañones fault including Garcia fault that strikes about N15E, the Mosque fault which has an attitude of N80E/60SE and smaller faults in Plaza Blanca (Figure 2.2). The major Laramide-age structure is the monocline running subparallel to the Cañones fault in the Red Wash Canyon, the inferred hinge of which has a strike of N10E and is marked with a dashed black line in Figure 2.2. The outcrop of the monocline is shown in Figure 2.4 where approximately 30 m of Entrada sandstone overlying Upper Chinle Formation is exposed. The other structures associated with Laramide Orogeny are smaller thrust faults and fault-propagation folds with the centimeter-scale offset that are abundant in Red Wash Canyon and Arroyo del Cobre. North to northwest orientations of thrust faults and folds are consistent with Laramide structures observed by Magnani et al. (2005) and Erslev and Koenig (2009) in north-central New Mexico.

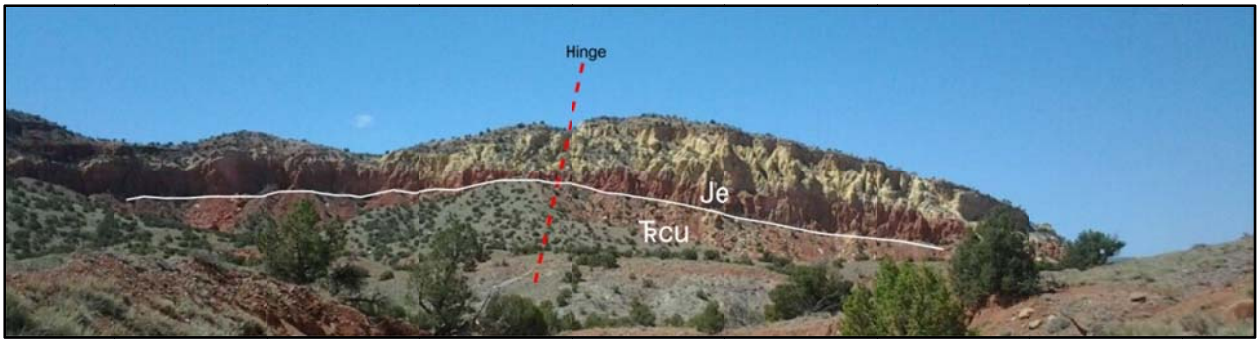

Figure 2.4: Outcrop of the Laramide-age monocline dipping west. The hinge is shown with a dashed red line. View is to the south. Cliff face is approximately 30 m. Je - Jurassic Entrada sandstone, Trcu - Triassic Upper Chinle Formation.

Table 1.1: Description of the structures marked with blue dots in Figure 1.2.

Name	**Location (UTM)**	**Attitude**	**Motion**
Fault-propagation fold 1	376560, 4011770	N10E/55NW	Reverse
Fault-propagation fold 2	379579, 4013622	N56W/34NE	Reverse
Thrust fault	379190, 4012679	N45W/61SW	Reverse
SF1	382665, 4010818	N60E/74SE	Normal
SF2	382713, 4010941	N10W/72NE	Normal
SF3	382849, 4010844	N55E/59NW	Normal
SF4	382921, 4010805	N69E/74SE	Normal
SF5	383088, 4010769	N5W/76SW	Normal

2.2 Stratigraphy

The rocks in the study area range from Miocene to Permian in age (Figure 2.5). The youngest formation present in the area is Late Oligocene-Miocene Abiquiu Formation. The Abiquiu Formation consists of white tuffaceous sandstone with some volcaniclastics present. Oligocene Ritito Conglomerate underlies Abiquiu. Alluvial fan deposits of Ritito Formation contain the angular clasts of metamorphic rock originated from Tusas Mountains and transported by southward-flowing streams (Maldonado and Kelley, 2009). The base of Ritito unconformably overlies Eocene El Rito Formation which ranges from boulder-sized well-rounded conglomerates at the base to fine-grained sandstones interbedded with siltstone. Both El Rito and Ritito are interpreted to be deposited during the erosion of Tusas Mountains due to Laramide uplift

(Maldonado, 2008; Maldonado and Kelley, 2009). The base of El Rito unconformably overlies the Jurassic Morrison Formation where approximately 185 m of Cretaceous rocks consisting of Mancos Shale, Dakota Sandstone, and Burro Canyon Sandstone were eroded (Kelley et al., 2005). In areas where Morrison is not present, El Rito forms an unconformity with Jurassic Entrada sandstone or Triassic Chinle formation (Maldonado, 2008). The unit related to Morrison Formation observed in the field is the Brushy Basin Member. The unit presents greenish-purple siltstone interbedded with white fine-grained sandstone which was deposited in a fluvial environment (Flesch, 1974). The Morrison overlies Jurassic Todilto limestone of the Wanakah Formation that is presented as massive to basal laminated lacustrine limestone containing kerogen. The Todilto was deposited in a large saline lake overlying the dune field (Vincelette and Chittum, 1981).The base of Todilto is in contact with Jurassic Entrada sandstone which is a cliff-forming massive aeolian sandstone. The Todilto is rich in organic matter and serves as a source rock for the Entrada sandstone in San Juan basin located on the Colorado - New Mexico border (Vincelette and Chittum, 1981). The Entrada sandstone is composed of well-sorted porous quartz sandstone. Entrada gradationally changes colors from red at the base, to white in the middle, and yellow at the top. (Kelley et al., 2005; Maldonado, 2008) . The maximum burial depth of Entrada is approximated to be 1 km in the study area (Figure 2.5). Triassic Chinle Formation underlies Entrada. In Red Wash Canyon, Upper and Middle members of Chinle Formation are observed. Petrified Forest Member presents the Upper Chinle and is composed of brown-red siltstone and shale containing wood fragments. Poleo is the Middle Member which is a massive quartzose sandstone (Kelley et al., 2005). Arroyo del Aqua Formation of Permian Cutler Group is the oldest unit that outcrops in the study area (Maldonado, 2008). The formation is presented by dark purple siltstone and shale interbedded with sandstone.

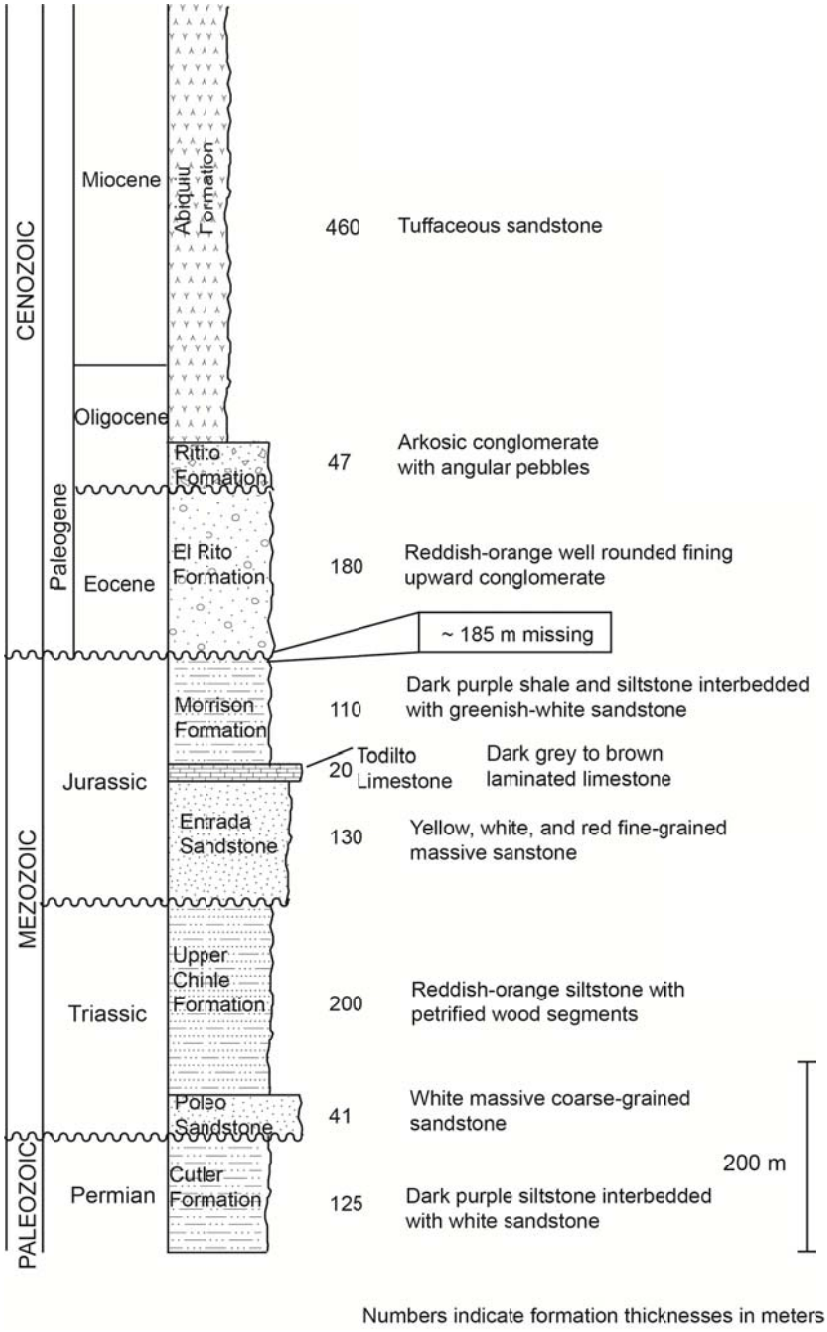

Figure 2.5: Stratigraphic column of the rocks present in Abiquiu Embayment. Unit thicknesses are taken from Baldridge et al., 1994; Maldonado, 2008; Maldonado and Kelley, 2009; Kelley et al., 2005.

2.3 Geologic Cross-Sections

A cross-section in the vicinity of the study area passing through the Cañones fault and the monocline is shown in Figure 2.6. An unconformity where Oligocene (Tr) rocks are deposited on top of Jurassic (Jm) is captured in the section. Two other unconformities, Permian-Triassic (between Pcu and Trcp) and Triassic-Jurassic (between Trcu and Je-r) are also present.

The throw of the fault in this area is 450 m in the southern part of the map (Figure 2.6 (a)); it is reduced to 240 m towards the north (Figure 2.6 (b)). A similar deformation trend is observed in the monocline where its curvature is much smaller in the northern part compared to the southern (O'Keeffe, 2014). The strikes of both structures (N40E for the fault and N10E for the monocline) mentioned in Section 2.1 are subparallel. East-west Rio Grande extension in this area is coincident with earlier Laramide compaction direction.

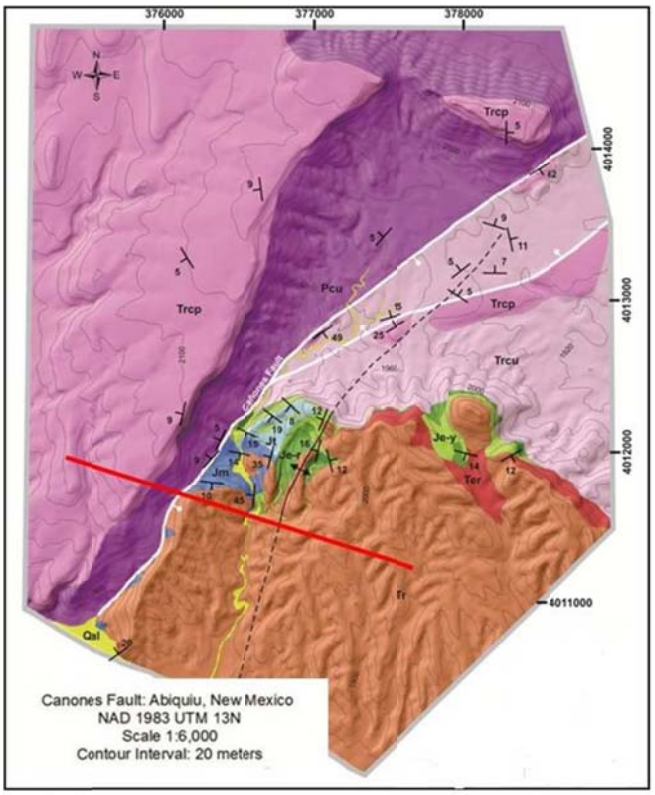

Legend

- Anticline
- (White Line) Canones Fault
- Strike & Dip
- Qal — Quaternary Deposits
- Tr — Tertiary Ritito
- Ter — Tertiary El Rito
- Jm — Jurassic Morrison
- Jt — Jurassic Todilto Ls.
- Je-y — Jurassic Entrada Ss. (Yellow-Pink)
- Je-r — Jurassic Entrada Ss. (Red)
- Trcu — Triassic Chinle (Upper)
- Trcp — Triassic Chinle (Poleo)
- Trcl — Triassic Chinle (Lower)
- Pcu — Permian Cutler (Upper)

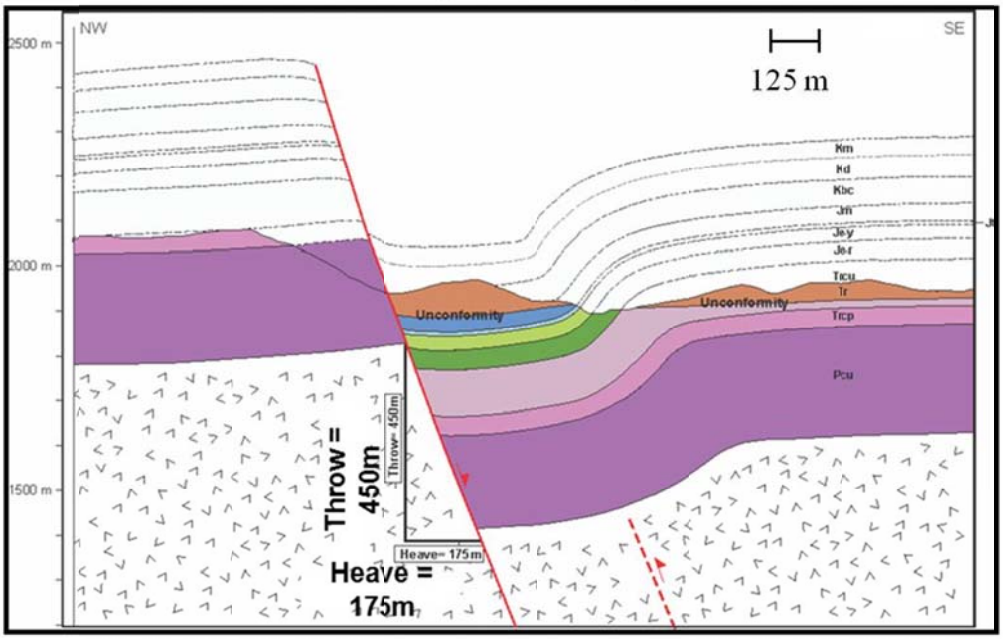

a)

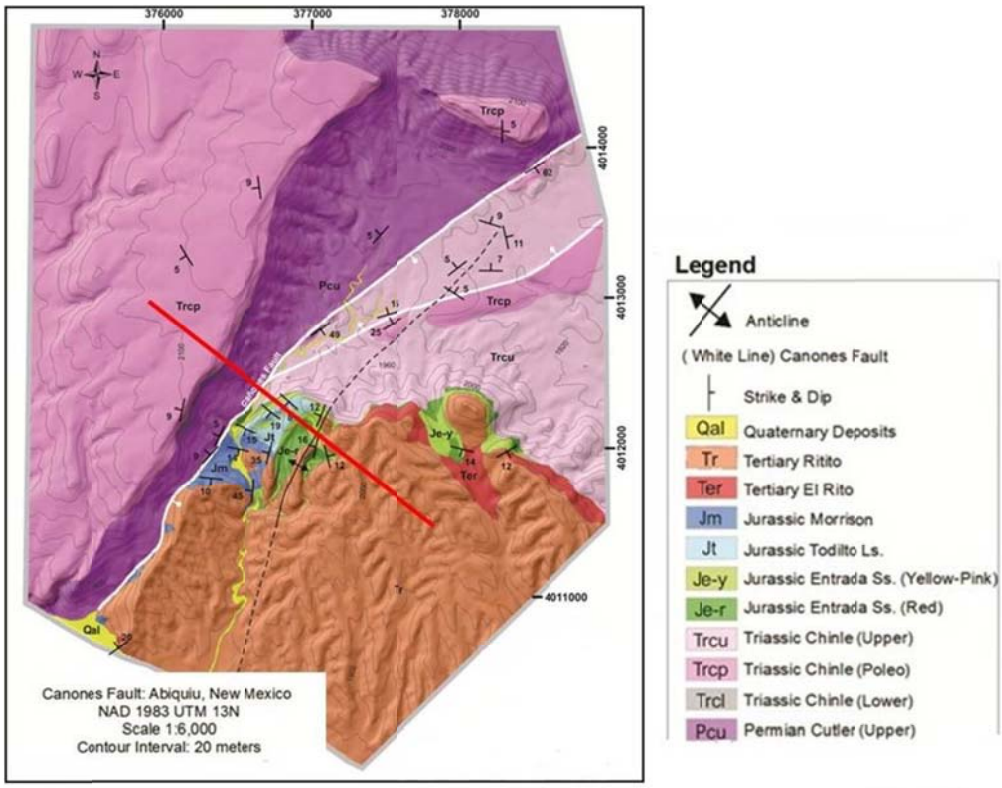

b)

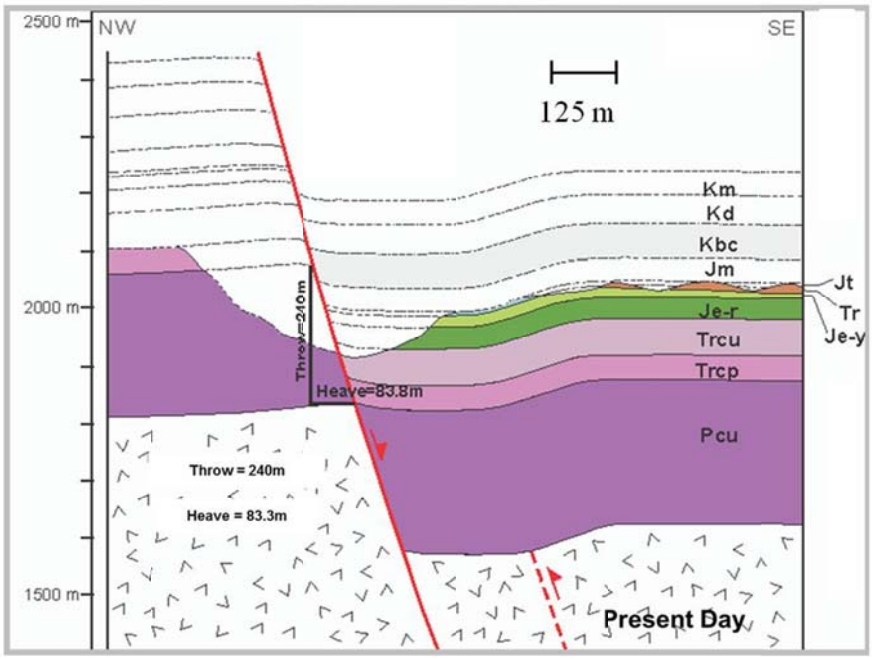

Figure 2.6: Geologic cross-section in Red Wash Canyon showing Cañones fault and the monocline a) in the southern part of the study area and b) in the northern part of the study area. The location of each cross-section is indicated with solid red line on the maps to the right. The present day rocks are colored in, and the eroded section is hollow. The missing units include Burro Canyon sandstone (Kbc), Dakota sandstone (Kd), and Mancos shale (Km). Bending of the monocline and the fault throw on Cañones fault increase from north to south (modified from o'Keeffe, 2014).

3. FORMATION OF DEFORMATION BANDS

Deformation bands are the structures typically associated with faulting in porous sandstones. They are zones of strain localization along which a fault may develop. Different types of deformation bands may be found in the damage zone depending on depth of burial, mineral composition, and fluids present in the formation. The type of deformation band encountered in the damage zone has an effect on porosity and permeability of the rock. Also, it has an influence on elastic properties as changes in rock properties occur during deformation.

3.1 Types of Deformation Bands

Deformation bands present gouge-filled fractures where material within the fracture has different physical properties from the undeformed, or host, rock. Deformation bands are differentiated based on the rock kinematics where shear, compaction and dilation bands are the end members (Figure 3.1). Combination of shearing with compaction or dilation produces compactional shear or dilational shear bands, respectively (Fossen et al., 2007).

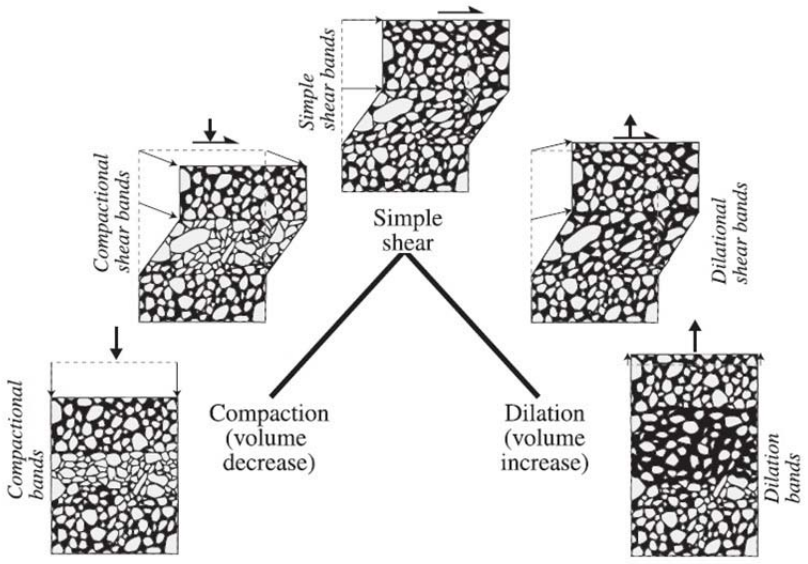

Figure 3.1: Types of deformation bands based on kinematic processes occurring during deformation (Fossen et al., 2007).

Another classification of deformation bands is based on rock texture, chemical composition of fluid, and overburden stress. Four types of bands are distinguished from the above characteristics. The first type is disaggregation band where grains are reorganized by grain rolling (Figure 3.2 (a)) (Du Bernard et al., 2002a). Disaggregation bands form in shallow conditions where depth of burial is less than 1 km (Fossen and Bale, 2007). Three subgroups (compactional, dilational, and shear) of disaggregation bands can be observed depending on their orientation relative to the maximum principal stress (σ_1) (Figure 3.3). Dilational bands develop parallel to σ_1, compactional bands are perpendicular to σ_1, and shear bands form at an acute (~30°) angle to σ_1. Grain rolling and reorganization in compactional and shear subgroups of disaggregation bands leads to porosity reduction and causes decrease in permeability perpendicular to the band. Dilational bands, in contrast, result in pore space increase and become conduits for fluid flow (Du Bernard et al., 2002a).

The second type, a phyllosilicate band, forms by the same mechanism of grain rolling as a disaggregation band, but contains more than 10% clay minerals which get preferentially aligned along the band (Figure 3.2 (b)) (Torabi, 2007). Such bands are visible in outcrop due to the contrast in mineral composition from the host rock. In lithologies with more than 40% clays present, the bands form clay smears where the deformation band is composed entirely of clay minerals. Clays enhance grain sliding within the band and cause phyllosilicate bands to have greater offsets compared to the other types of deformation bands. Significant decrease in porosity and permeability is observed within a band due to pore space collapse and infiltration with phyllosilicates (Fossen et al., 2007).

Cataclastic bands present the third type and are characterized by grain fracturing and crushing during rotation (Figure 3.2 (c)). The band is characterized by a low-porosity and low-

permeability gouge that stands out as a more resistant feature compared to the host rock in the outcrop. During cataclasis, the rock initially undergoes compaction and fracturing without major reduction in grain size. As cataclasis progresses, the grains rotate and crush forming a zone of finer grained poorly sorted sand surrounded by fractured grains (Engelder, 1974).

Dissolution bands comprise the last type of deformation bands which are formed during dissolution of the existing minerals along the deformed rock and their later precipitation (Figure 3.2 (d)). Stress magnitude, temperature and grain size of the rock affect the rate of mineral solution and precipitation. The process of these bands' formation consists of three steps that involve 1) dissolution along grain contacts, 2) mixing of dissolved minerals with water and 3) and precipitation of solution on grain edges (Renard et al., 2000).

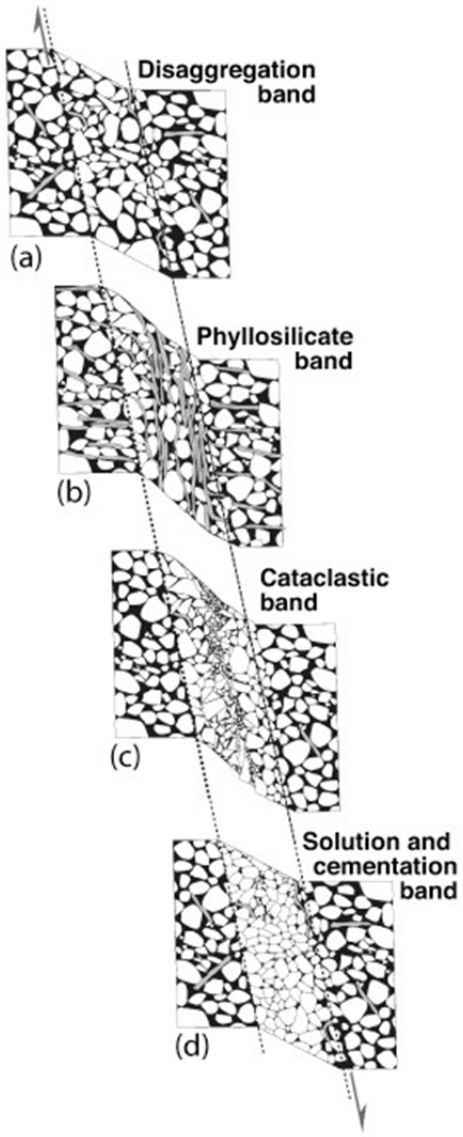

Figure 3.2: a) Disaggregation band composed of mostly quartz grains that is formed by grain rotation and sliding; b) phyllosilicate band that is formed from a host rock consisting of more than 10% of clay minerals; clays enhance grain sliding during deformation; c) cataclastic band that develops from disaggregation bands with an increase of applied pressure; smaller grain size as a result of grain crushing can be observed; d) dissolution band where pore space is filled with dissolved and repricipitated minerals (Fossen et al., 2007).

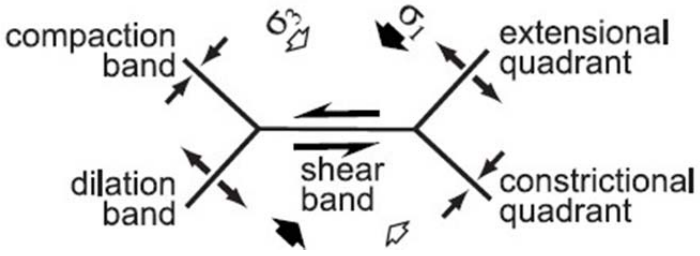

Figure 3.3: Schematic orientations of three subgroups (compressional, dilational, and shear) of disaggregation bands relative to the maximum principal stress (Du Bernard et al, 2002a).

3.2 Mechanism of Deformation Bands' Development

Burial history and tectonic forces facilitate deformation band development and transformation from one type to another (Figure 3.4). Disaggregation bands are the first features to form due to gravitational forces. Compaction promotes pore collapse and clay, if present, intrusion into the remaining pore space forming phyllosilicate bands. As the confining pressure due to burial or tectonism increases, the grains undergo cataclasis, and cataclastic bands develop. When the gravitational unloading occurs, the open fractures develop (Fossen et al., 2007).

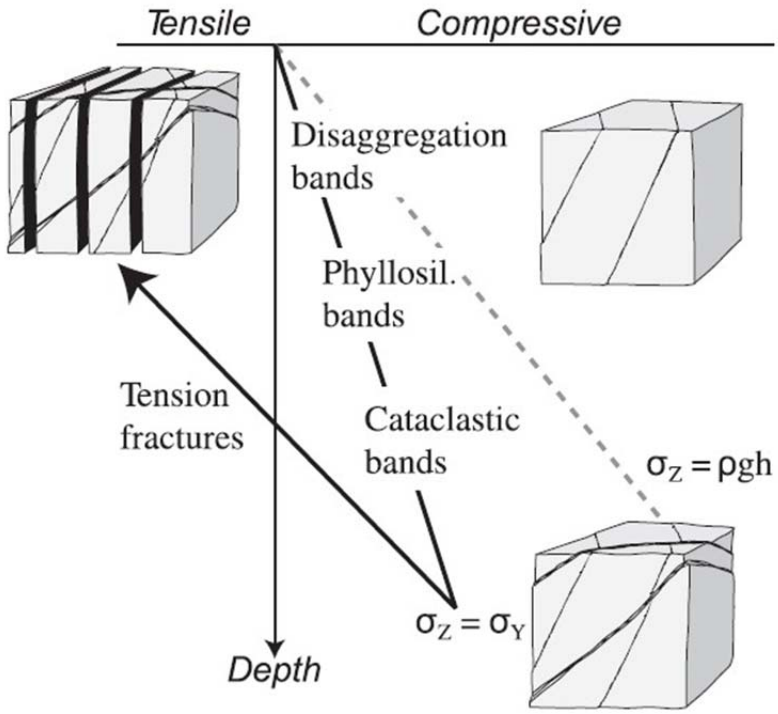

Figure 3.4: Evolution of deformation bands with increasing depths of burial and later exhumation (Fossen et al., 2007).

Deformation bands precede faulting and create a zone along which a fault breaks. The model of cataclastic deformation bands' development is described by Antonellini and Aydin (1995). Initially, a single deformation band of about 1 mm in width with an offset on a millimeter scale develops (Figure 3.5 (a)). In the next stage, more deformation bands form as a result of strain accommodation producing a deformation band zone of several centimeters thick

with decimeter-scale cumulative offset (Figure 3.5 (b)). Finally, the rock breaks along a plane adjacent to the deformation band zone creating a slip plane (Figure 3.5 (c)).

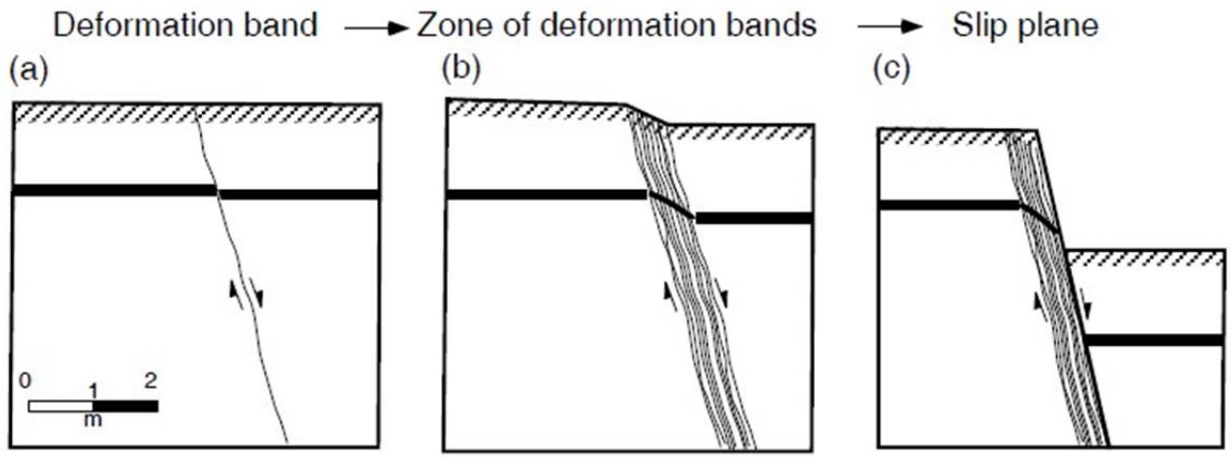

Figure 3.5: Generation of a fault slip as a result of deformation bands development, where a) a single deformation band forms as a result of strain localization, b) multiple deformation bands develop into a zone of deformation bands as deformation progresses, and c) slip plane initiates on the edge of deformation band cluster (Antonellini and Aydin, 1995).

Laboratory experiments to understand the development of deformation bands were conducted by Engelder (1974) and Mair et al (2000) on clean sandstones. Engelder (1974) concentrated on producing a single deformation band at various confining pressures and changing shear displacement. Thin sections of produced deformation bands were then analyzed to relate their properties back to observed shear displacement and confining pressure. Grain cataclasis was observed within the band where fractured large grains were surrounded by smaller crushed grains. While cataclastic deformation was observed within the band, no inference about the differential pressure required to produce such band was made.

Next, Mair et al. (2000) tested the progression from an individual deformation band to a zone of deformation bands in a laboratory conditions. The experiment was conducted on a porous aeolian Lochabriggs sandstone 100 mm in diameter and 230 mm in length at a confining pressure of 34 MPa. During the experiment, formation of cataclastic deformation band zones

within the core samples were observed. The thickness of deformation band zone increased progressively with applied strain. Differential pressure ($\sigma_1 - \sigma_3$) at which rock failed were recorded between 120 and 140 MPa. Considering Antonellini and Aydin (1995) model, first and second stage of the deformation band development were reproduced in the above laboratory experiment. Slip surface generation was not observed during the experiment which the authors attributed to insufficient stress applied to the samples.

3.3 Deformation Bands in Entrada Sandstone

Thin sections of Entrada sandstone (Figures 3.6, 3.7 and 3.8) were made to determine internal structure and mineralogical composition of deformation bands in the study area. Red outline defines the edge of a deformation band in Figures 3.6 and 3.7. Figure 3.6 shows grain size and sorting of deformation bands and host rock. The bands are surrounded by high porosity rock that consists of sub-rounded to sub-angular grains. Porosity within the bands is significantly reduced by the presence of finer irregularly-shaped grains that fill up the space between larger grains.

Higher magnification (Figure 3.7) reveals the mineral composition of the band and the host rock. The higher porosity host rock consists of quartz grains where some of the pore space is filled with calcite cement. The band consists of 100 μm in diameter quartz grains floating in much smaller angular quartz grains. Calcite is not visible in the band. Some of the larger grains within the deformation band and host rock are fractured.

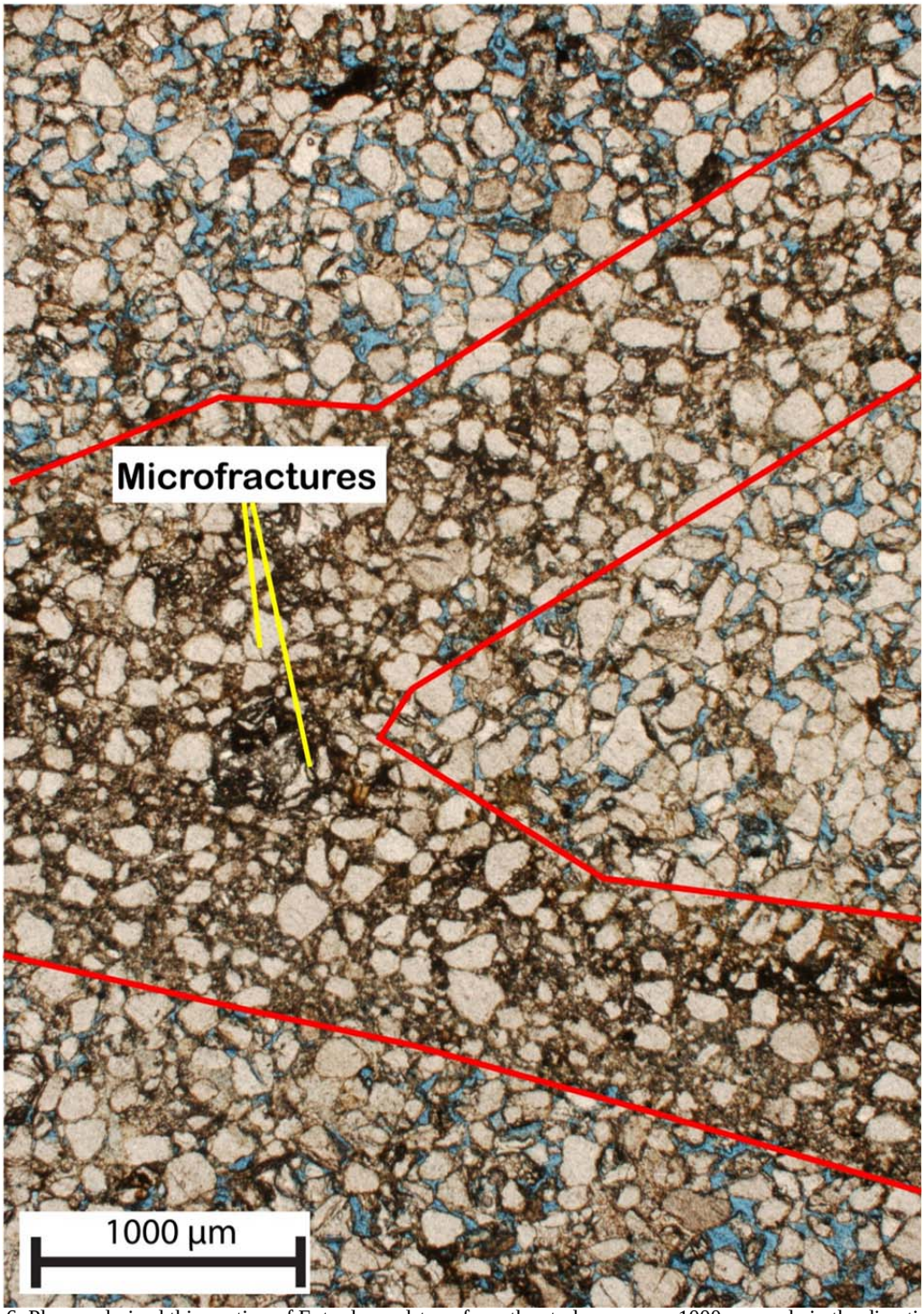

Figure 3.6: Plane-polarized thin section of Entrada sandstone from the study area on a 1000 µm scale in the direction parallel to the bedding. Deformation bands are the zones of low porosity outlined in red. Grains within the band and matrix rock are sub-angular to sub-rounded. Fracture are visible in some large grains. Smaller grains within the band are angular.

a)

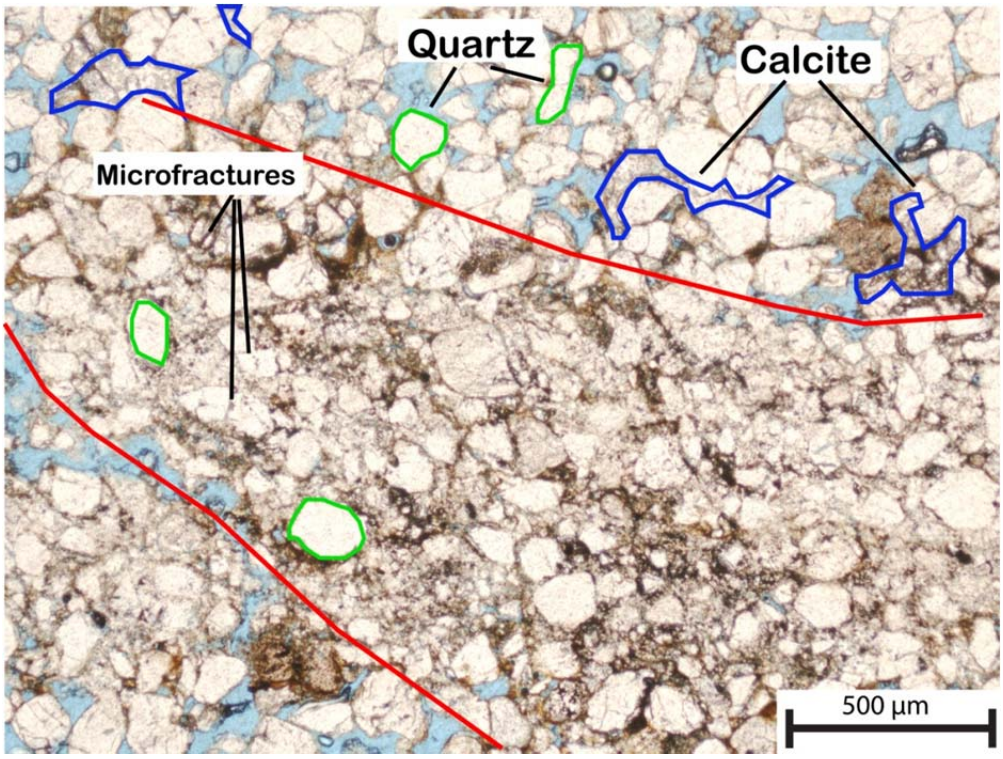

b)

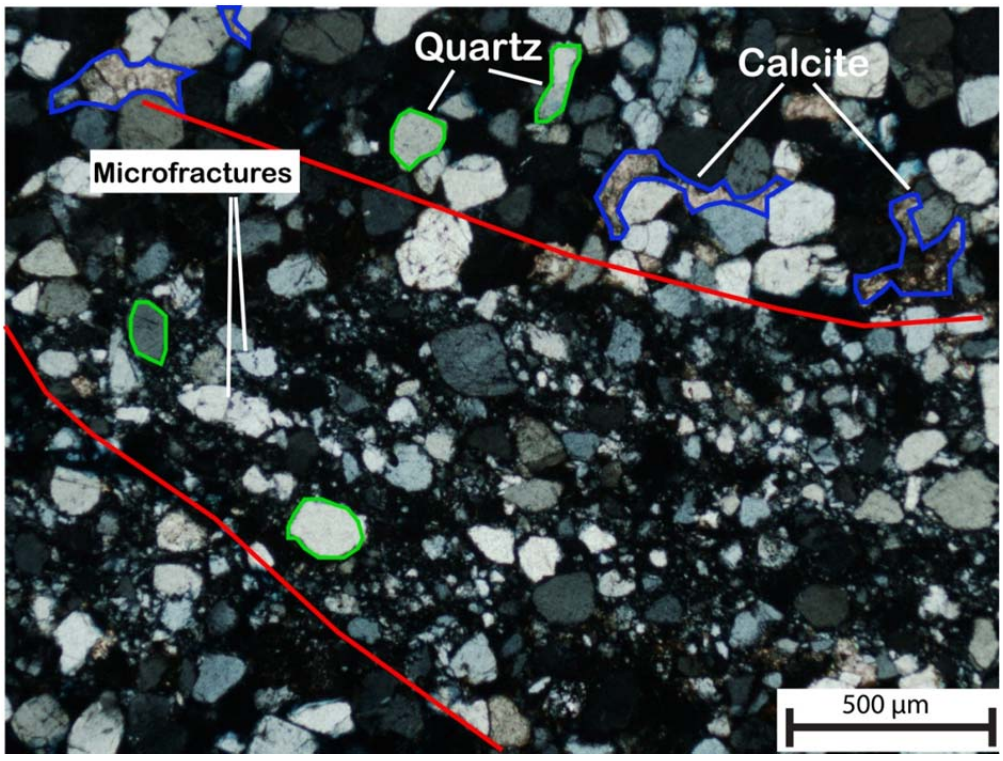

Figure 3.7: Deformation band in the Entrada sandstone on a 500 µm scale in a) plane-polarized light and b) cross-polarized light in the direction parallel to the bedding. Quartz grains are outlined in green, and calcite cement is outlined in blue. Microfractures are observed within some of the quartz grains. Finer grains are more angular than larger grains.

Figure 3.8 shows magnified quartz grains within a deformation band on a 100 μm scale. As noted previously, microfractures and high angularity of smaller grains are observed in the band. Also, some of the grains exhibit conchoidal fractures which are characteristic of quartz deformation (Klein and Dutrow, 2007).

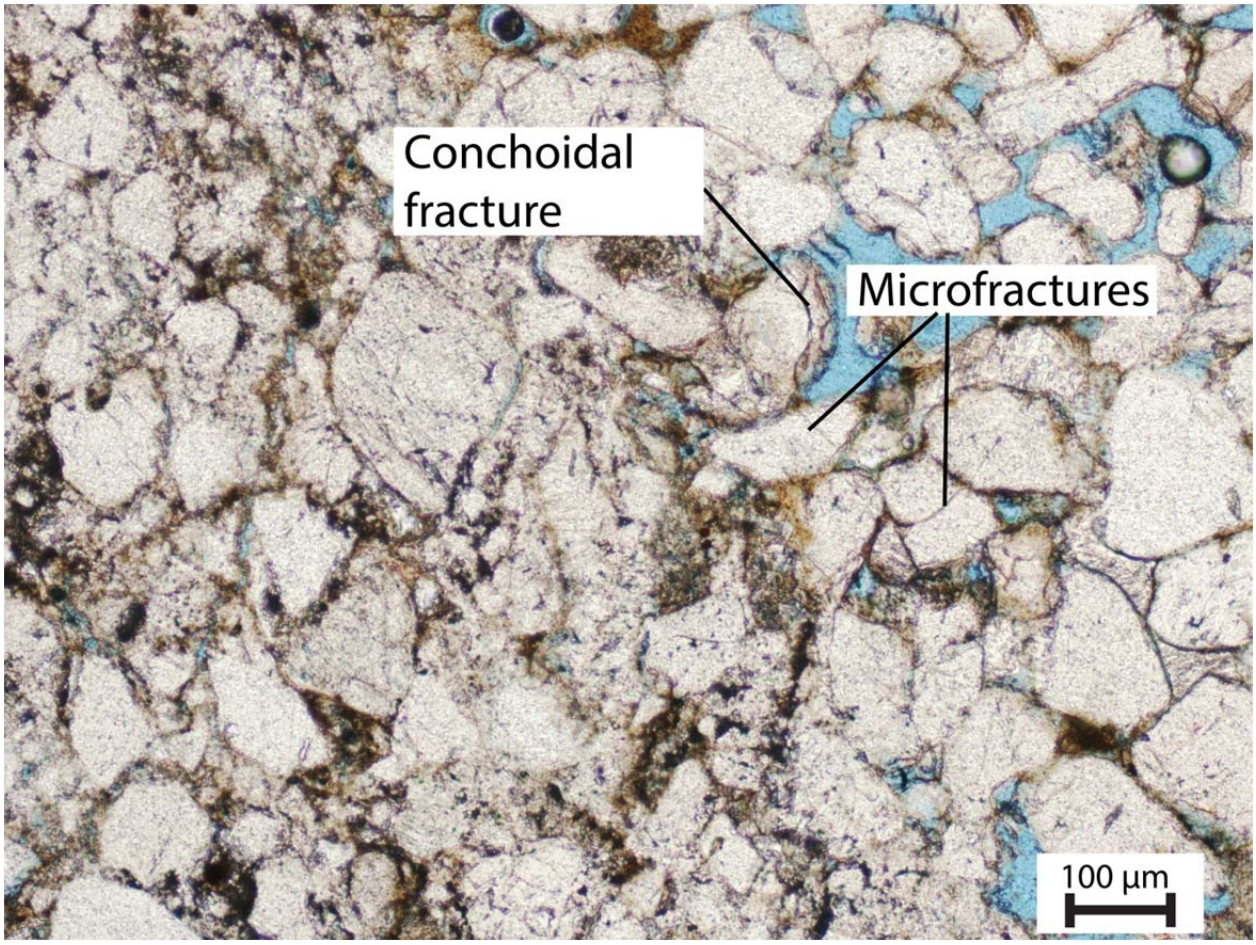

Figure 3.8: Magnified image of a deformation band in Entrada sandstone on a 100 μm scale. The thin section orientation is parallel to bedding. Some of the quartz grains exhibit microfractures. Conchoidal fractures at the edges of some grains are also observed.

3.4 Depth of Burial and Inferred Stress Magnitudes in Entrada Sandstone

Depth of burial of Entrada sandstone in the study area along with the graphs derived by Zoback (2010) from Mohr-Coloumb failure criterion were used to infer stress magnitudes at which these deformation bands formed (Figure 3.9). Magnitudes of principal stresses and

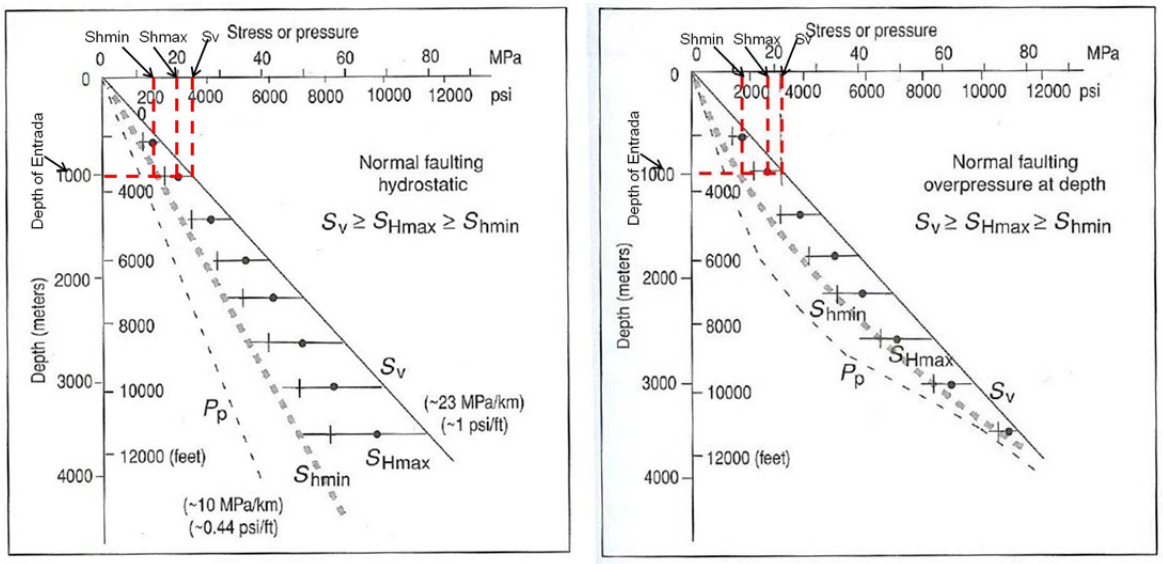

a)

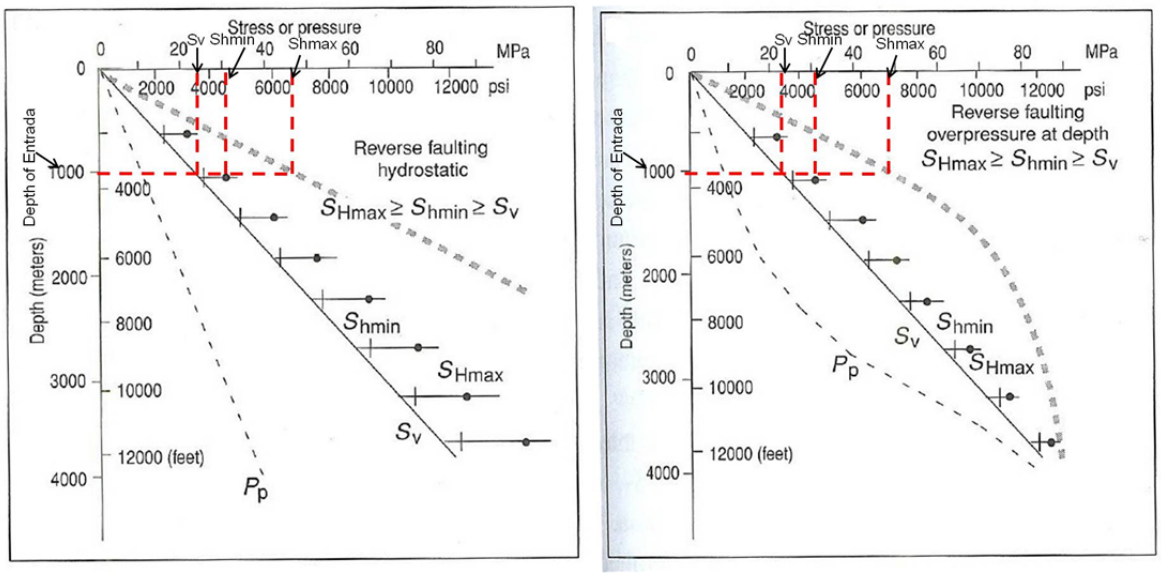

b)

Figure 3.9: Graphs showing the magnitudes of principal stresses based on the depth of burial in a) normal faulting regime at hydrostatic pore pressure (left) and overpressure (right) and b) reverse faulting regime at hydrostatic pore pressure (left) and overpressure (right). The red dashed lines indicate stress magnitudes for Entrada sandstone (modified from Zoback, 2010).

differential pressure for both extensional (normal faulting related to Rio Grande rifting) and compressional (reverse faulting related to Laramide Orogeny) regimes were estimated. In the study area, the maximum depth of burial of Entrada sandstone is around 1 km (Figure 2.5, page 12). Since pore pressure at the time of folding and faulting is unknown, both cases for normal hydrostatic pressure and overpressure were taken into account for the estimation. In extensional regime, σ_1 is 23 MPa and σ_3 is 13 MPa at hydrostatic pore pressure which gives the differential pressure of 10 MPa. In case of overpressure, σ_1 is 21 MPa and σ_3 is 12 MPa that produces 9 MPa differential pressure (Figure 3.9 (a)). In compressional regime at hydrostatic pressure, σ_1 is 47 MPa σ_3 is 23 MPa which produces differential pressure of 24 MPa. Overpressured formation in compressional regime gives σ_1 and σ_3 magnitudes of 50 MPA and 23 MPa, respectively; differential pressure in this case is equal to 27 MPa (Figure 3.9 (b)).

3.5 Outcrop of Deformation Bands in Entrada Sandstone

Outcrop pattern of deformation band in the study area is shown in Figure 3.10. Single deformation bands, some of which join into deformation band clusters are observed which resemble the first and second stages of deformation band development described by Antonellinin and Aydin (1995). The examples of the final stage where the slip surface develops is the Cañones fault itself and smaller faults observed in the area.

Figure 3.10: Single deformation bands and deformation band clusters in Entrada sandstone, Red Wash Canyon, New Mexico. These features are lighter in color and more resistant compared to the surrounding rock.

4. DISTRIBUTION OF DEFORMATION BANDS IN THE FAULT DAMAGE ZONE

4.1 Literature Overview of Deformation Bands' Distribution Models

The structural elements of a fault include fault core and a fault damage zone (Figure 4.1). The fault core is a zone of the largest offset along deformed rock that incorporates fault surfaces, parts of the host rock, gouge material, etc. The damage zone is the area adjacent to the fault core that is less deformed than the fault core and contains deformation bands, fractures, smaller faults and other structures (Berg and Skar, 2005; Torabi et al., 2013).

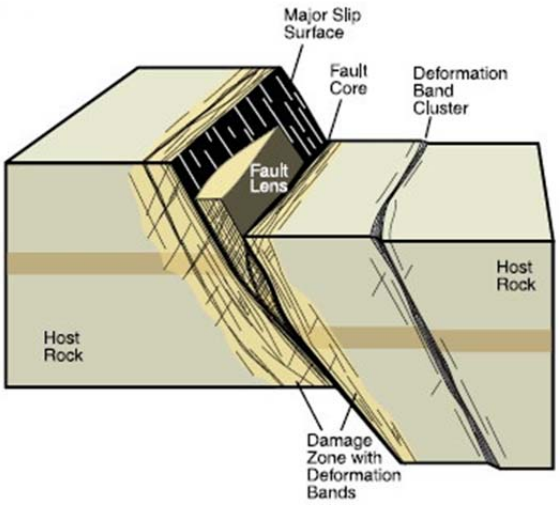

Figure 4.1: Schematic representation of fault damage zone elements. The maximum deformation is seen adjacent to the fault core. Deformation bands in the damage zone are clustered (Torabi et al., 2013).

Deformation band density in the fault damage zone is affected by rock strength, mineralogy, texture, cementation, and tectonic history of the region (Nelson, 2001; Fossen et al., 2007). Many authors have described deformation band density in outcrops across the damage zones of the faults (e. g. Berg and Skar, 2005; Du Bernard et al., 2002b; Shipton and Cowie, 2003; Kolyukhin et al., 2010; Saillet and Wibberley, 2010). Several models of deformation bands' distribution based on the outcrop data exist in the literature. One example is the study conducted by Kolyukhin et al. (2010) on multiple faults in Utah and Sinai where the gradual

decrease in deformation band density with increasing distance from the fault core was observed for the majority of the faults. A few outliers in the form of localized slip surfaces surrounded by high deformation-band concentration were seen within the damage zone in some of the faults. However, the decrease in deformation band density could be modeled by using an exponential fit (Figure 4.2).

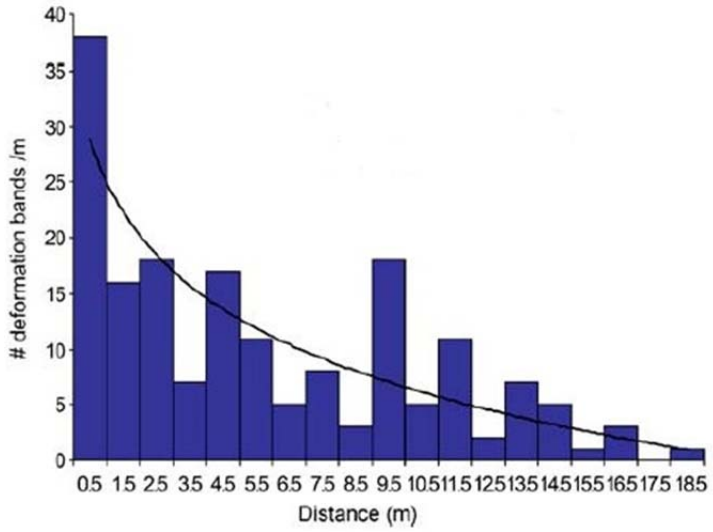

Figure 4.2: The deformation band density from the fault core to the end of the damage zone can be fitted with negative exponential curve; data from the CIPR database for the faults from Utah and Sinai (Kolyukhin et al., 2010).

Another model suggests that the damage zone is clustered into deformation band zones and slip surfaces with high deformation band density. The deformation band density drops between the clusters (Figure 4.3). The end of the damage zone is defined where deformation band density drops to some background levels, and no clusters are observed (Du Bernard et al., 2002b; Shipton and Cowie, 2003). Some variations of this model show that the density of the deformation bands stays constant in between the clusters. When mapping fault-related deformation in Navajo sandstone in Utah, Shipton and Cowie (2003) have observed the peaks of deformation band density adjacent to slip planes. The areas in between the slip planes had a constant low deformation band density. The other studies show gradual decay in deformation

band density away from the clusters as observed by Saillet and Wibberley (2010) in Bassin du Sud-Est, France. They define such decay in deformation band density as a “ladder pattern.”

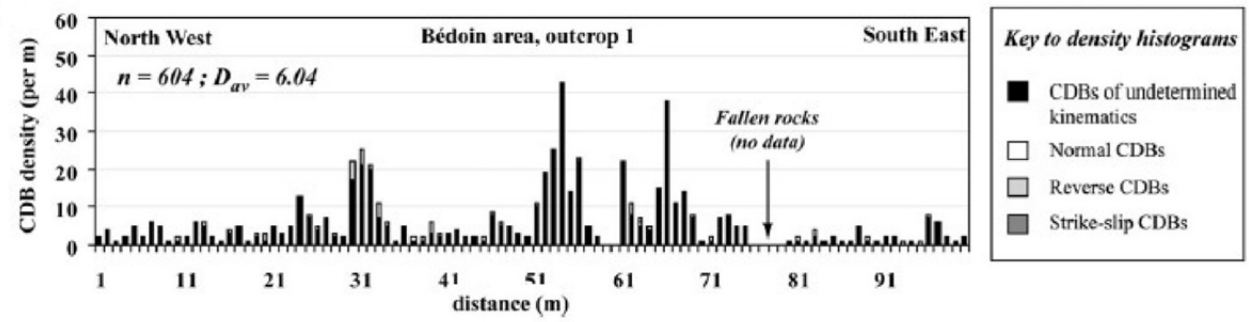

Figure 4.3: Clustering of deformation bands observed in Bédoin region, Bassin du Sud-Est (Saillet and Wibberley, 2010).

Based on reviewed literature, variation in deformation band distribution is seen in fault outcrops for different study areas, and the models of deformation bands' distribution have to be fitted individually for a specific example. However, several common trends can be recognized. First, the increase of deformation band density is observed in direct proximity to the main fault slip and around minor slip planes and deformation band clusters within the fault damage zone. As shown in examples from Du Bernard et al. (2002), Shipton and Cowie (2003), and Figure 4.3, clustering of deformation bands into zones of high deformation band density is evident. Also, the fault data analyzed by Kolyukhin et al. (2010) (Figure 4.2), despite being fitted exponentially, shows occasional peaks in deformation band density away from the fault.

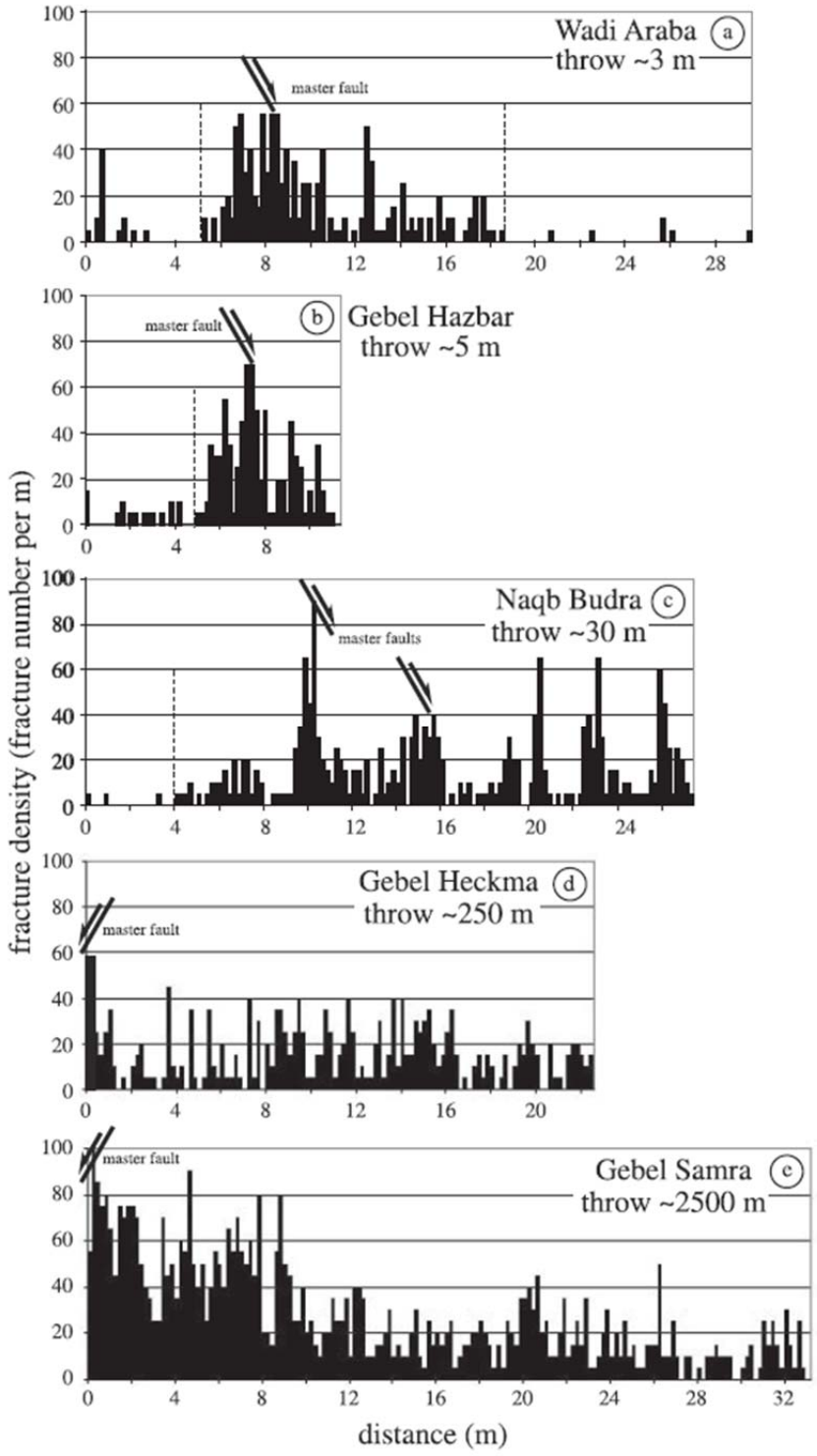

Figure 4.4: Comparison of the damage zone widths in normal faults with different throws, Suez Rift. Dashed vertical lines represent damage zone cutoffs. The faults with larger throw have a wider damage zone. Hanging wall damage zone is wider than the footwall damage zone (Du Bernard et al., 2002b).

Second, the damage zone width is proportional to the fault throw (Du Bernard et al., 2002b; Shipton and Cowie, 2003). The study conducted by Du Bernard et al. (2002b) in Suez Rift compared the damage zones of normal faults with throws varying between 3 and 2500 m and observed the increase in damage zone width in faults with larger throw (Figure 4.4). This relationship can also be observed on a smaller scale in thin sections (Engelder, 1974) and cores (Mair et al., 2000) where the thickness of individual deformation bands and zones of deformation bands increases due to larger volumes of rock incorporated into damage zone as displacement progresses.

Third, the deformation band density increases with the curvature of the strata (Antonellini and Aydin, 1995; Berg and Skar, 2005). Figure 4.5 shows a diagram of Bartlett fault in Utah from the field study by conducted Berg and Skar (2005). As seen in the diagram, the downward movement of the hanging wall relative to the footwall of the fault results in bending of the hanging wall strata while the footwall rock remains flat. Lateral extent of deformation in the hanging wall of the fault is three times greater than the footwall. Generation of the wider hanging wall damage zone was also observed by Du Bernard et al. (2002b) in faults of Suez rift (Figure 4.4) which, as Bartlett fault, exhibit normal sense of motion.

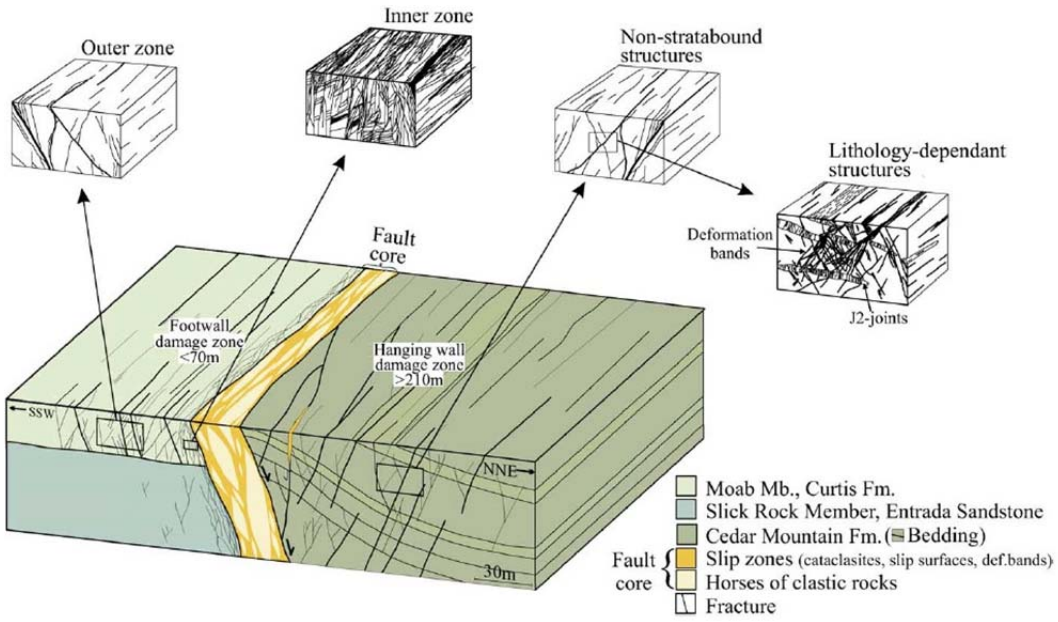

Figure 4.5: Field observations of deformation in hanging wall and footwall of Bartlett fault, Utah. The hanging wall damage zone is three times wider than the footwall damage zone. The bending of the rock units in the hanging wall is clearly observed while the footwall rock remains flat (Berg and Skar, 2005).

4.2 Field Observations of Deformation Bands' Distribution in the Study Area

An approach of determining deformation band density described in literature (e. g. Antonellini and Aydin, 1995; Du Bernard et al., 2002b; Shipton and Cowie, 2003) is to pick a continuous traverse, where possible, perpendicular to the strike of the structure. Next, the traverse is subdivided into equal intervals, and the number of deformation bands within each interval is recorded. In order to be consistent with previously published data and be able to compare the results, the similar approach of taking a traverse perpendicular to Cañones fault strike and dividing it into 1 m intervals was adopted. This method turned out to be challenging due to the lack of continuous outcrop that ran perpendicular to the fault strike. Figure 4.6 shows the geologic map of the study area where the outcrop of the yellow member of Entrada sandstone for which the data were collected is shown in dark green color and marked as Je-y.

Since the outcrop was not continuous, smaller traverses up to 10 m long were used in this study. Traverse locations are shown with black dots in Figure 4.6.

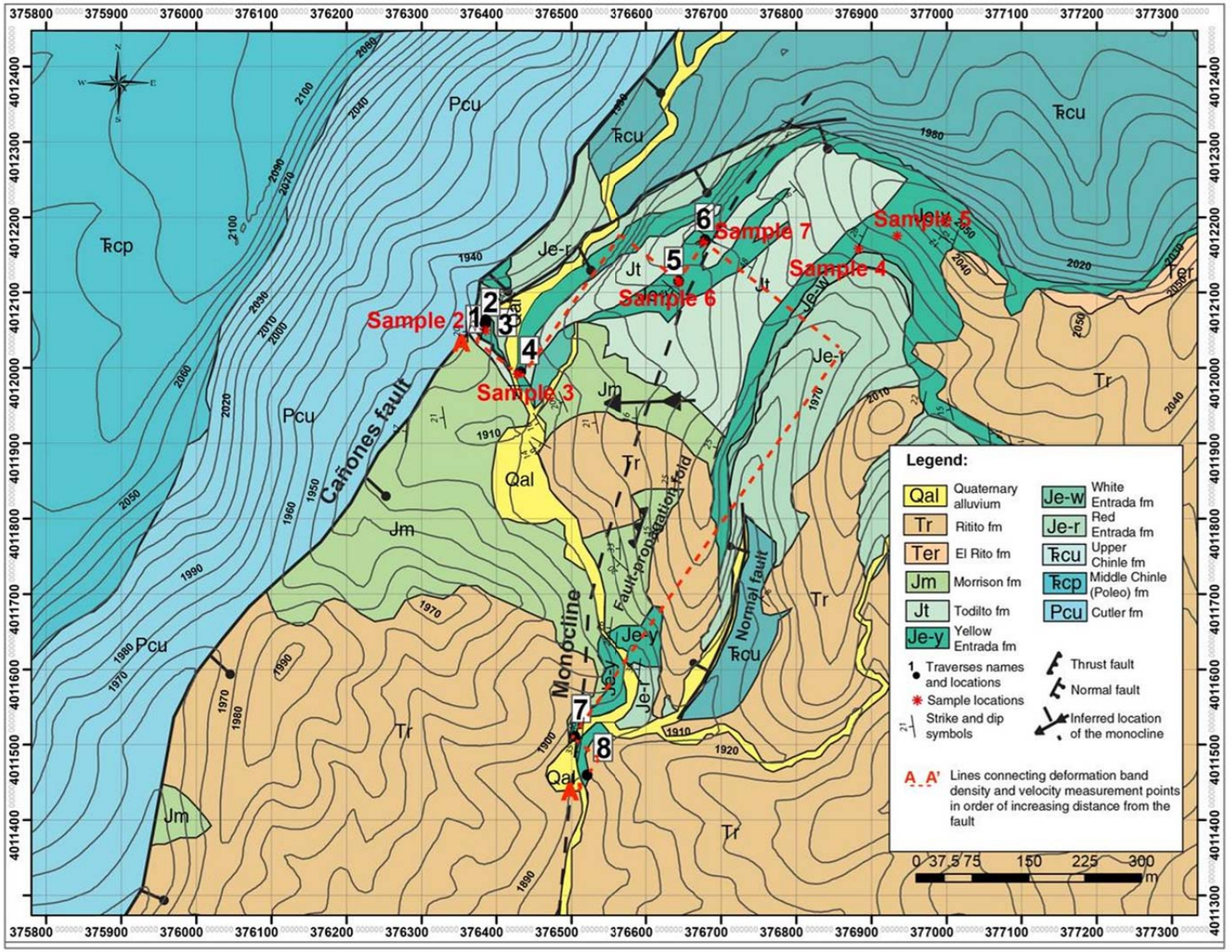

Figure 4.6: Geologic map of the study area in Red Wash Canyon. The rock shown in dark green and marked with the letters Je-y is the yellow member of Jurassic Entrada sandstone for which the data were acquired. Red dashed lines connect the traverses.

Figure 4.7: Example of a traverse layout (traverse 4) for deformation band density measurement. Traverse orientation is S45E which is indicated by a black arrow. Deformation bands' measurement points are separated with solid black lines. The distance between each line is 1 m. Deformation band density is counted within each area between the black lines.

Each traverse was aligned subperpendicular to the Cañones fault strike. Figure 4.7 presents traverse 4 as a layout example. The black lines indicate separations between each measurement point where deformation bands were counted. The GPS location of starting point for each traverse was recorded. Then, the distance between the fault and traverse starting point was calculated using Pythagorean theorem as shown in Figure 4.8. Further, all of the traverse points were sorted relative to the distance to the Cañones fault. Table 4.1 summarizes the locations of traverses and the distances from the fault. The red dashed line from A to A' in Figure 4.6 connects the traverses.

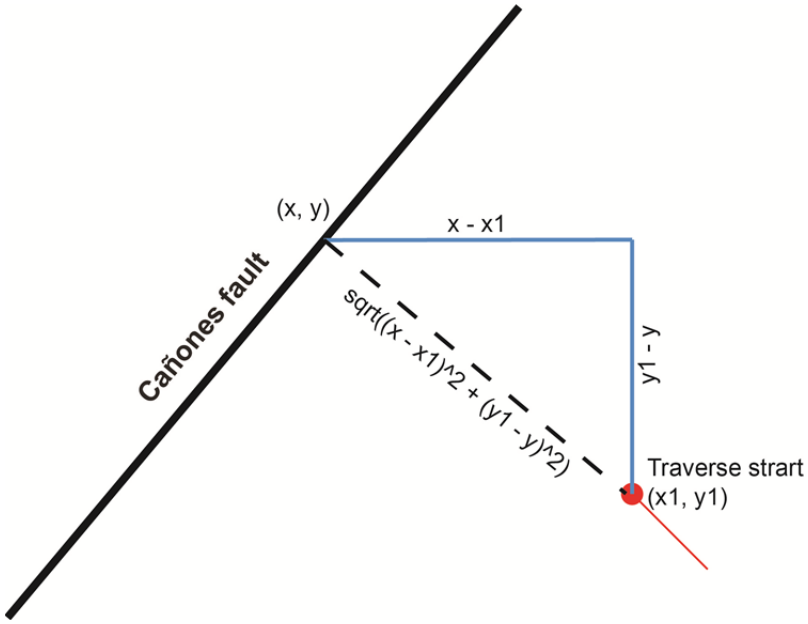

Figure 4.8: A diagram showing the method of computing traverse distances relative to Cañones fault. The starting point of traverse is indicated with red dot.

Table 4.1: Locations of traverses in order of decreasing distance from the fault.

UTM Location (x1, y1)	**Traverse #**	**Bearing**	**Traverse length (m)**	**Distance from the fault (m)**
376383, 4012061	1	S45E	3	16
End of traverse 1	2	S45E	3	19
End of traverse 2	3	S40E	3	22
376430, 4011992	4	S45E	4	91
376641, 4012112	5	S45E	8	195
376676, 4012167	6	S45E	7	205
376502, 4011508	7	S45E	4	438
376518, 4011457	8	S50E	5	473

A plot of deformation band density versus distance from the fault is shown in Figure 4.9. The number of deformation bands per meter within the first 24 m from the fault is high reaching up to 84 bands/m at the points closer to the fault and dropping down to 26 bands/m at the 24th meter. The second interval is located 91 m away from the fault and shows significantly lower deformation band density of less than 20 bands/m. The next cluster of measurements is located in the northern part of the map on the western side of the monocline. A slight increase in

deformation band density up to 30 bands/m 195 m away from the fault is attributed to the influence of monocline. The last two intervals are located in the southern portion of the map to the east of the monocline hinge. The points located closer to the monocline (~438 m away from the fault) show significant increase in deformation band density up to 79 bands/m after which a sharp decrease in deformation density is observed. The influence of the monocline on deformation band density is strong to the south and is not so prominent to the north of the study area. Such change is associated with decrease in bending of the monocline in the northern part of the area (see Chapter 2).

The peaks in deformation band density correlate with the major structures, fault and monocline. Also, the higher curvature of the monocline in the south has lead to an increase of deformation band density relative to its northern part where the curvature is not so steep.

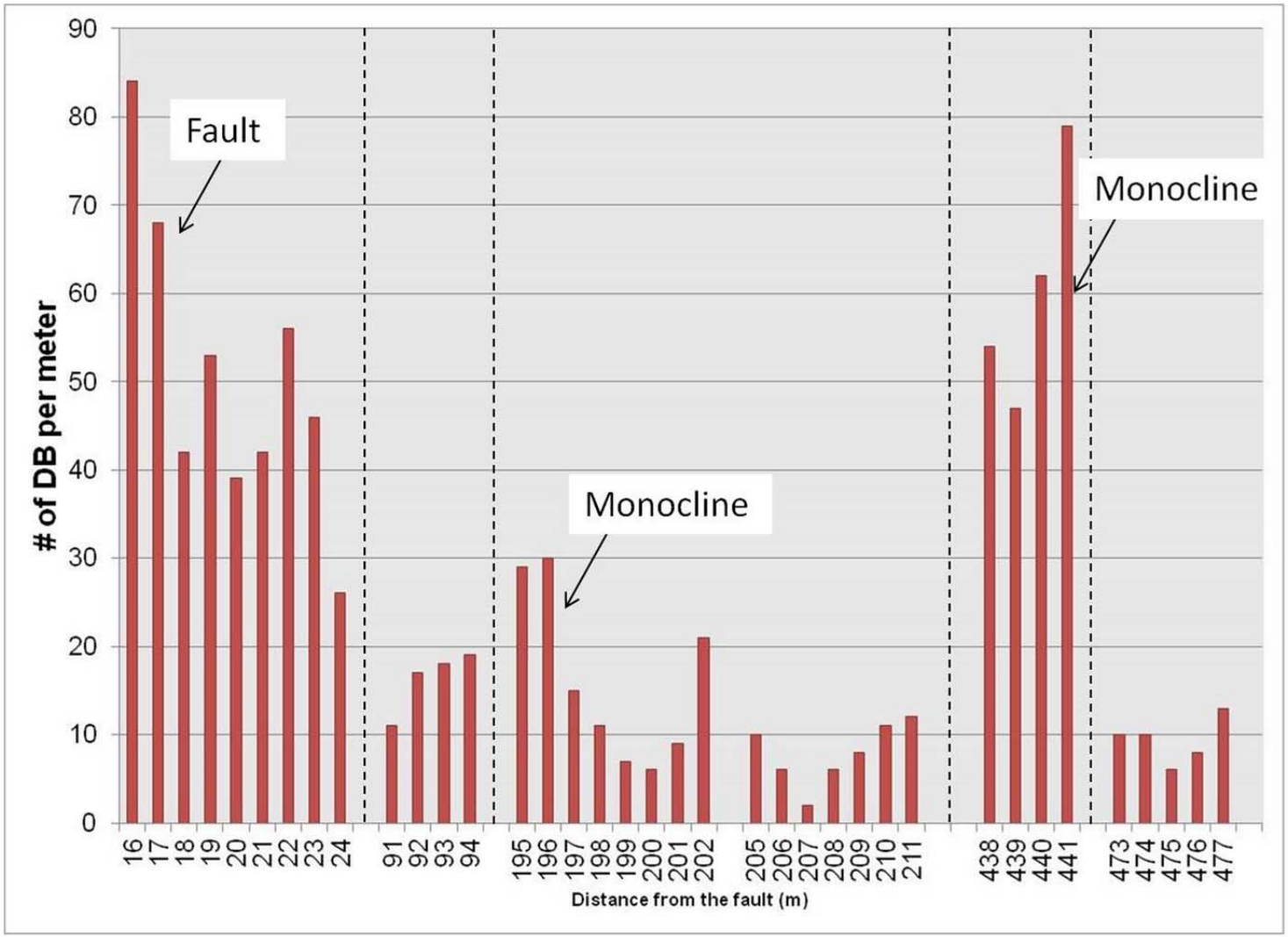

Figure 4.9: Deformation band density versus the distance from Cañones fault. Observed peaks correlate to the structures (fault and monocline). The locations of traverses where the data were collected are found in Figure 4.6.

5. FIELD VELOCITY ACQUISITION AND RESULTS

5.1 Spatial Analysis of Deformation Bands

In this study, I expect to observe the velocity anisotropy associated with the dominant strike of deformation bands, where the fast velocity is oriented parallel to the strike of deformation bands, and the slow velocity is orthogonal to the fast velocity (Chapter 1). In order to align velocity measurements to capture anisotropy, their orientations in the study area were analyzed.

Deformation band orientations were acquired for the yellow member of Entrada sandstone (Figure 4.6 in Chapter 4) along the traverses and plotted using Stereonet software (Allmendinger et al., 2012). Orientations of deformation bands' separated by traverses are shown in Figure 5.1 (a). Traverses 1 and 2 located near Cañones fault, the attitude of which is N40E/70SE, show strikes of deformation bands subparallel to the fault strike around N-S to N40E.

Traverses 5 and 6 in the northern part of the study area to the west of the monocline axis show variation in deformation band orientations with two main strike directions at N-S and E-W. The attitude of the bedding in this area is N50W/14SW. Traverses 7 and 8 on the southern end of the monocline where the attitude of the bedding is N19E/27NW also show a scatter in deformation band orientations with dominant strike direction around E-W.

a)

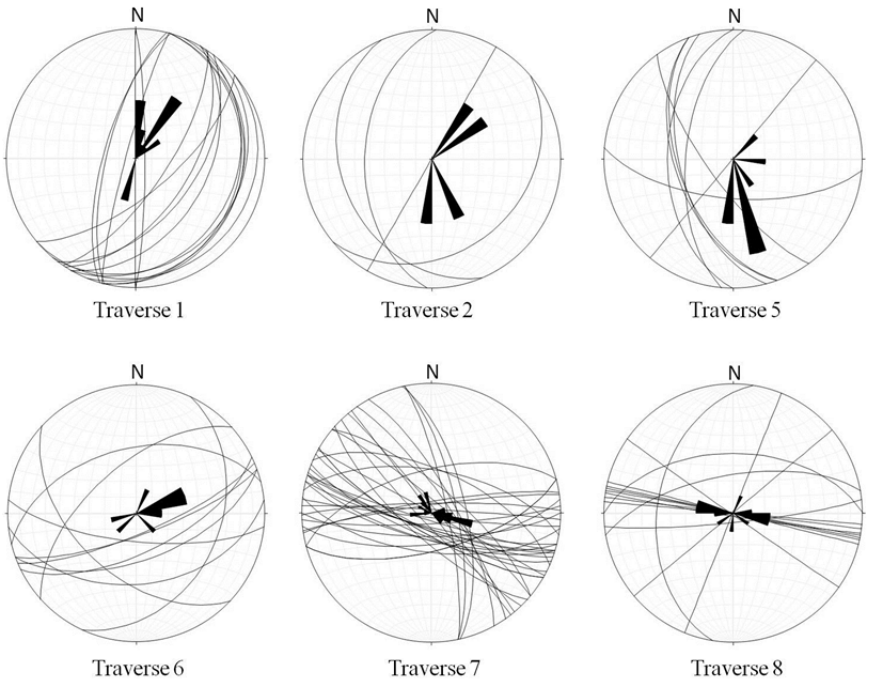

b)

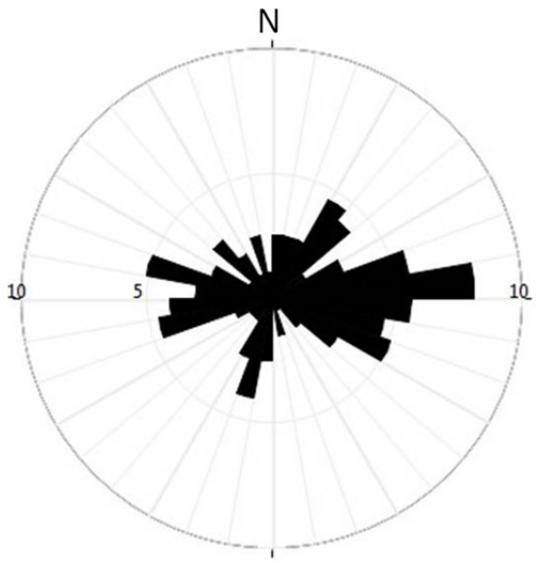

Figure 5.1: a) Deformation band orientation by traverse and b) overall strikes of deformation bands in the study area. The letter N indicates north direction.

Overall strikes of deformation bands in the study area including the points around the traverses is shown on a rose diagram in Figure 5.1 (b) where the numbers are shown in percentages. The variability in deformation bands' strikes is observed; however, a dominant strike direction can be defined around E-W. The minor axis of deformation bands' strikes is

around N30E. Velocity measurements are expected to reflect anisotropy at the locations where E-W deformation bands' strike directions are prominent. Near the fault, velocities are expected to be faster in N-S direction since more deformation bands strike subparallel to the fault. At the locations near the monocline, it is unclear whether anisotropy can be observed since there is no preferred orientation of deformation bands' strikes.

5.2 Velocity Acquisition

5.2.1 Layout for Velocity Measurements

Ultrasonic velocity measurements were collected across eight traverses that coincide with the traverses for deformation band density acquisition. An ultrasonic velocity measurement system that consists of portable transducer gun, controller, and oscilloscope was used in data acquisition. The system's description can be found in Appendix A. The transducer gun constitutes a set of one receiver and two transmitters arranged in line (Figures A.1 and A.3). The distance between each sensor is 2.54 cm. One of the receivers adjusts vertically with the use of a spring to ensure a good three-point contact with an uneven surface.

A photo of a velocity measurement station on Traverse 4 is shown as an example in Figure 5.2. Both Vp and Vs velocity measurements were obtained in N-S and E-W directions. Two sets of Vp and Vs are recorded at each meter of the traverse. The location of each measurement is marked with two orthogonal black lines that indicate measurement direction. Photographs of each of measurement station can be found in Appendix B.

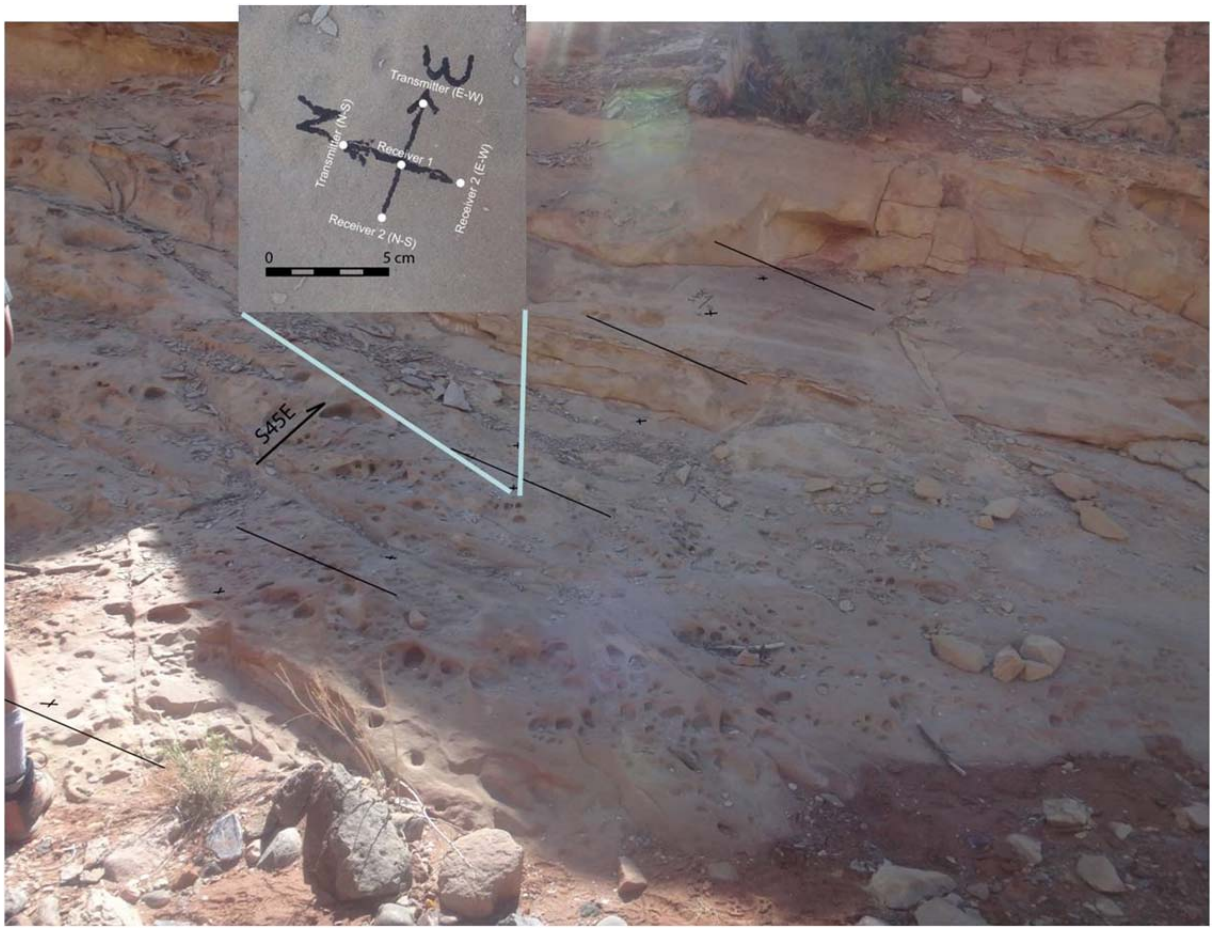

Figure 5.2: An example of layout for velocity acquisition. Orthogonal black lines represent the points oriented N-S and E-W where velocity was measured.

5.2.2 Error Analysis in Field Velocity Acquisition

Several sources of uncertainty in velocity measurement associated with the accuracy of recorded results are identified:

1) An uncertainty in the distance between the receivers (2.54 cm apart) accounts to +/- 0.01cm. Since the design of the transducer gun does not allow for a change in the receiver separation, this uncertainty leads to a systematic error in all of the measurements.
2) An uncertainty associated with resolution of acquired signal is related to the frequency of a signal. In ultrasonic measurements, typical frequency is 20 – 200 kHz (Li et al., 2011). The sample rate of the measurement is defined by the concept of Nyquist frequency:

$$Sample\ rate = \frac{1}{2*f_{nyq}} = \frac{1}{4*f_{max}} \quad (5.1),$$

where f_{nyq} – Nyquist frequency and f_{max} is the highest signal frequency (Liner, 2004).

From the equation (5.1), the sample rate for ultrasonic frequency measurements is 1.25 μs, so the uncertainty in the measurement is +/- 1.25 μs.

The major source of error is associated with the uncertainty (2) since it is random. Time difference between the signal arrivals on both receivers varied between 7.0 – 13.8 μs for P-wave measurements and 10.6 – 18.8 μs for S-wave measurements. The percent uncertainty in the measurement is, thus, 9 – 18% for Vp and 7 – 12 % for Vs where the uncertainty in faster velocity drifts towards the higher percentage value.

5.3 Results of the Measurements

Acquired measurements were examined to clean out erroneous data points and plotted as velocity versus distance from the fault (Figure 5.3). Five clusters of data points are observed around 16 m, 91 m, 195 m, 438 m, and 473 m. The cluster within the first 16 m located next to the fault core has the lowest velocities across the traverse for both P- and S-waves. P- and S-velocities also slightly drop towards the southern end of the monocline where the curvature of the monocline is higher.

In order to quantify the amount of anisotropy between N-S and E-W direction, the

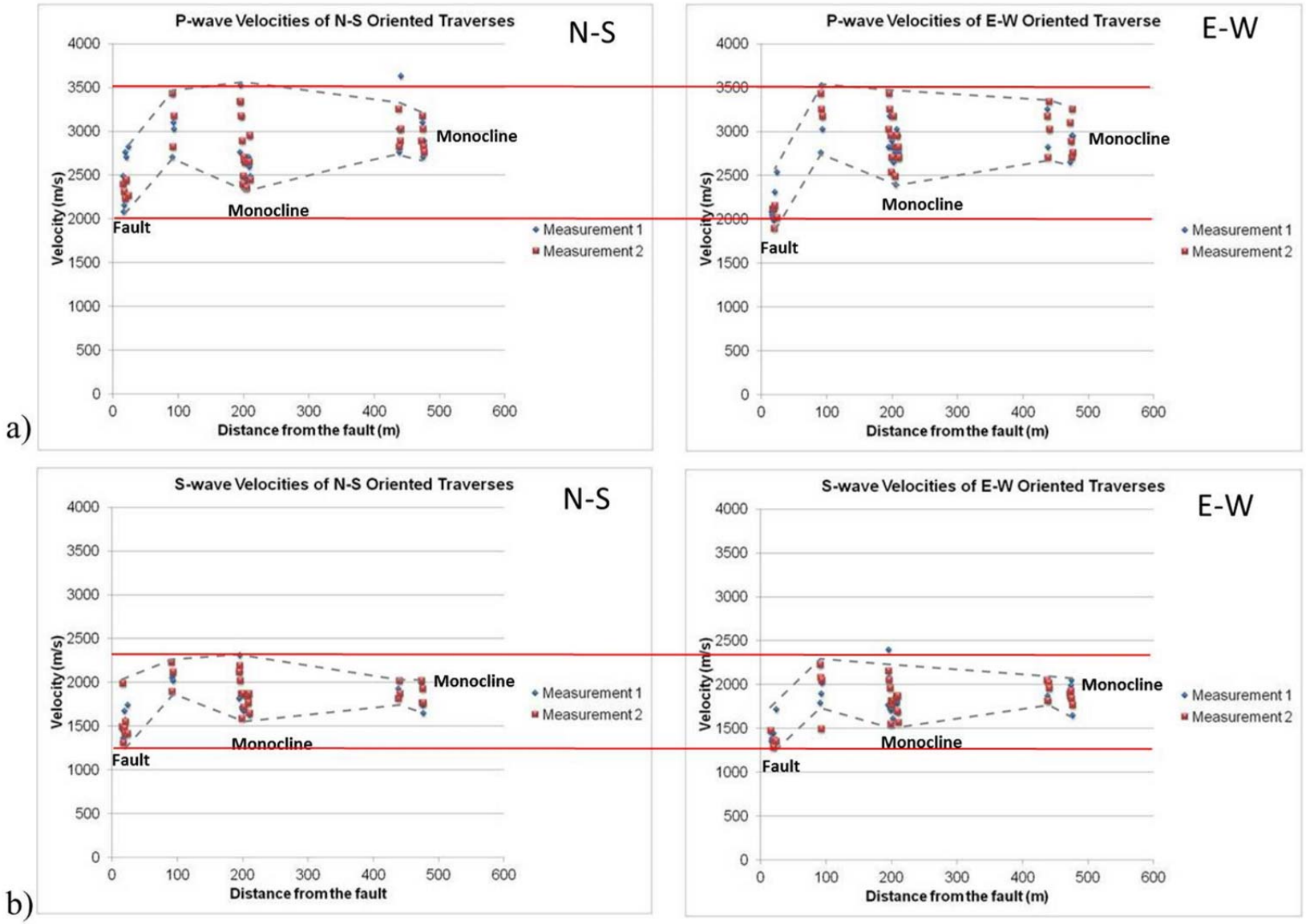

Figure 5.3: Comparison of a) Vp measurements and b) Vs measurements in N-S and E-W orientation. Anisotropy associated with deformation bands is observed for measurement points near the fault.

obtained velocity measurements at each location were averaged. Then, the average values of the velocity in N-S and E-W directions were used to find a ratio of fast to slow velocity as shown below:

$$\frac{Vfast-Vslow}{Vfast} \quad (5.2),$$

(Treadgold et al., 2011).

Fraction difference in velocity measurements for N-S and E-W directions averaged at each location described above is summarized in Table 5.2. Out of five locations, the largest value of anisotropy is observed 16 m away from the fault where the difference between Vp measurements in N-S direction is 13% larger than in E-W direction. Since the P-wave velocity in this area is the lowest, the percent of uncertainty in measurement is the smallest. Thus, the measurement points near the fault are potentially exhibiting a weak anisotropy. The difference in Vs measurements is also larger in N-S direction and amounts to 7% which is smaller than the percent uncertainty, so the S-wave anisotropy is not detectable. At the location near the fault, the largest amount of deformation bands is observed (Figure 4.9 in Chapter 4), and the deformation bands have a preferred orientation around N-S (Figure 5.2(a)). For the remaining locations, the velocity difference is between 1 – 3 % for both Vp and Vs measurements and is smaller than the percent uncertainty. Thus, it was concluded that the difference between E-W and N-S orientation are due to the measurement error, and no velocity anisotropy is observed.

Table 5.2: Fraction difference in velocity measurements averaged at different points along the traverse.

Distance from the fault (m)	Vp fraction difference	Vs fraction difference	Fast direction
16	0.13	0.07	N-S for both Vp and Vs
91	0.03	0.01	E-W for Vp and N-S for Vs
195	0.03	0.03	E-W for Vp and N-S for Vs
438	0.03	0.01	E-W for both Vp and Vs
473	0.01	0.02	N-S for Vp and E-W for Vs

6. LINKING VELOCITY WITH PETROPHYSICAL PROPERTIES

6.1 Laboratory Measurements and Their Comparison to the Field Results

Seven samples from different parts of the study area were acquired for petrophysical properties determination and calibration with field velocity data (Figure 6.1). It was only possible to produce cores out of samples 1, 2, 3, 6 and 7. Samples 4 and 5 crushed during coring as the rock surrounding deformation bands was too soft. Porosity, permeability, and Vp and Vs velocities were obtained from the cores of the remaining samples. Porosity was measured with a gas-porosimetry method using helium gas. Permeability was determined with gas permeability method where nitrogen gas was used. Ultrasonic velocities were acquired under 10 MPa confining pressure. The description of methods and equipment can be found in Appendix A. The results are summarized in Table 6.1.

Figure 6.1: Samples collected for coring; locations of the samples are indicated with red asterisks in Figures 2.2 and 4.6.

Table 6.1: Rock properties measured for each sample. The first digit indicates the number of the sample from which the core was extracted. Velocities are measured at 10 MPa confining pressure.

Sample #	Distance from fault (m)	Porosity (%)	Permeability (md)	Vp (m/s)	Vs (m/s)
1-1	837	33		2820	1720
1-4	837	34	2730		
2-1	16	25		3250	2020
2-2	16	29	75.6	2800	1700
3-1	91	26	308	3140	1950
3-2-1	91	27	607	2723	1667
3-2-2	91	27		3210	2040
3-3	91	26	274	2674	
3-4	91	27	492	2639	
6-1	195	26	659	2048	
7-3	205	25	927	2374	
7-4	205	24	887	2467	1695
7-5	205	23	459	2732	1385

Comparison of field and lab velocities is shown in Figure 6.2. Laboratory velocity measurements are consistent with field data, except for the points near the fault where lab velocities are slightly higher. The velocity difference between field and lab samples can be attributed to the higher rock disturbance near the fault which lead to formation of microfractures that closed under applied pressure in the lab experiments resulting in higher rock velocities.

a)

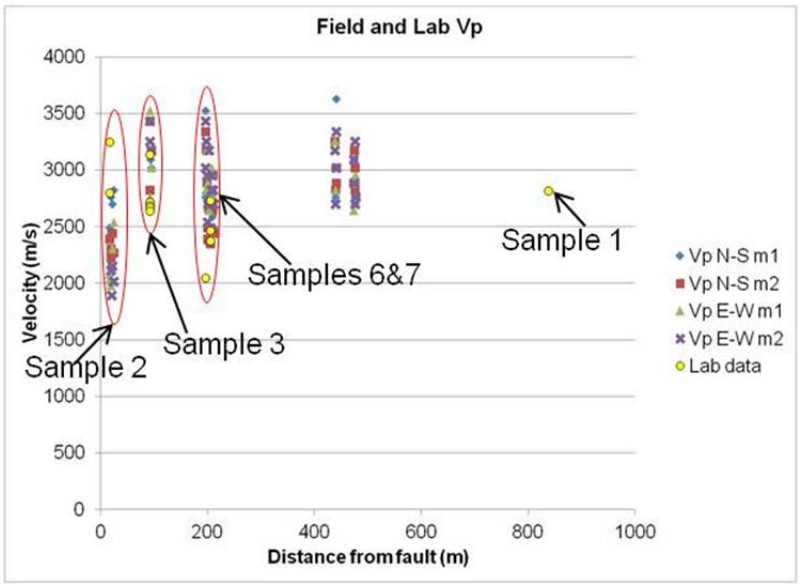

b)

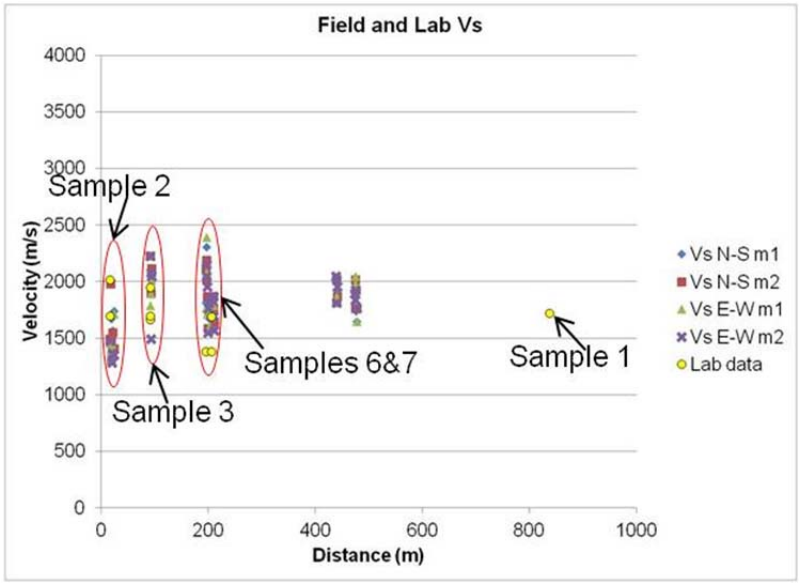

Figure 6.2: Comparison of laboratory and in-situ velocity measurements.

6.2 Sources of Error in Lab Velocity Measurements

Sources of error in the measured lab velocities similar to the one outlined in Section 5.2.2 of Chapter 5 are identified where 1) an uncertainty in measured length of the core and 2) signal resolution are assessed. Unlike field velocity data, lab samples had a variable length ranging from 4.030 – 5.426 +/- 0.001 cm. The same uncertainty of +/-1.25 μs associated with picking the first break for signal arrival.

6.3 Velocity – Porosity Relationship in the Laboratory Samples

6.3.1 Vernik and Kachanov (2010) Sand Diagenesis Model

Vernik and Kachanov (2010) empirical model for sand diagenesis is used to establish velocity-porosity relationship (Figure 6.3). The model recognizes two different mechanisms of diagenesis based on porosity. The first part of the model is constructed for consolidated rocks with porosity values up to 0.3 or less where the change in velocity with porosity is controlled by the density of microfractures and pore geometries which are determined from empirical data (Vernik and Kachanov, 2010). The parameter defining density of microfractures is expressed as:

$$\eta(\sigma) = \eta_0 \exp(-d\sigma) \quad (6.1),$$

where $\eta_0 = 0.3 + 1.6\phi$ - density of microfractures at zero stress,

$d = 0.02 + 0.003\sigma$ - compaction coefficient (MPa)

ϕ - porosity (Vernik and Kachanov, 2010).

The empirical constants *p* and *q* defining pore geometries are:

$$p \cong q = 3.6 + b\phi \quad (6.2),$$

where *b* can vary between 8 and 12 (Vernik and Kachanov, 2010).

An equation for the consolidated sands model is in the form:

$$M_d = M_m\left(1 + p\frac{\phi}{1-\phi} + 1.94\frac{\eta_0 \exp(-d\sigma)}{1-\phi}\right)^{-1}$$

$$G_d = G_m\left(1 + q\frac{\phi}{1-\phi} + 1.59\frac{\eta_0 \exp(-d\sigma)}{1-\phi}\right)^{-1} \quad (6.3),$$

where M_d - P-wave modulus of a dry rock,

M_m - P-wave modulus of rock matrix,

G_d - S-wave modulus of a dry rock,

G_m - P-wave modulus of rock matrix (Vernik and Kachanov, 2010).

A change in the model occurs when it reaches consolidation porosity (~0.2 - 0.3) after which the rock is considered unconsolidated. Transition from consolidated to unconsolidated sands is characterized by a sharp bend at the consolidation porosity value due to faster rate of change of velocity with porosity in unconsolidated rock (Vernik, 1997). The following equations are used to construct the model:

$$M_d = M_{con}\left(1 - \frac{\phi - \phi_{con}}{\phi_c - \phi_{con}}\right)^2$$

$$G_d = G_{con}\left(1 - \frac{\phi - \phi_{con}}{\phi_c - \phi_{con}}\right)^{2.05} \quad (6.4),$$

where M_{con} and G_{con} are the dry moduli calculated for consolidated model (Equation 6.3),

ϕ_{con} - consolidation porosity at which the switch between consolidated and unconsolidated models occurs,

ϕ_c - critical porosity at which the grains are in suspension (40%) (Vernik and Kachanov, 2010).

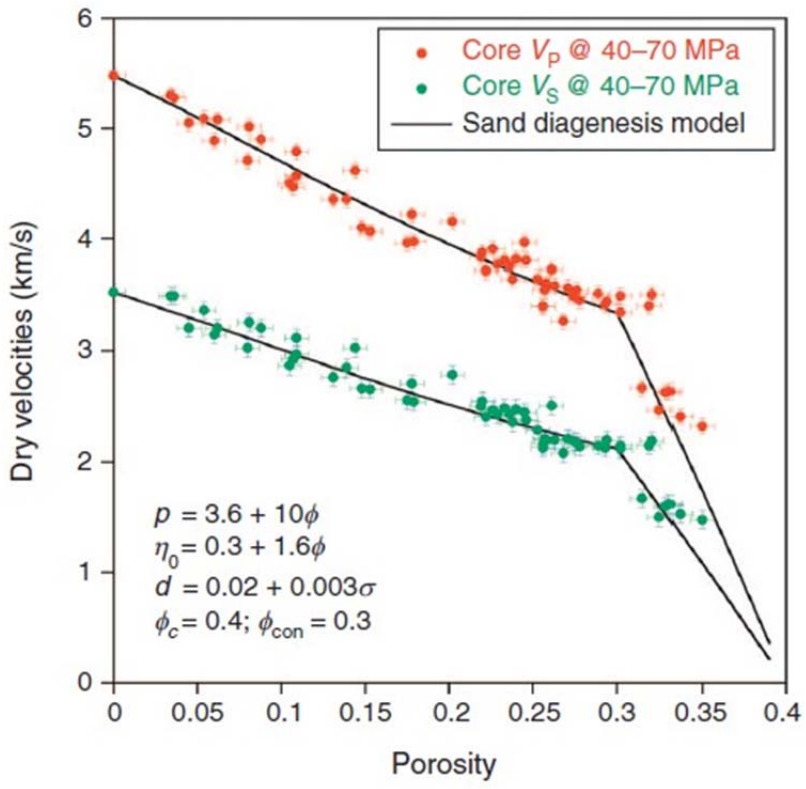

Figure 6.3: Sand diagenesis models from core Vp and Vs data. The change from consolidated to unconsolidated model occurs at consolidation porosity (30 % for this example) at the point where the slope of the line becomes steeper (Vernik and Kachanov, 2010).

While the consolidated model is affected by both pore shapes and microfractures, the unconsolidated model mostly depends on the pore shapes that indicate the degree of compaction (Vernik and Kachanov, 2010). To assess the degree of compaction, the modeling with varying empirical coefficients of pore shapes (p and q) to fit the observed data is performed with the following equations:

$$M_d = M_m\left(1 + p\frac{\phi}{1-\phi}\right)^{-1}$$

$$G_d = G_m\left(1 + q\frac{\phi}{1-\phi}\right)^{-1} \quad (6.5)$$

where $p = q$ - empirical parameters that represent the degree of compaction; larger values of p and q are associated with higher porosity (Vernik and Kachanov, 2010).

6.3.2 Construction of Diagenesis Models for the Core Samples

Dry rock moduli in equation 6.5 were computed by varying p and q parameters for a porosity range of 0.01 - 0.4. These values along with Gassmann's fluid substitution equations were used to determine air-saturated P- and S-wave moduli (M_{sat} and G_{sat}) from which rock velocities were calculated. Figure 6.4 shows modeled curves for pore shape factors of 10, 14, 18 and 24 overlain by measured lab velocity versus porosity data. It is interesting to note that shape factors for the samples 2 and 3 located near Cañones fault are higher than the pore shape factors for samples 6 and 7 near the monocline for both Vp and Vs.

a)

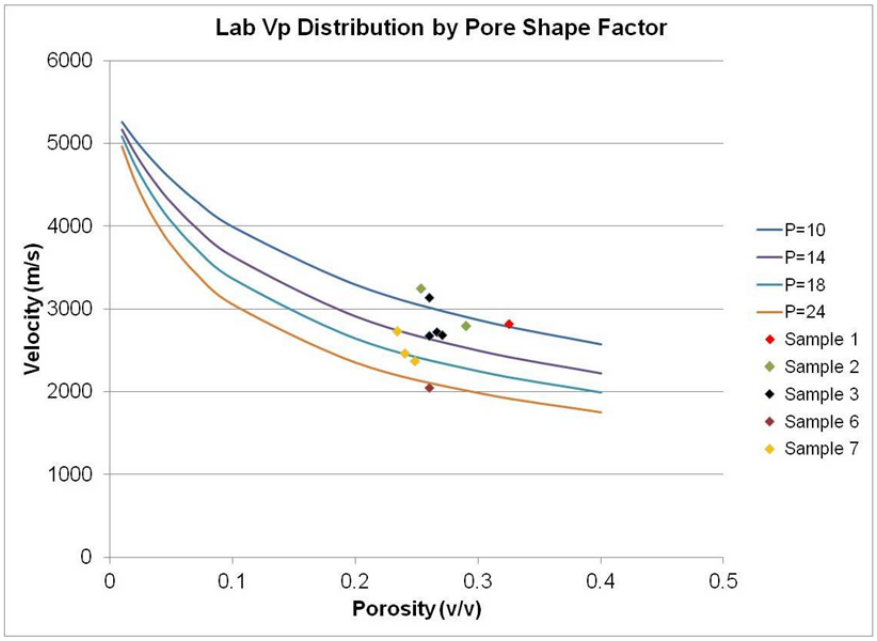

b)

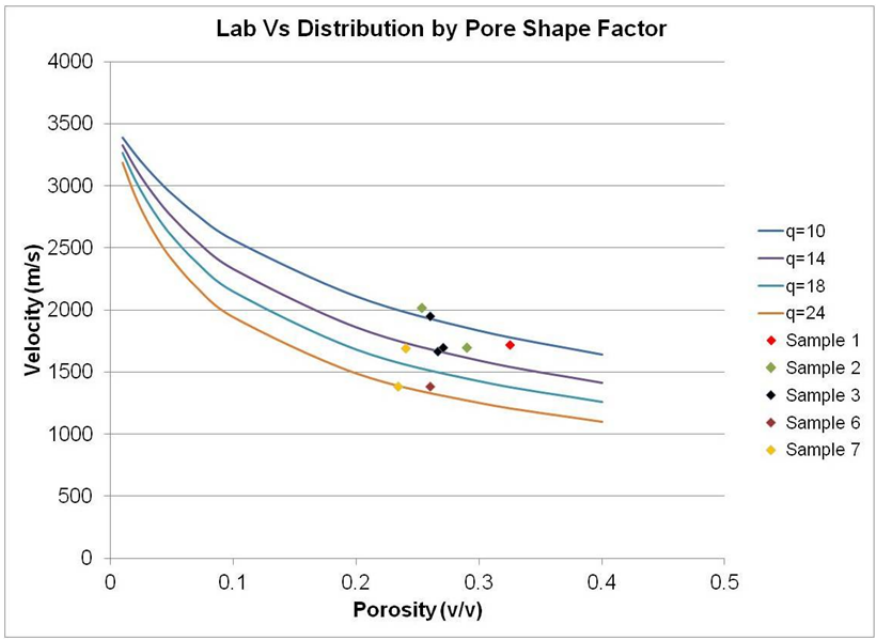

Figure 6.4: Distribution of a) P-wave velocity and b) S-wave velocity versus porosity by pore shape factors. The data points for samples 2 and 3 located near Cañones fault have higher p and q parameters than the data points for samples 6 and 7 near monocline. Two distinct compaction groups based on pore shape factors are observed.

Two distinct compaction groups associated with the fault and the monocline can be recognized, for which separate sand diagenesis models were constructed (Figure 6.5). Sand diagenesis models were built to establish Vp and Vs velocity- porosity relationship (Figure 6.5) at 0.2 consolidation porosity (points near the monocline) and 0.25 consolidation porosity (points near the fault). The equations for the porosity estimations for these two groups are provided below:

1) Group 1 (near the monocline; consolidation porosity = 0.2):

$$Vp = -4538 * \ln(\phi) - 3929$$

$$Vs = -3203 * \ln(\phi) - 2923.7 \quad (6.6).$$

The porosity from these equations is estimated as:

$$\phi = \exp\left(\frac{Vp+3929}{-4538}\right) = \exp\left(\frac{Vs+2923.7}{-3203}\right) \quad (6.7).$$

2) Group 2 (near the fault; consolidation porosity = 0.25):

$$Vp = -6263 * \ln(\phi) - 5564.6$$

$$Vs = -4394 * \ln(\phi) - 4037.4 \quad (6.8).$$

The porosity is then:

$$\phi = \exp\left(\frac{Vp+5564.6}{-6263}\right) = \exp\left(\frac{Vs+4037.4}{-4394}\right) \quad (6.9).$$

From the equations (6.7) and (6.9), it is apparent that knowing one of parameters (Vp, Vs or porosity) one can estimate the two remaining parameters.

a)

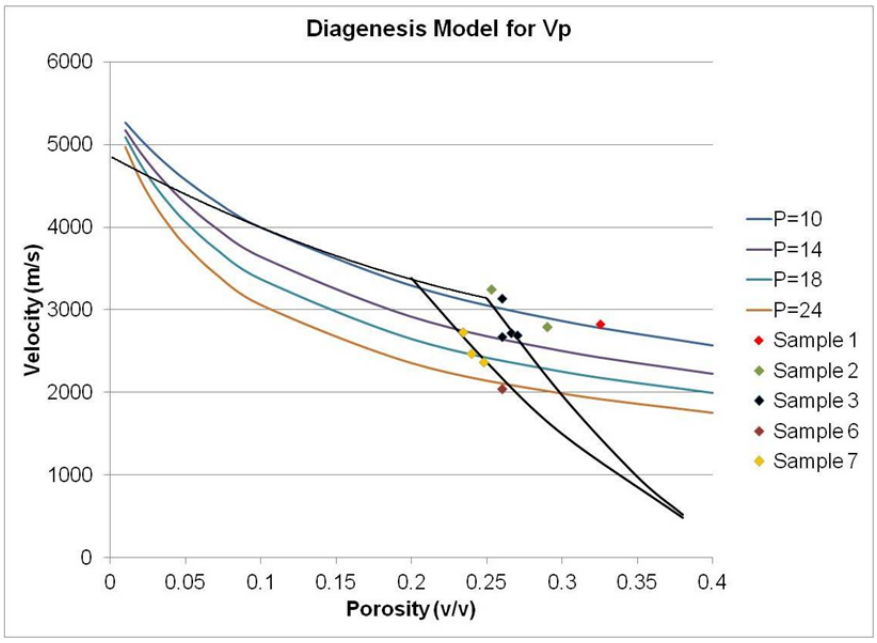

b)

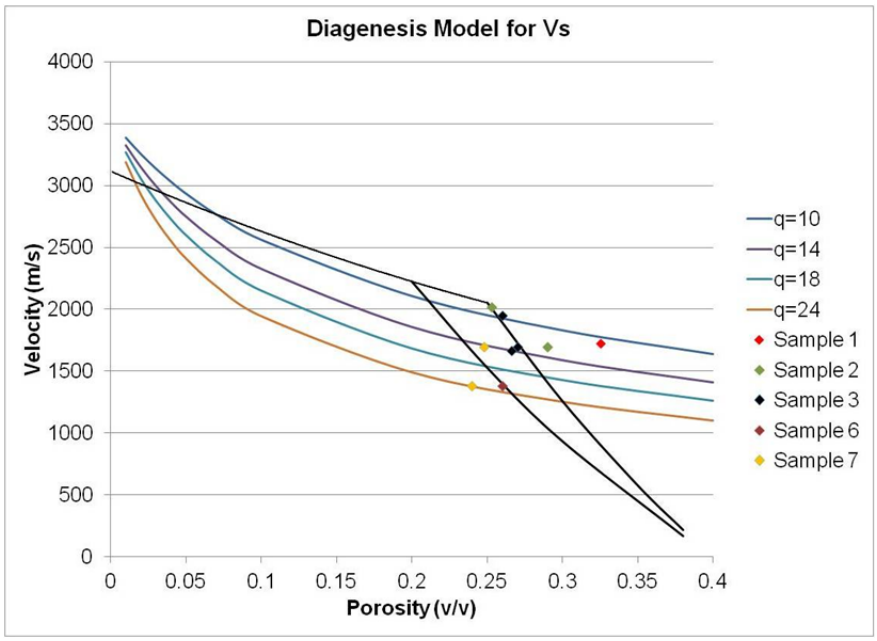

Figure 6.5: Diagenesis models for the group of points near the fault (samples 2 and 3) and near the monocline (samples 6 and 7). The trends are used to estimate a) porosity from Vp and b) porosity from Vs data.

6.3.3 Porosity Prediction of Field Velocity Data Based on Established Correlations

The relationships between porosity and velocity established in equations (5.4) and (5.6) are applied to the in-situ measured velocities for porosity prediction. Estimated porosity values for the field data are found in Table C.2 of Appendix C where estimations with both Vp and Vs

models were made. The porosity estimations with Vp were crossplotted against the porosity estimations with Vs to verify that both models produce the same result. Figure 6.6 shows the results of the comparison where the black line at 45° to the horizontal and vertical axes marks one-to-one match between the approximations. If a good match between the approximation with Vp and approximation with Vs is achieved, the point should fall on this line or close to it which is seen for the most of the data points. The exception to this trend is a set of E-W-oriented measurement points that form another linear trend where the porosity estimation with Vs is higher than the porosity estimation with Vp. The Table C.2 shows that the locations of the points where this discrepancy is observed are near the fault. These measurement points also exhibit the highest amount of anisotropy (Table 5.2) where the E-W direction is associated with slow P- and S-wave propagation.

The equation obtained from the slope of the line where the outliers fall corrects the mismatch in estimated porosity due to anisotropy as shown below:

$$\phi(Vs) = 0.75\phi(Vp) + 0.105 \tag{6.10}$$

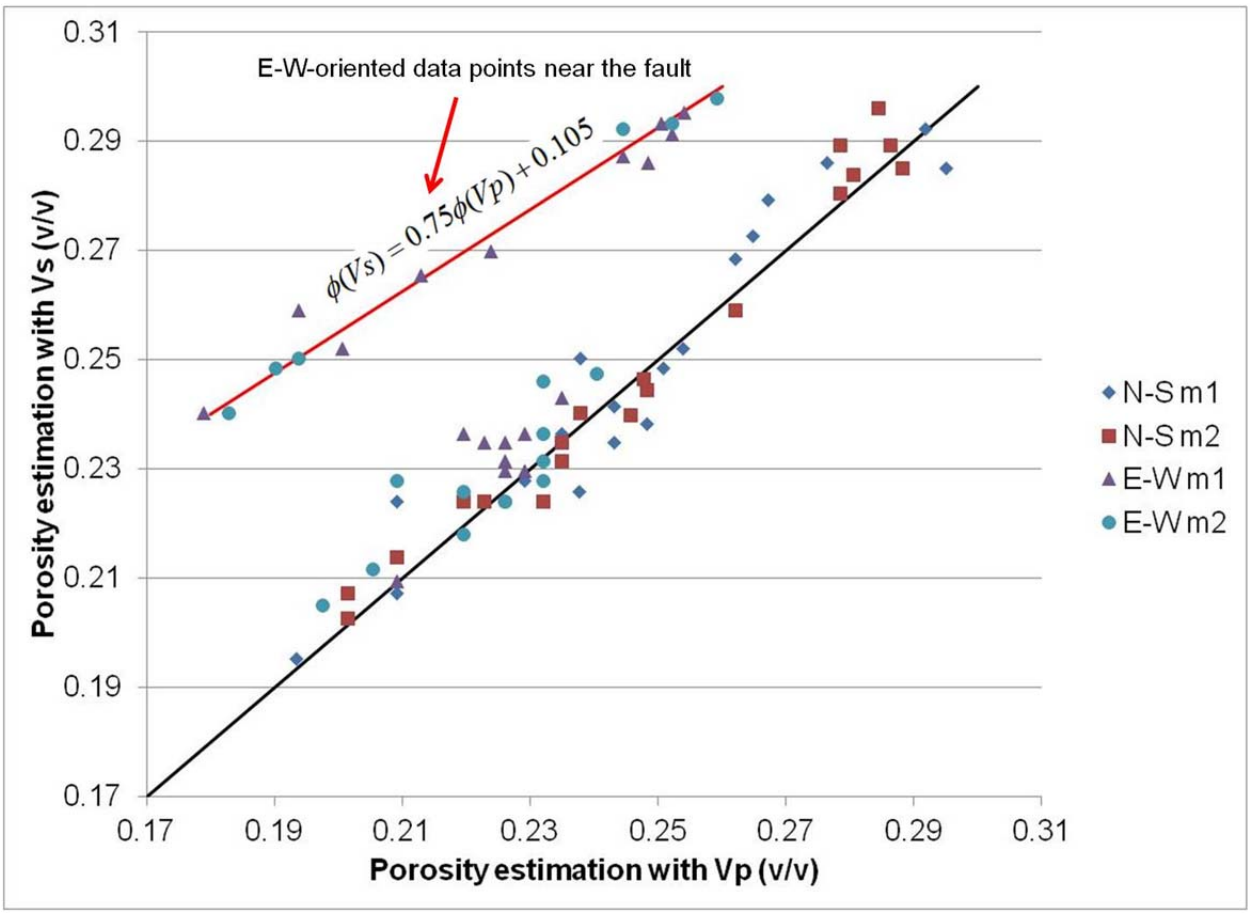

Figure 6.6: Quality check of estimated porosity with Vp versus estimated porosity with Vs for the in-situ velocities. Expected one-to-one relationship for both estimations is observed for most of the data. A deviation from the trend is observed for the data points near the fault.

6.4 Permeability Versus Porosity in Lab Samples

Permeability measured in core samples is highly variable. Permeability data measured in the lab samples were plotted against porosity to determine whether correlation between these two properties exist (Figure 6.7). The data points are scattered, and no evident correlation is present. Therefore, it was concluded that porosity is not related to permeability for the collected samples. The lack of correlation could be due to insufficient number of permeability measurements available.

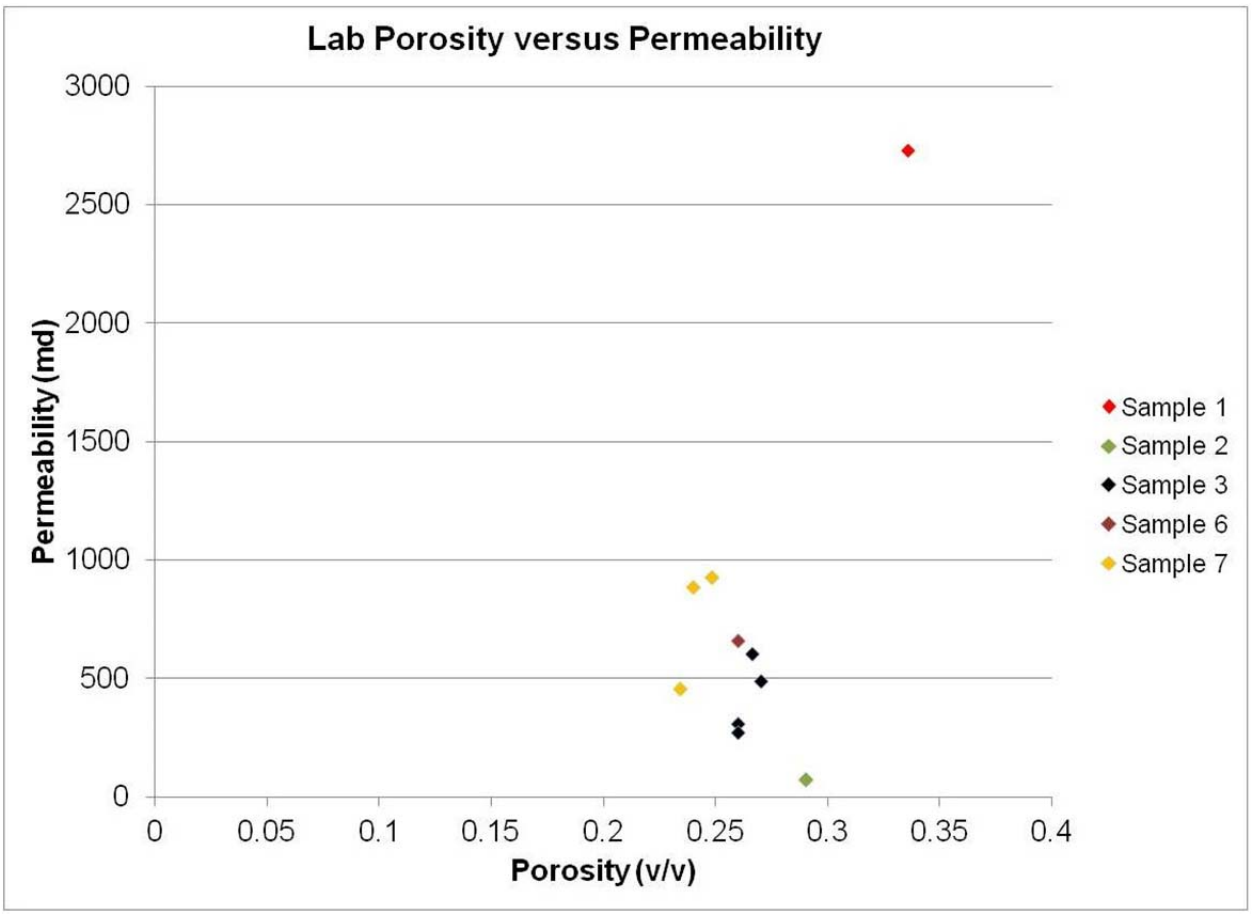

Figure 6.7: Plot of core porosity versus permeability. Correlation between these properties is not observed possibly due to a small number of sample points.

7. DISCUSSION

7.1 Mechanism of Deformation Bands' Development in the Study Area

Overview of the deformation types and their petrophysical properties along with thin sections from the study area was done in Chapter 3. Porosity within the band and geometry of the grains within Entrada sandstone resembles cataclastic band type similar to the examples from Aydin and Johnson, 1978; Antonellini et al., 1994; Mair et al., 2000; etc. Microfractures and conchoidal fractures are observed within the deformation bands Estimated differential pressure based on the depth of burial of Entrada sandstone at the time of deformation bands' formation is between 9 and 27 MPa. Such pressure is too low compared to the experimental results of cataclastic bands' generation by Mair et al. (2000) where these features developed at 120 - 140 MPa differential pressure. The question is then how could these bands having the same appearance as cataclastic bands have been generated under low differential pressure conditions?

The preferred explanation is that the deformation bands observed in the area were the zones of high porosity due to dilational component of motion. The fractured grains have already been in place before deformation occurred. Instead of pore space collapse and cataclasis, the increase of pore space took place. Higher porosity within the band created the path for migration of fluids and finer grained material (Figure 6.1) until the band got truncated. The zones of deformation bands were created by repetitive small-offset sliding events along the weakness plane where generated fractures got filled in with smaller grained sediments until the major rupture event that created Cañones fault occurred.

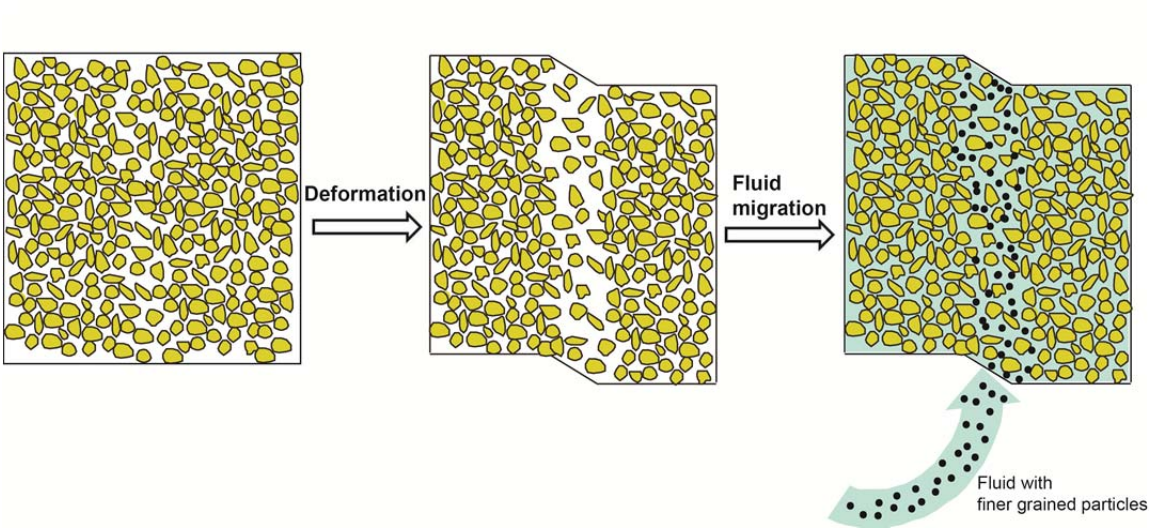

Figure 7.1: Formation of dilational disaggregation bands and their infill with finer grained material.

7.2 Effect of Laramide Structure on Cañones Fault

A noticeable feature that the study area exhibits is that the strike of the Cañones fault is coincident with the strike of the Laramide monocline (Chapters 2 and 4). Also, the larger throw is in the southern part of the fault where the monocline exhibits the largest amplitude. Both of the structures show less deformation towards the south. The fault is positioned to the west of the monocline where the curvature of monocline strata occurs. This observation leads to a conclusion that Cañones fault, if not reactivated Laramide structure, was initiated along the weakness plane defined by the monocline.

7.3 Correction of Porosity Estimation for In-situ Velocity Anisotropy

Velocity anisotropy detected near Cañones fault produced inconsistent porosity estimations from Vp and Vs velocities using Vernik and Kachanov (2010) model (Chapter 6). Estimated porosity for E-W-oriented measurements near the fault shows lower values from Vp model than from Vs model. This discrepancy in porosity estimation shows a linear trend (Figure 5.10). In order to determine which approximation is more reliable, the following observations were taken into consideration:

1) Porosity is defined as the ratio of pore volume (V_{pore}) to the bulk volume of the rock (V_b) such that:

$$\phi = \frac{V_{pore}}{V_b} \quad (7.1),$$

(Cone and Kersey, 1992). As seen from the above equation, porosity is the volume property and is not dependent on the sample orientation.

2) Weak P-wave anisotropy (13%) for the field data in this area was observed.
3) Porosity estimations from both Vp and Vs models show similar results in this area that are independent of measurement orientation (Table C.2), except for the porosity estimated from Vp for E-W-oriented measurements.

Based on these observations, porosity from Vs for E-W oriented measurements near the fault was considered a better approximation. The equation (6.10) shows a correction that accounts for anisotropy when estimating porosity from Vp.

Validation of the constructed models for porosity estimation is based on the consistency of the results. No porosity data were acquired in situ to compare with the estimated values which opens up the opportunity for further research. Another potential point of interest is the statistical significance of the available data used to construct the models, i. e. whether these models would show similar results on larger datasets. Furthermore, this study shows that anisotropy associated with the preferred strike orientations of deformation bands is detected with ultrasonic velocity measurements; this finding can be tested on a larger scale, such as seismic dataset.

8. CONCLUSIONS

During the course of this research, the following issues associated with deformation bands in the study area have been addressed:

1) Structures observed in the study area in relation to each other: A monocline of Laramide age and Cañones fault related to Rio Grande extension are the two major structures in the study area that are subparallel to each other. Their orientation relative to each other is not coincidental. It suggests that Cañones fault ruptured along the zone of weakness created by the monocline.

2) Type of deformation bands and their effect on petrophysical properties in the study area: Entrada thin sections were analyzed to determine the effect of deformation bands on porosity. Porosity within the deformation band is significantly reduced. The proposed mechanism of their formation involves pore space increase within the band and migration of smaller particles carried with fluids into open pore space.

3) Deformation bands' density and orientations, and their relation to the main structures: Deformation band density strongly correlates with the proximity to the fault and monocline. Near these structures, high deformation band density is observed. Deformation band density drops away from the fault and monocline. Deformation bands near the fault are aligned preferentially subparallel to the strike of the fault. Near the monocline, a variation in deformation bands' orientation is observed due to multiple deformation band sets generation associated with bending in different parts of the monocline.

4) Porosity versus velocity relationship in the study area: Core samples from different parts of the study area were used for velocity-porosity calibration. Established

trend was applied to in-situ velocity measurements for porosity estimation. Porosity trend established from Vp predicted the same porosity values as he trend established from Vs for most of the samples which provided confidence in constructed models. The samples near the fault that exhibited anisotropy produced a linear error in porosity estimation from Vp versus porosity estimation from Vs. A correction equation that scaled the porosity from Vp estimations to porosity from Vs estimation was established.

REFERENCES

Allmendinger, R. W., Cardozo, N. C., and Fisher, D., 2012, Structural Geology Algorithms: Vectors & Tensors: Cambridge, England, Cambridge University Press, 289 p.

Antonellini, M. and Aydin, A., 1995, Effect of faulting on fluid flow: geometry and spatial distribution: AAPG Bulletin 79 (5): 642-671.

Aydin, A. and A. M. Johnson, 1978, Development of faults as zones of deformation bands and as slip surfaces in sandstone: Pageoph 116, 931 – 942.

Baldridge, W. S., J. F. Ferguson, L. W. Braile, B. Wang, K. Eckhart, D. Evans, C. Schultz, B. Gilpin, G. R. Jiracek, and S. Biehler, 1994, The western magin of the Rio Grande Rift in Northern New Mexico: An aborted boundary?: GSA Bulletin 106, 1538 – 1551.

Berg, S. S. and Skar, T., 2005, Controls on damage zone asymmetry of a normal fault zone: outcrop analyses of a segment of the Moab fault, SE Utah: Journal of Structural Geology 27, 1803 – 1822.

Bergbauer, S. and D. D. Pollard, 2004, A new conceptual fold–fracture model including prefolding joints, based on field data from the Emigrant Gap anticline: Wyoming, Geological Society of America Bulletin 116, 294–307.

Biehler, S., J. Ferguson, W. S. Baldridge, G. R. Jiracek, J. L. Aldern, M. Martinez, R. Fernandez, J. Romo, B. Gilpin, L. W. Braile, D. R. Hersey, B. P. Luyendyk, and C. L. Aiken, 1991, A geophysical model of the Española Basin, Rio Grande rift, New Mexico: Geophysics 56 (3), 340 – 353.

Cone, M. P. and D. G. Kersey, 1992, Porosity: Part5. Laboratory Methods: AAPG Special Issues, ME 10, 204 – 209.

Crain's Petrophysical Textbook, Core permeability, http://www.spec2000.net/09-coreperm.htm.

Du Bernard, X., P. Eichhubl, and A. Aydin, 2002a, Dilation bands: A new form of localized failure in granular media: Geophysical Research Letters 29 (24), 29-1 – 29-4.

Du Bernard, X., P. Labaume, and O. Bour, 2002b, Cataclastic slip band distribution in normal fault damage zones, Nubian sandstones, Suez rift: Journal of Geophysical Research 107, B7, 6-1 – 6-12.

Engelder, J. T., 1974, Cataclasis and the generation of fault gouge: GSA Bulletin, 85, 1515 – 1522.

Erslev, E. A., and N. V. Koenig, 2009, Three-dimensional kinematics of Laramide, basement-involved Rocky Mountain deformation, USA: Insights from minor faults and GIS-enhanced structure maps: The Geological Society of America, Memoir 204, 125 – 150.

Flesch, G. A., 1974, Stratigraphy and sedimentology of the Morrison Formation (Jurassic), Ojito Spring quadrangle, Sandoval county, New Nexico: A preliminary discussion: New Mexico Geological Society Guidebook, 25th Field Conf., Ghost Ranch (Central-Northern N. M.).

Fredericks, K., L. Goodwin and H. Tobin, 2013, Petrophysical properties of a deformation band fault zones in the Entrada sandstone, Utah: Search and Discovery Article #50861.

Fossen, H., R. A. Schultz, Z. K. Shipton, and K. Mair, 2007, Deformation bands in sandstone: a review: Journal of the Geological Society, London 164, 1 – 15.

Fossen H. and A. Bale, 2007, Deformation bands and their influence on fluid flow: AAPG Bulletin 91, 1685 – 1700.

Golombek, M. P., G. E. McGill, and L. Brown, 1983, Tectonic and geologic evolution of Española Basin, Rio Grande rift: structure, rate of extension, and relation to the state of stress in the western United States: Tectonophysics 94, 483 – 507.

Han, D., A. Nur and D. Morgan, 1986, Effects of porosity and clay content on wave velocities in sandstones: Geophysics 51 (11), 2093 – 2107.

Ingersoll, R. V., 2001, Structural and stratigraphic evolution of the Rio Grande rift, Northern New Mexico and Southern Colorado: International Geology Review 43, 867 – 891.

Kelley, S. A., G. R. Osburn, C. Ferguson, J. Moore, and K. Kempter, 2005, Preliminary geologic map of the Cañones Quadrangle, Rio Arriba county, New Mexico: New Mexico Bureau of Geology and Mineral Resourses Open-file Digital Geologic Map OF-GM 107.

Klein, C. and B. Dutrow, 2007, Mineral Science: Jon Wiley and Sons Inc., New Jersey, 675 p.

Kolyukhin, D., Schueller, S., Espedal, M. S., and Fossen, H., 2009, Deformation band populations in fault damage zone – impact on fluid flow: Comput. Geosci., 14, 231 – 248.

Li, T., J. Ma and A. F. Low, 2011, Horn-type piezoelectric ultrasonic transducer: modelling and applications: Advances in Piezoelectric Transducers, Dr. Farzad Ebrahimi (Ed.), ISBN: 978-953-307-931-8, InTech.

Liner, C. L., 2004, Elements of 3D Seismology, 2nd ed.: PennWell Corporation.

Magnani, B., A.R. Levander, E.A. Erslev, N. Bolay-Koenig, and K.E. Karlstrom, 2005, Listric thrust faulting in the Laramide from north-central New Mexico guided by Precambrian basement anisotropies: in Karlstrom, K.E. and Keller, G.R., editors, The Rocky Mountain Region - An Evolving Lithosphere: Tectonics, Geochemistry, and Geophysics: American Geophysical Union Geophysical Monograph 154, p. 239 – 252.

Mair, K., I. Main, and S. Elphick, 2000, Sequential growth of deformation bands in the laboratory: Lournal of Structural Geology 22, 25 – 42.

Maldonado, F., 2008, Geologic map of the Abiquiu Quadrangle, Rio Arriba county, New Mexico: USGS.

Maldonado, F. and S. A. Kelley, 2009, Revisions to the stratigraphic nomenclature of the Abiquiu Formation, Abiquiu and contiguous areas, north-central New Mexico: New Mexico Geology 31 (1), 3 – 8.

Nelson, R. A., 2001, Geologic analysis of naturally fractured reservoirs, 2nd. ed.: Boston, Gulf Professional Publishing, An Imprint of Elsevier, 332 p.

O'Keeffe, K., 2014, Geometry and kinematics of the Cañones Fault and the effects of lithology on the distribution of strain within the Cañones Fault damage zone: Master's Thesis, University of Houston.

Porosimeter Theory: Frank Jones and Associates.

Renard, R., E. Brosse and J. P. Gratier, 2000, The different processes involved in the mechanism of pressure solution in quartz-rich rocks and their interactions: Special Publications of the International Association of Sedimentologists, 67 – 78.

Rich, J. P. and M. Ammerman, 2010, Unconventional geophysics for unconventional plays: SPE paper 131779.

Saillet E. and C. A. J. Wibberley, 2010, Evolution of cataclastic faulting in high-porosity sandstone, Bassin du Sud-Est, Provence, France: Journal of Structural Geology 32, 1590 – 1608.

Shipton, Z. K. and P. A. Cowie, 2003, A conceptual model for the origin of fault damage zone structures in high-porosity sandstones: Journal of Structural Geology 25, 333 – 344.

Torabi, A., 2007, Deformation bands in porous sandstone their microstructure and petrophysical properties: PhD Dissertation, University of Bergen.

Torabi, A., H. Fossen, and A. Braathen, 2013, Insight into petrophysical properties of deformed sandstone reservoirs: AAPG Bulletin 97 (4), 619 – 637.

Treadgold, G., B. Campbell, B. McLain, S. Sinclair and D. Nicklin, 2011, Eagle Ford shale prospecting with 3D seismic data within tectonic and depositional system framework: The Leading Edge, January 2011, 48 – 53.

USGS Crustal Geophysics and Geochemistry Science Center, 2013, San Luis Basin Geophysics: http://crustal.usgs.gov/projects/rgb/SanLuisBasin/index.html

Vernik, L., 1997, Acoustic velocity and porosity systematics in siliciclastics: SPWLA 38th Annual Logging Symposium.

Vernik, L. and M. Kachanov, 2010, Modeling elastic properties of siliciclastic rocks: Geophysics 75 (6), E171 – E182.

Vincelette, R. R. and W. E. Chittum, 1981, Exploration for oil accumulation in Entrada sandstone, San Juan Basin, New Mexico: AAPG Bulletin 65 (12), 2546 – 2570.

Wawrzyniec T. F., J. W. Geissman, M. D. Melker, and M. Hubbard, 2002, Dextral shear along the eastern margin of the Colorado Plateau: A kinematic link between Laramide contraction and Rio Grande rifting (Ca. 75 – 13 Ma): The Journal of Geology 110 (3), 305 – 324.

Wild, P., 2011, Practical applications of seismic anisotropy: First Break 29, 117 – 124.

Zoback, M., 2010, Reservoir Geomechanics: Cambridge University Press, New York, 461 p.

A . MEASUREMENT EQUIPMENT AND METHODS

A.1 Portable Ultrasonic Velocity Measurement System

The equipment used in field velocity measurements consists of portable transducer gun, controller box, and oscilloscope (Figure A.1). Transducer gun has one transmitter and two receivers, 1 inch (2.54 cm) apart from each other. The first receiver, positioned in the middle, has a spring that adjusts its vertical position in order to ensure a good coupling with formation. The gun is connected to controller by four wires, three of which send the signal from transmitter and each receiver to the controller box, and the fourth wire sends the pulse from the controller box to the transmitter. The transmitter converts the pulse into a sound wave that propagates through the rock and gets picked up by two receivers. Transmitted and received signal is then sent to and digitized by controller. Digitized output signal from transmitter and both receivers can then be displayed on oscilloscope which is also connected to the controller.

Display output from two receivers presents sinusoidal waveforms, from which first arrival times are determined. Since receivers are separated by the distance of 2.54 cm, the first arrival on the second receiver shows later in time. Velocity is later computed from the receiver separation distance over the difference in time arrivals.

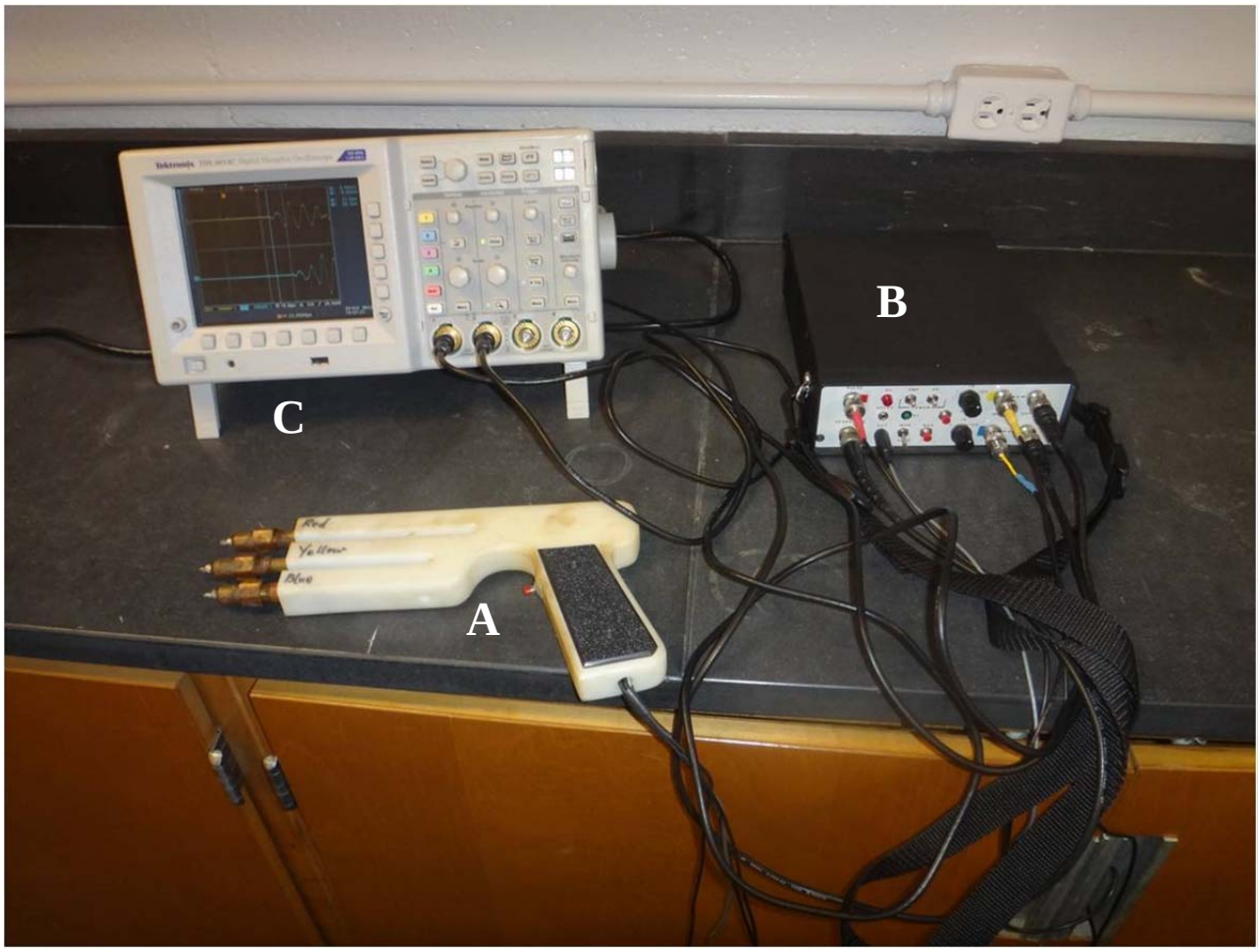

Figure A.1: Equipment connected for velocity measurement. A is a portable transducer gun with labels Red for transmitter, and Yellow and Blue for two receivers. B is a controller box that sends the electric pulse and receives the signal from the transducer gun. C is the oscilloscope where the digitized signal from the controller is displayed; two waveforms shown on the display are the signals obtained from the first (yellow) and second (blue) receivers.

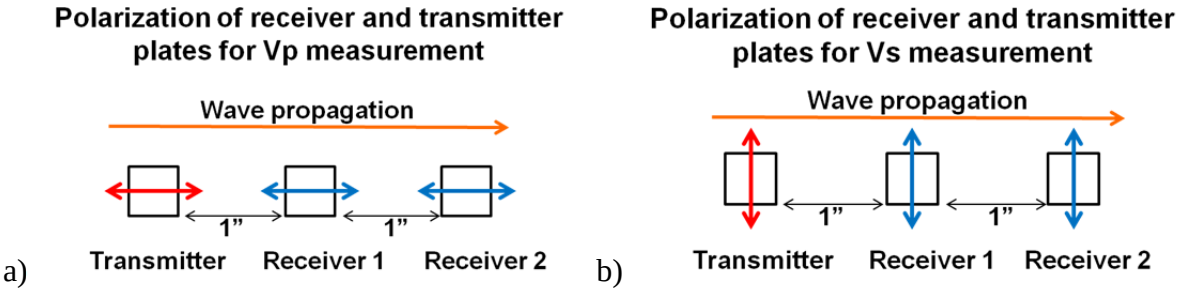

Figure A.2: A diagram of receiver and transmitter plates for measuring a) P-wave velocity where particle motion is parallel to wave propagation and b) S-wave velocity where particle motion is perpendicular to wave propagation.

Portable transducer gun is capable of measuring both P- and S-wave velocities. Figure A.2 shows schematic configurations of plate orientations in transmitter and receivers for obtaining these measurements. Rotation of the plates in parallel or perpendicular orientation to the wave propagation direction allows to measure P-wave or shear wave, respectively. Figure A.3a shows transducer gun plate orientations in P-wave acquisition mode. The arrow points to a dot circled in red that indicates the plate position. These plate position indicators are present on transmitter and each receiver. When the dots for all components of the transducer gun are aligned with letter P, it is ready to measure P-wave velocity. In order to change acquisition mode from P- to S-wave, the screws of the transducer gun shown in Figure A.3b need to be loosened. Then, the dots for all of the transducer components need to be rotated 90° clockwise and aligned with the caps of the screws. A reference position for S-wave acquisition mode is marked with letter S on one of the receivers. After rotation is complete, the screws need to be tightened again to start the measurement.

a) 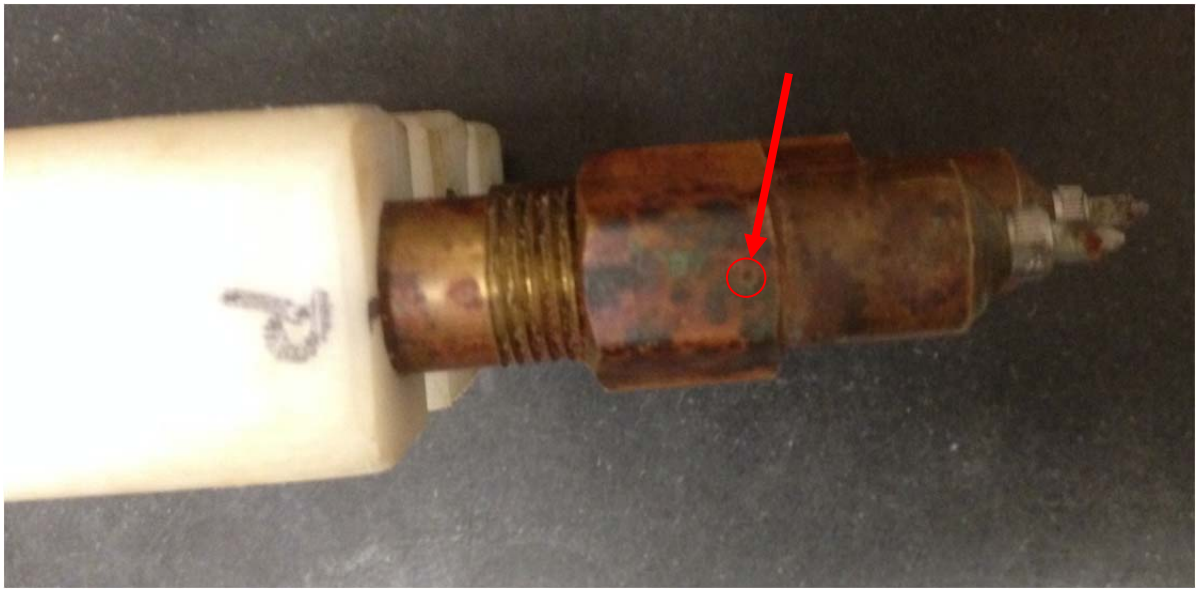

b) 

Figure A.3: a) Orientation of the plates in P-wave acquisition mode. The arrow points to the dot that indicates the position of receiver/transmitter plates that need to be aligned with letter P to start the acquisition. b) A view of transducer gun rotated 90°; for S-wave acquisition, all the dots indicating the plate position need to be aligned with the tops of the screws.

A.2 Cobberly-Stevens Porosimeter

Porosity measurement with the gas expansion method is based on the Boyle's law where, for a constant temperature, the product of pressure and volume remains constant. Cobberly-Stevens porosimeter is used for porosity measurement with gas expansion. The diagram of the porosimeter is provided in Figure A.4. This instrument (Figure A.5) consists of the sample cell with volume V_C and the reference section with volume V_R. The connection between the two sections is controlled by external valve. The pressure indicator is connected to the reference section. When the valve is closed, the reference section is filled with helium gas, and the gauge pressure, P_o, is displayed on the pressure indicator. The absolute pressure in the reference section

is the sum of the gauge (P_o) and atmospheric (A) pressures. The pressure - volume product in the reference section is $V_R(P_0 + A)$. The sample cell section contains the core sample with grain volume V_G which makes the total volume of the section equal to $(V_C - V_G)$.The pressure in the sample cell is the atmospheric pressure (A). The product of pressure and volume in the reference cell is $A(V_C - V_G)$ (Porosimeter Theory).

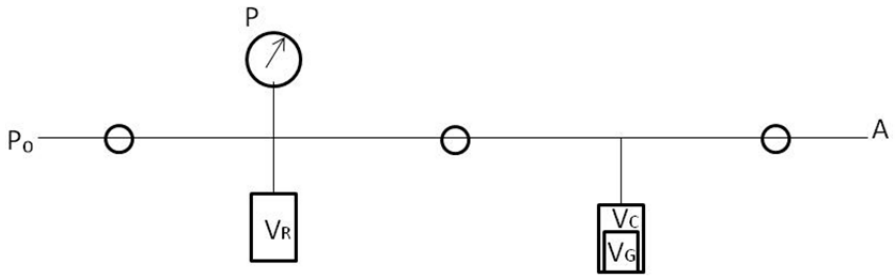

Figure A.4: Cobberly-Stevens porosimeter diagram. P_0 is the initial pressure in the reference cell when the valve is closed, P is the pressure after the valve is opened, A is the atmospheric pressure, V_R is the volume of the reference cell, V_C is the volume of the sample cell, and V_G is the grain volume (Porosimeter Theory).

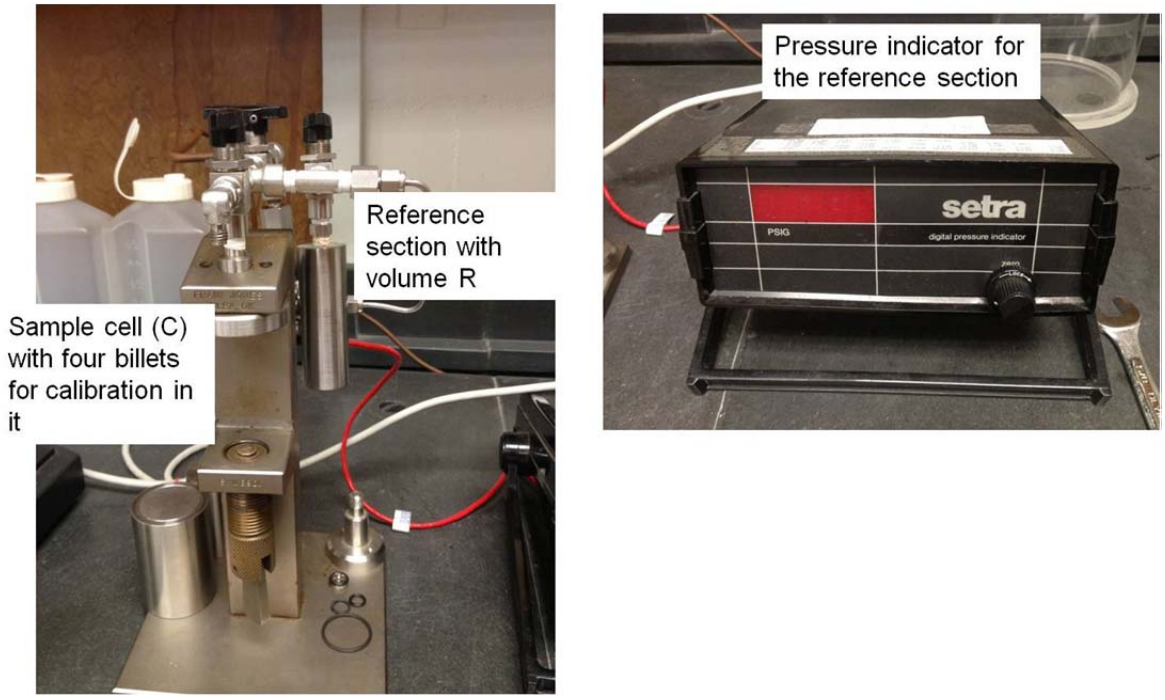

Figure A.5: Cobberly-Stevens porosimeter (left) and the pressure indicatoor for the reference section (right).

After valve that separates the two cells is opened, the gas starts flowing into the sample cell until it reaches equilibrium. The equilibrium gauge pressure, P, is displayed on the pressure indicator. The combined pressure - volume in both cells is now equal to $(P + A)(V_R + V_C - V_G)$. Since the product of pressure and volume is constant, the sum of pressure - volume products in the beginning of the experiment is equal to the pressure - volume product after the valve is opened, or

$$A(V_C - V_G) + V_R(P_0 + A) = (P + A)(V_R + V_C - V_G) \quad \text{(A.1).}$$

The grain volume is then can be written as

$$V_G = V_R + V_C - V_R(P_0/P) \quad \text{(A.2).}$$

In order to find the term V_R, the instrument is calibrated by using the set of billets of known volume. First, the measurement with all the billets in the sample cell is taken, and the equation (2) for this system is

$$B_1 + B_2 + B_3 + B_4 = V_R + V_C - V_R\left(P_{0f}/P_f\right) \quad \text{(A.3),}$$

where B_1, B_2, B_3, and B_4 are the volumes of the billets, P_{0f} is the initial gauge pressure, and P_f is the final gauge pressure with all of the billets present. Then, one of the billets, B_2, is removed, and the equation becomes

$$B_1 + B_3 + B_4 = V_R + V_C - V_R(P_{0b}/P_b) \quad \text{(A.4),}$$

where $P_{0b}$is the initial gauge pressure and P_b is the final gauge pressure with B_2 removed.

By subtracting (4) from (3), the following equations are obtained

$$B_2 = V_R(P_{0b}/P_b - P_{0f}/P_f) \quad \text{(A.5),}$$

and

$$V_R = B_2/(P_{0b}/P_b - P_{0f}/P_f) \quad \text{(A.6)}$$

(Porosimeter Theory).

After calibration is performed, some of the billets are removed from the sample cell to be replaced by the core sample. For example, if the first three billets are removed, then the equation (2) takes a form

$$V_G + B_4 = V_R + V_C - V_R(P_{0s}/P_s) \quad \text{(A.7)},$$

where P_{0s} is the initial gauge volume reading, and P_s is the final gauge volume reading. V_G is obtained by subtracting (7) from (3), so that

$$V_G = B_1 + B_2 + B_3 + V_R(P_{0f}/P_f - P_{0s}/P_s) \quad \text{(A.8)}.$$

Porosity is then can be determined from the equation below:

$$\phi = \frac{V_G - V_b}{V_b} \quad \text{(A.9)},$$

where V_b is the bulk volume of the sample (Porosimeter Theory).

A.3 Permeability Measurements

Gas permeability method with Ni gas using Core Petrophysical software and equipment was applied to the samples for measuring permeability. Permeability determination with gas flow method uses Darcy's law that is valid for the laminar flow. Therefore, the laminar flow condition needs to be maintained during the experiment. The flow equation is shown below:

$$Q = \frac{k*A*(P_1 - P_2)}{\mu*L} \quad \text{(10)},$$

where Q is the flow rate, k is the permeability, A is the surface area, P_1 and P_2 are initial and final pressures, respectively, μ is the viscosity, and L is the length of the sample (Figure A.6).

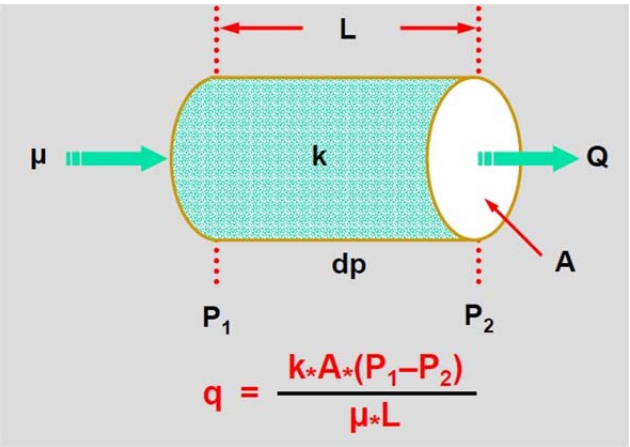

Figure A.6: An illustration of the laminar flow through the sample. Q is the flow rate, k is the permeability, A is the surface area, $P_1 - P_2$ is the pressure difference, μ is the viscosity, and L is the length of the sample (Crain's Petrophysical Handbook).

B. APPENDIX: PICTURES OF VELOCITY MEASUREMENT STATIONS

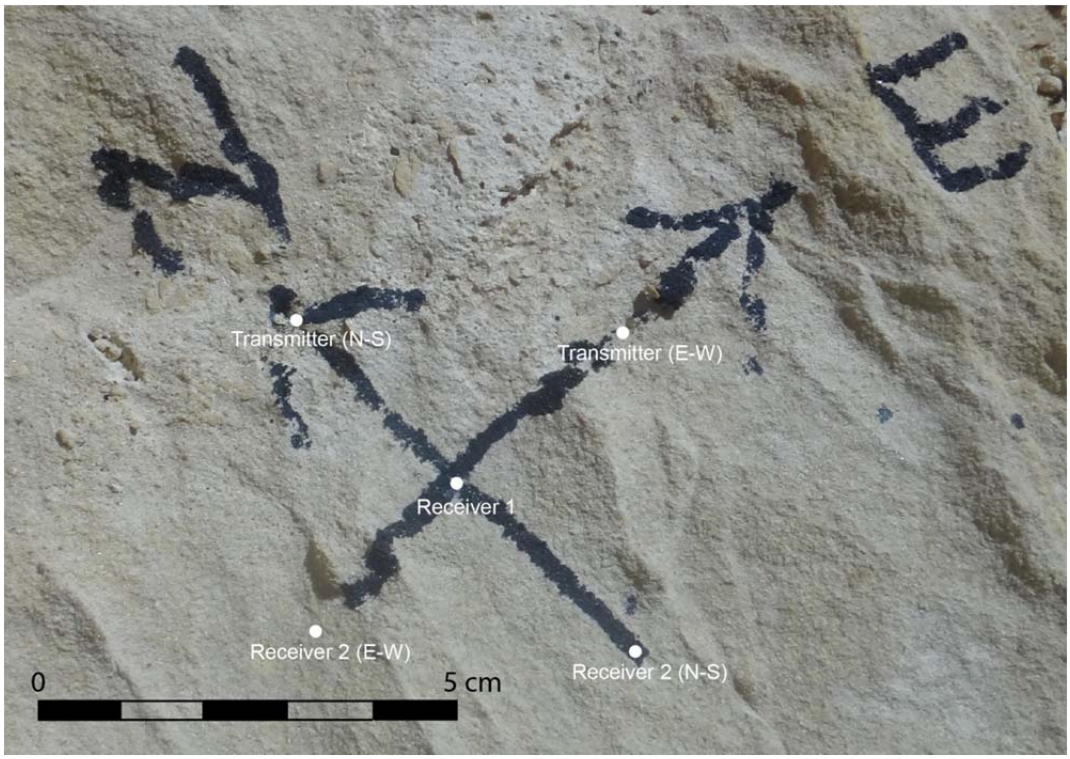

Figure B.1: Traverse 1, Station 1, Measurement 1.

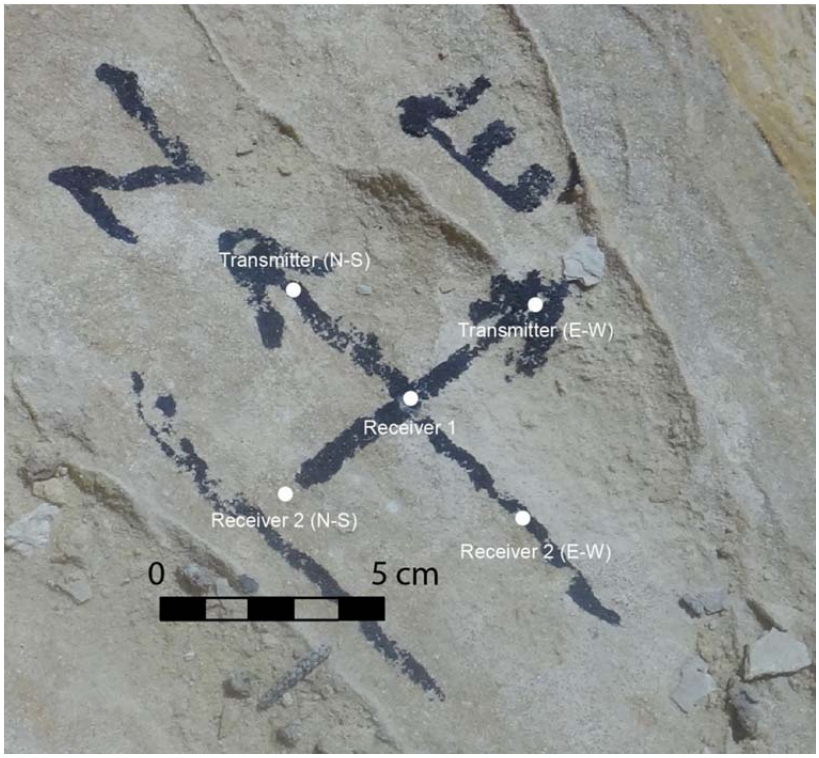

Figure B.2: Traverse 1, Station 1, Measurement 2.

Figure B.3: Traverse 1, Station 2, Measurement 1.

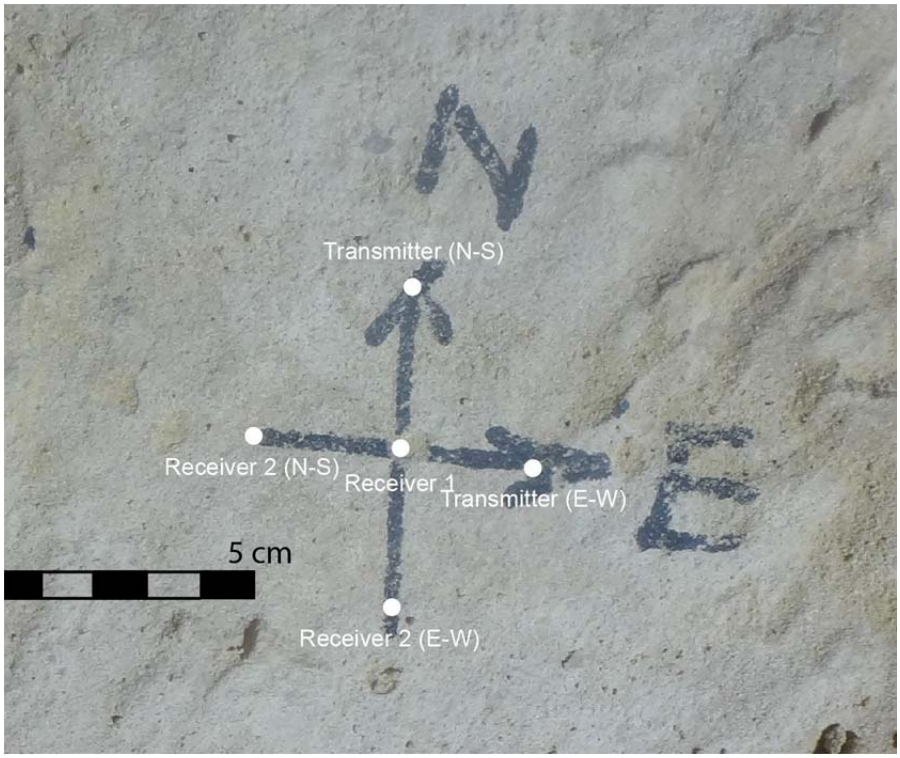

Figure B.4: Traverse 1, Station 2, Measurement 2.

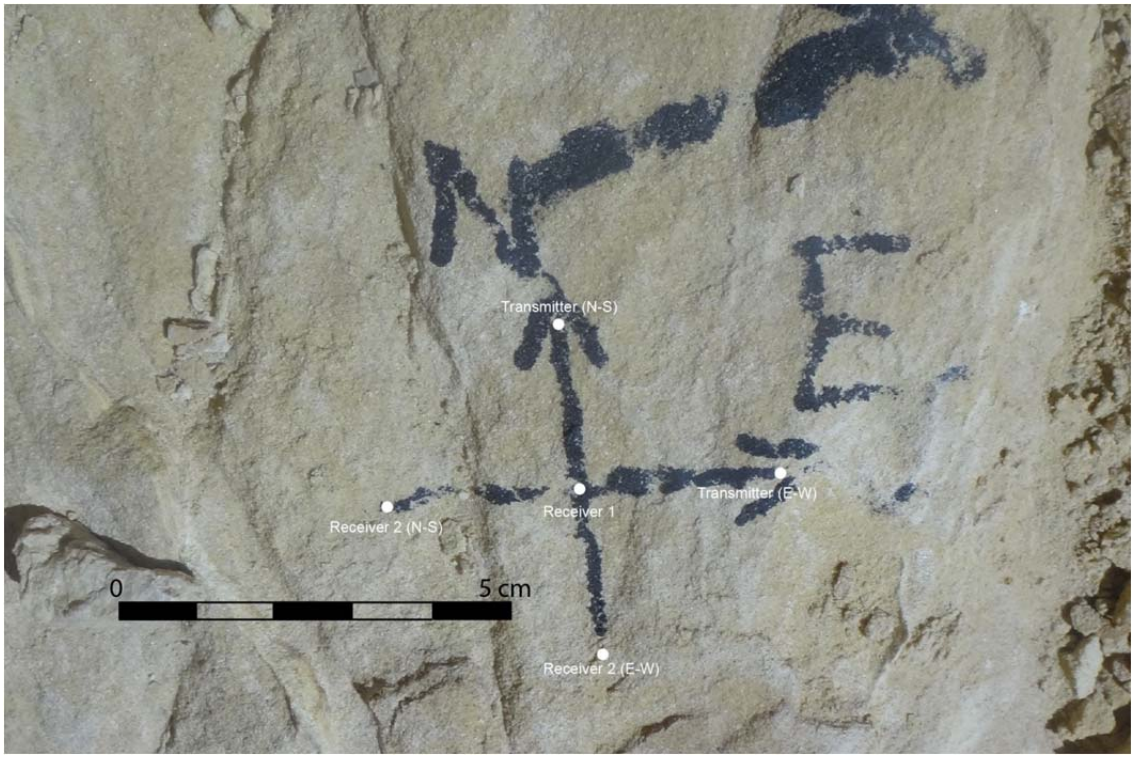

Figure B.5: Traverse 1, Station 3, Measurement 1.

Figure B.6: Traverse 1, Station 3, Measurement 2.

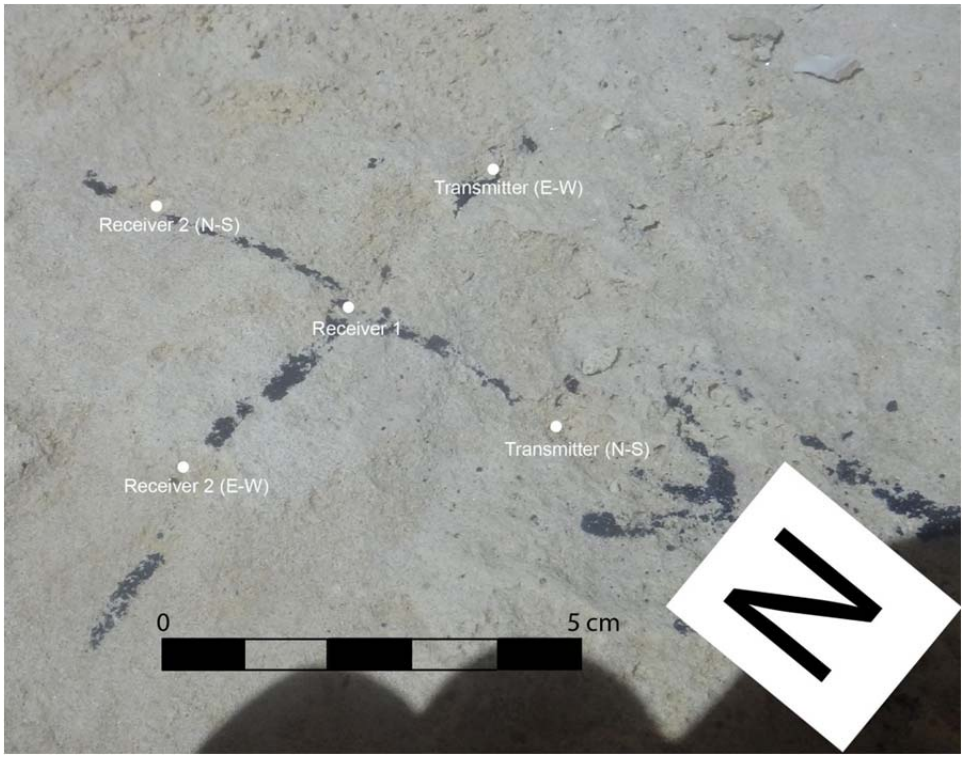

Figure B.7: Traverse 2, Station 1, Measurement 1.

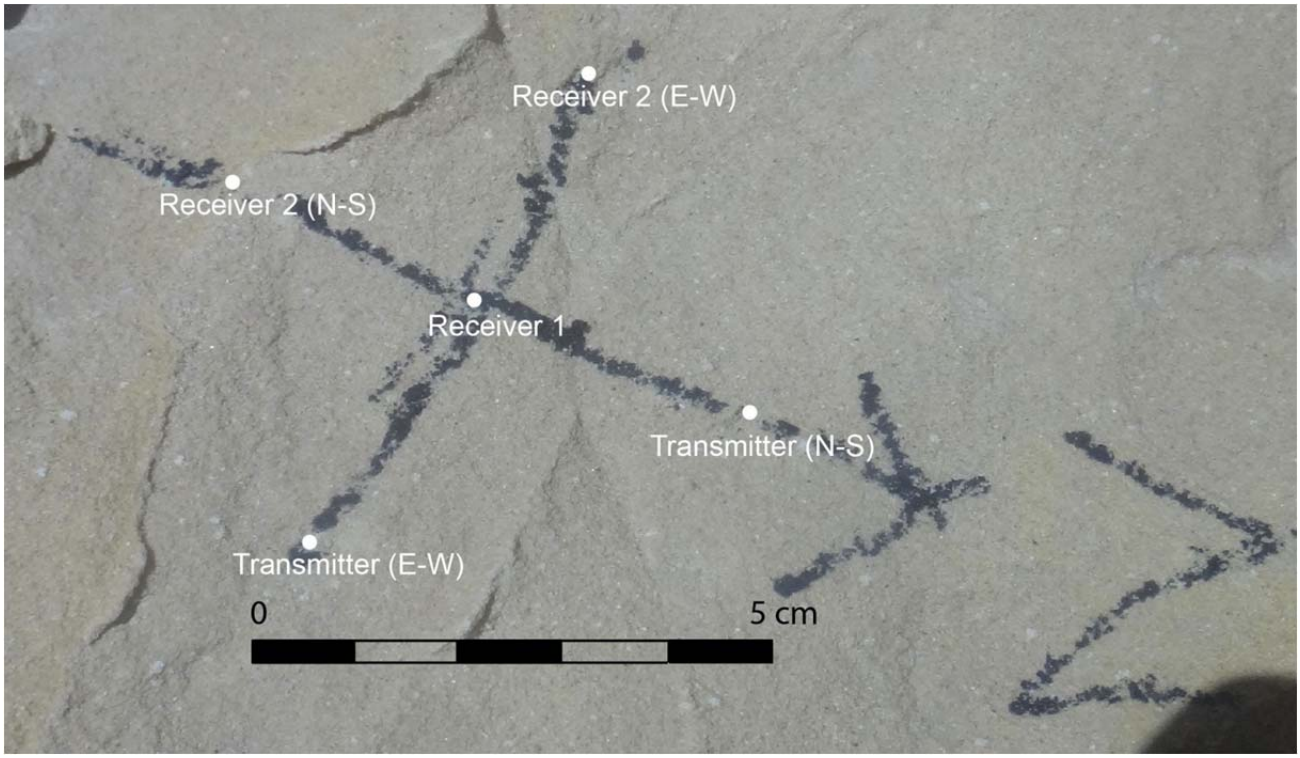

.

Figure B.8: Traverse 2, Station 1, Measurement 2.

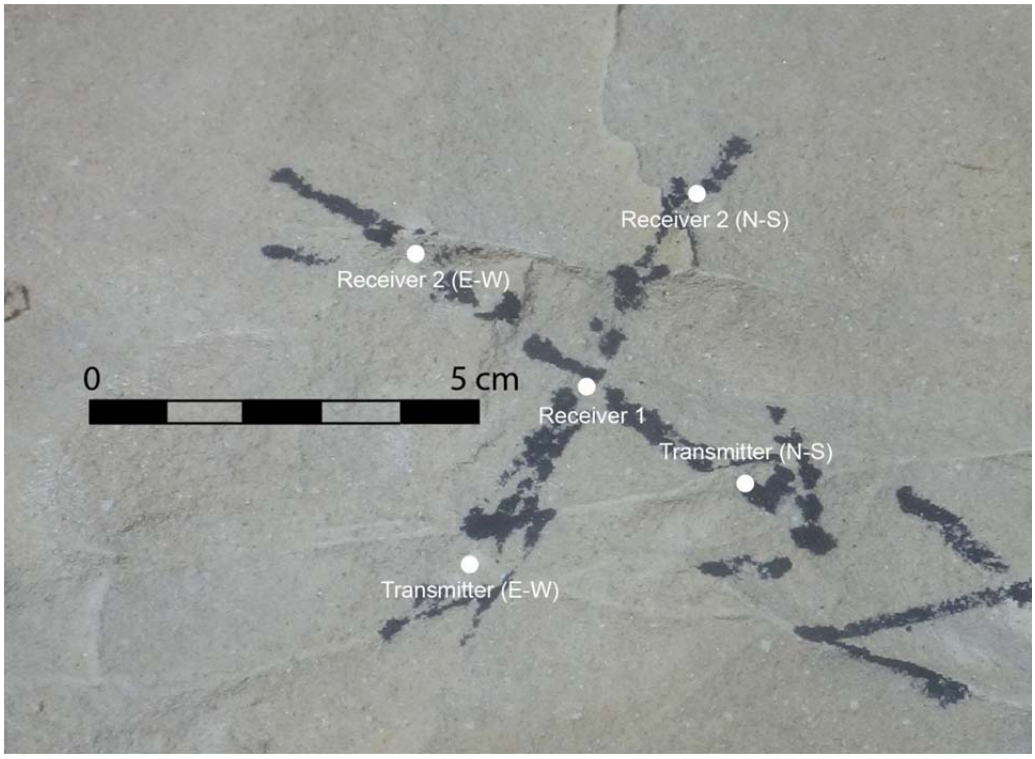

Figure B.9: Traverse 2, Station 2, Measurement 1.

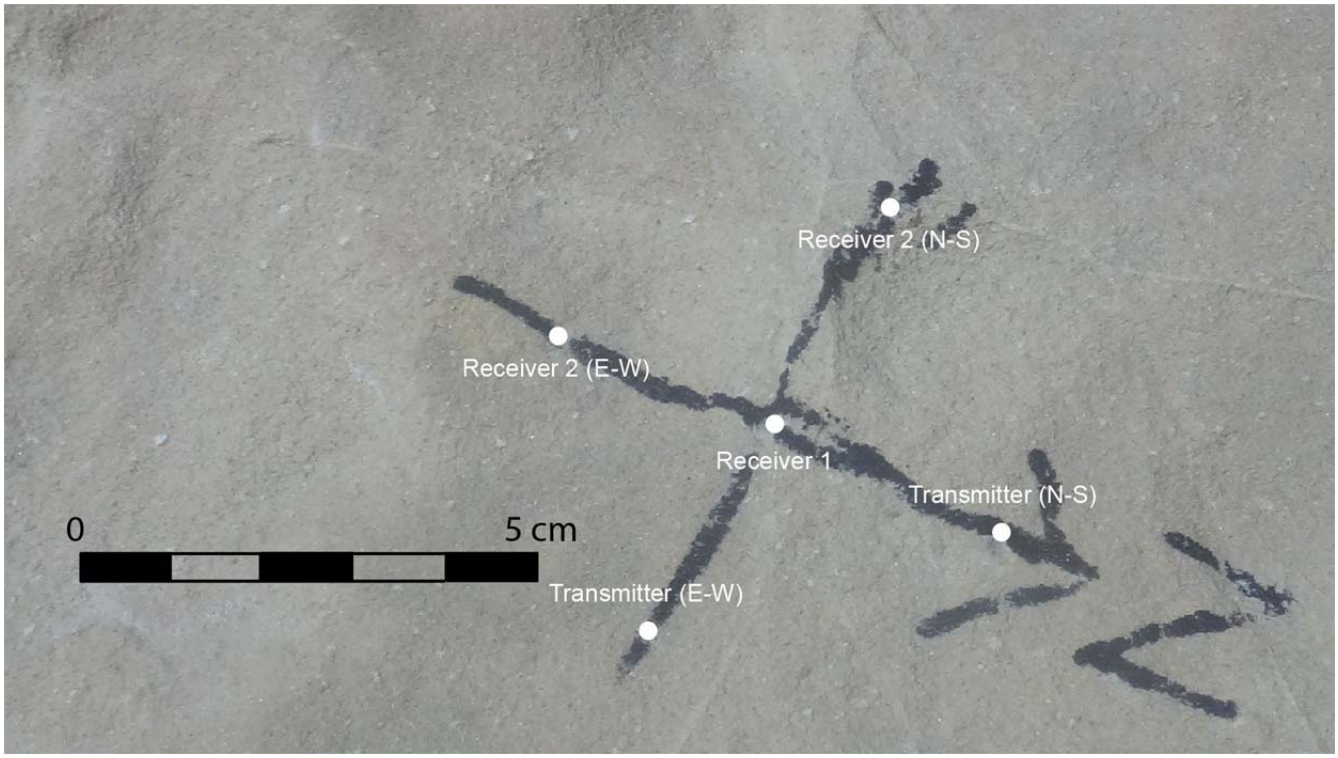

Figure B.10: Traverse 2, Station 2, Measurement 2.

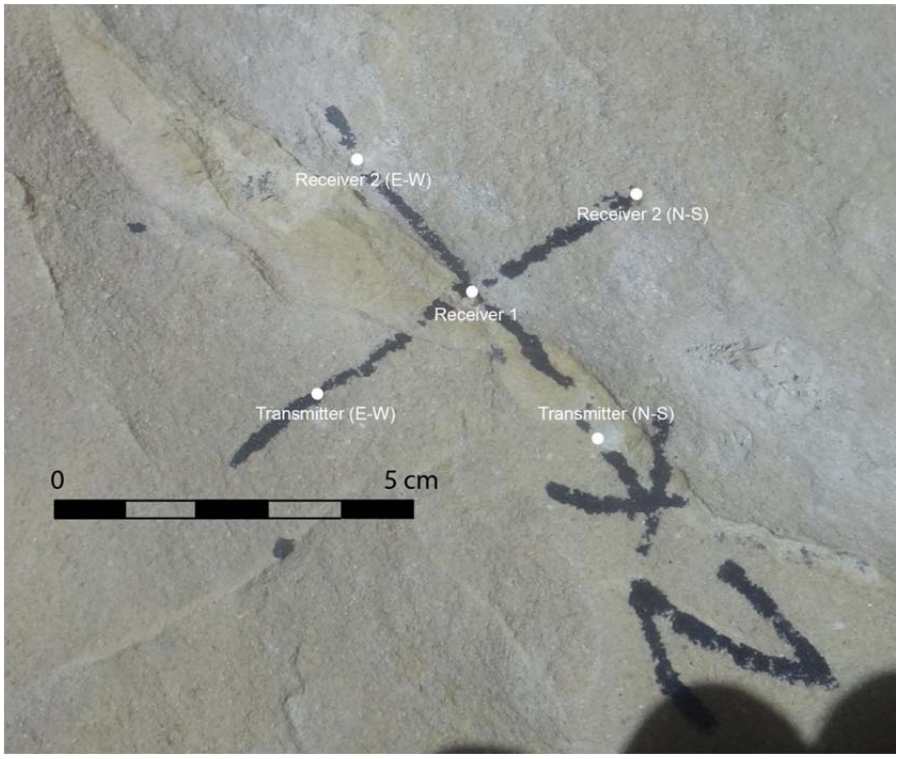

Figure B.11: Traverse 2, Station 3, Measurement 1.

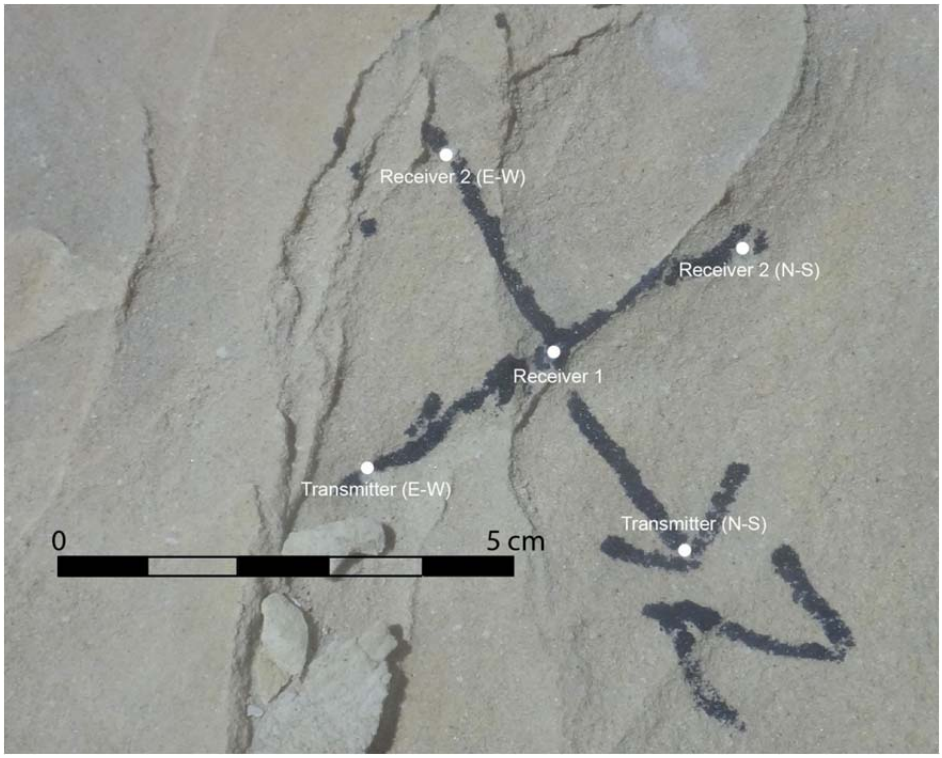

Figure B.12: Traverse 2, Station 3, Measurement 2.

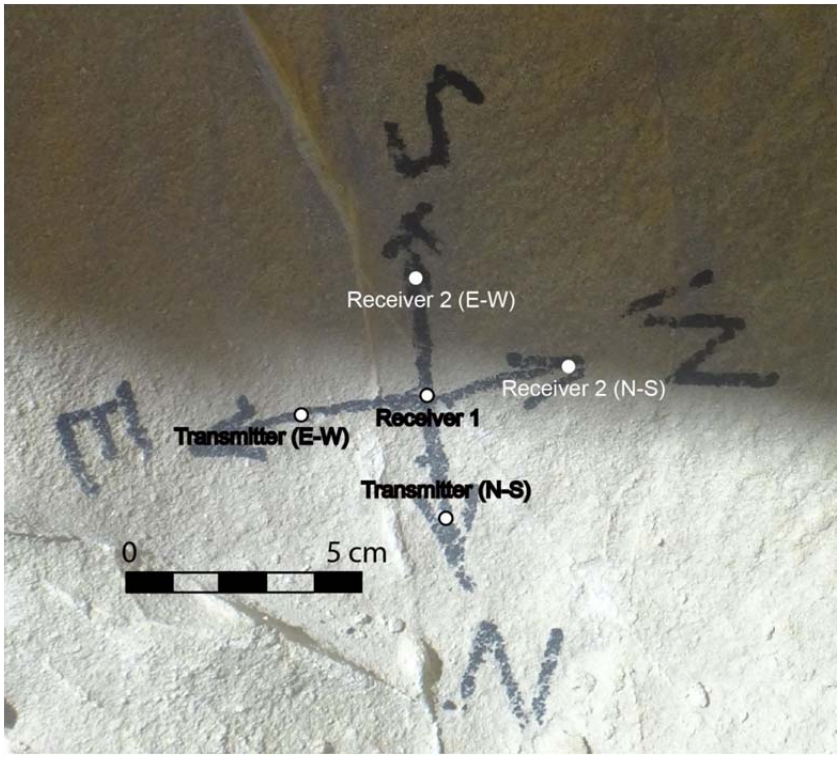

Figure B.13: Traverse 3, Station 1, Measurement 1.

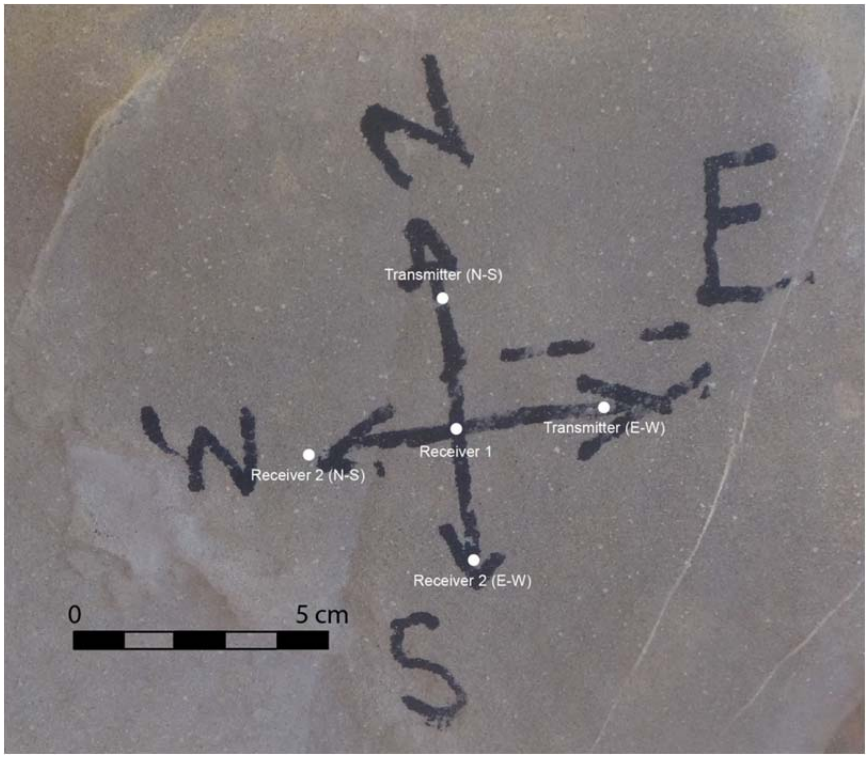

Figure B.14: Traverse 3, Station 1, Measurement 2.

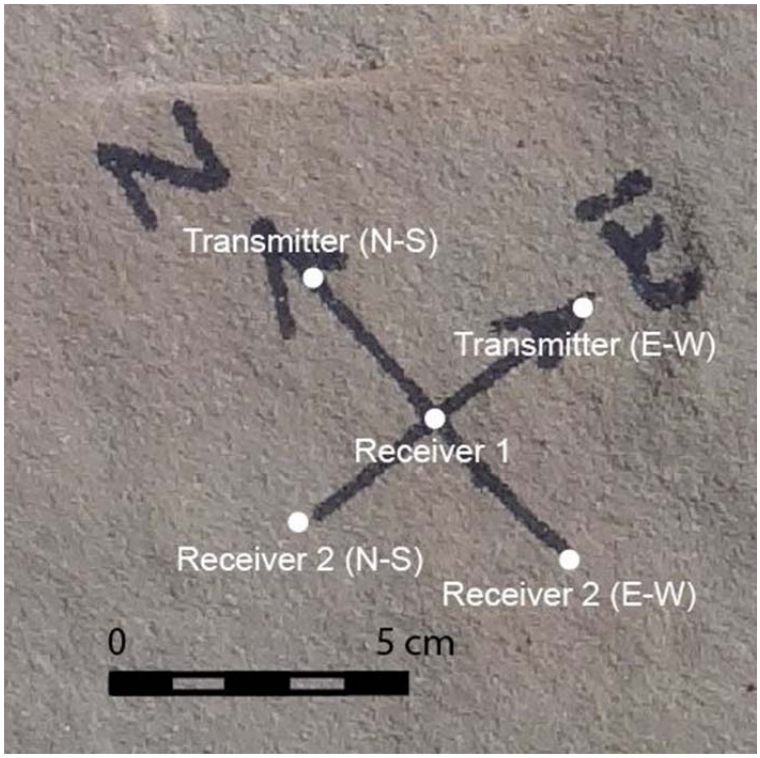

Figure B.15: Traverse 4, Station 1, Measurement 1.

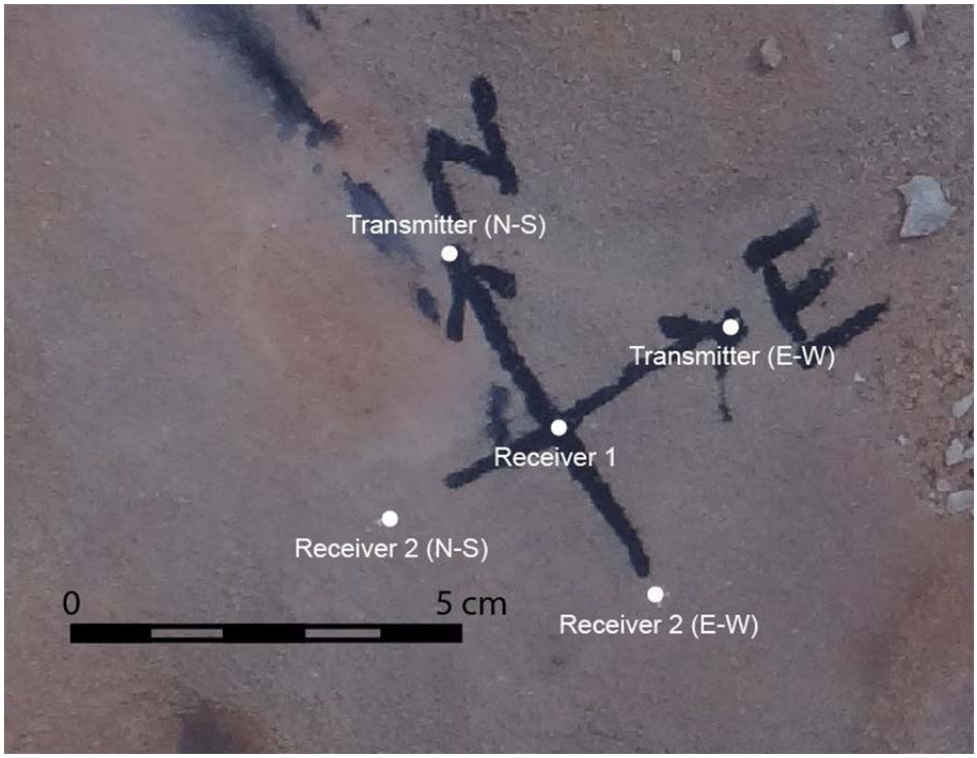

Figure B.16: Traverse 4, Station 1, Measurement 2.

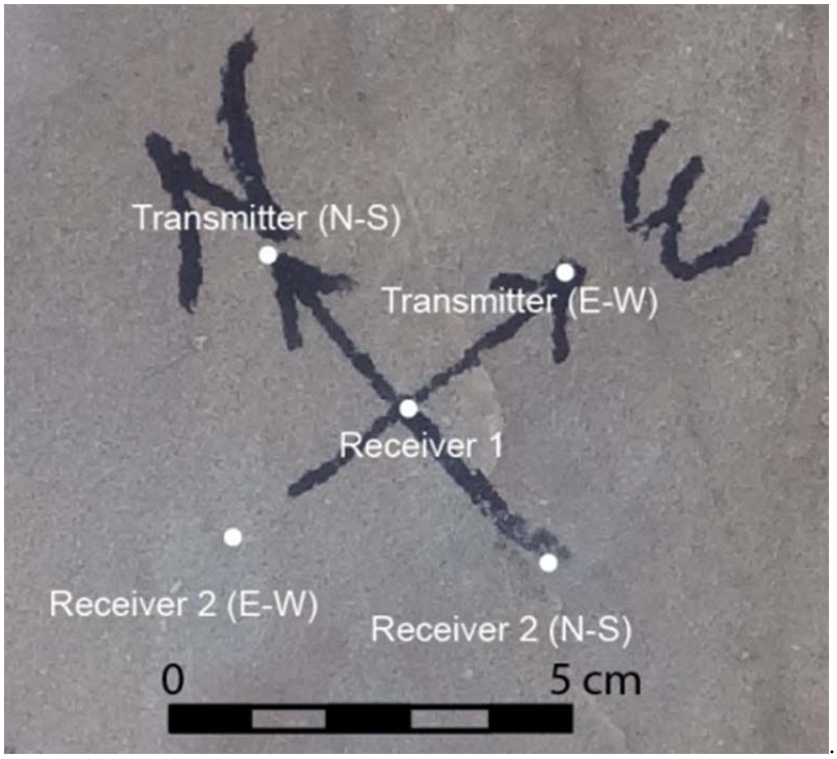

Figure B.17: Traverse 4, Station 2, Measurement 1.

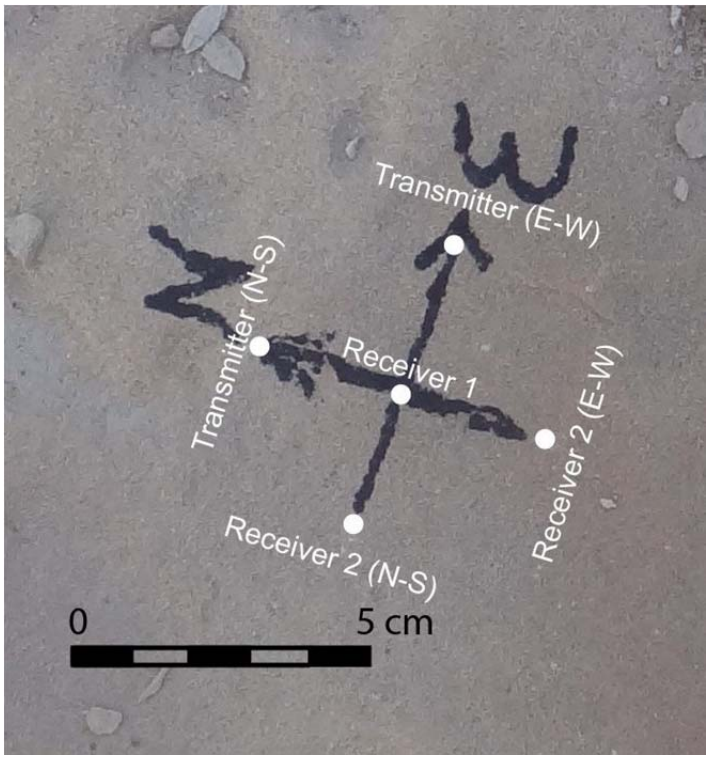

Figure B.18: Traverse 4, Station 2, Measurement 2.

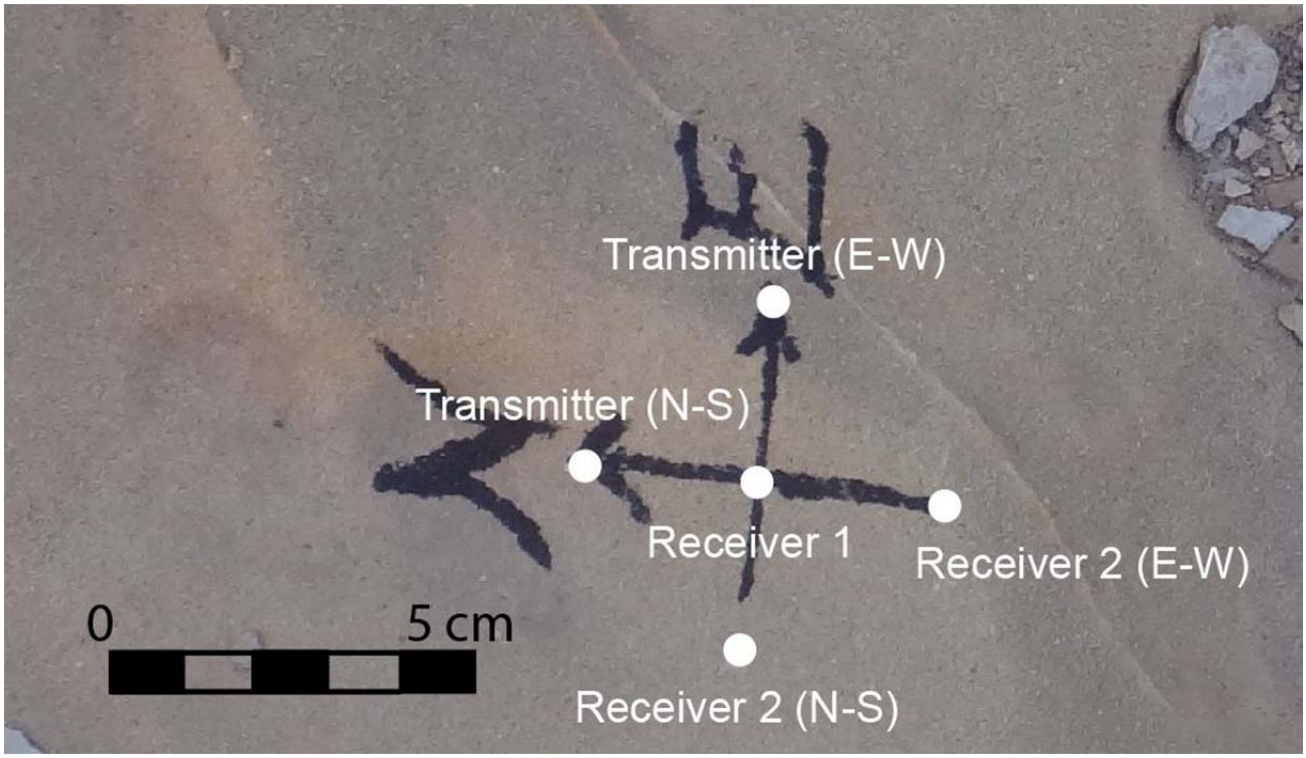

Figure B.19: Traverse 4, Station 3, Measurement 1.

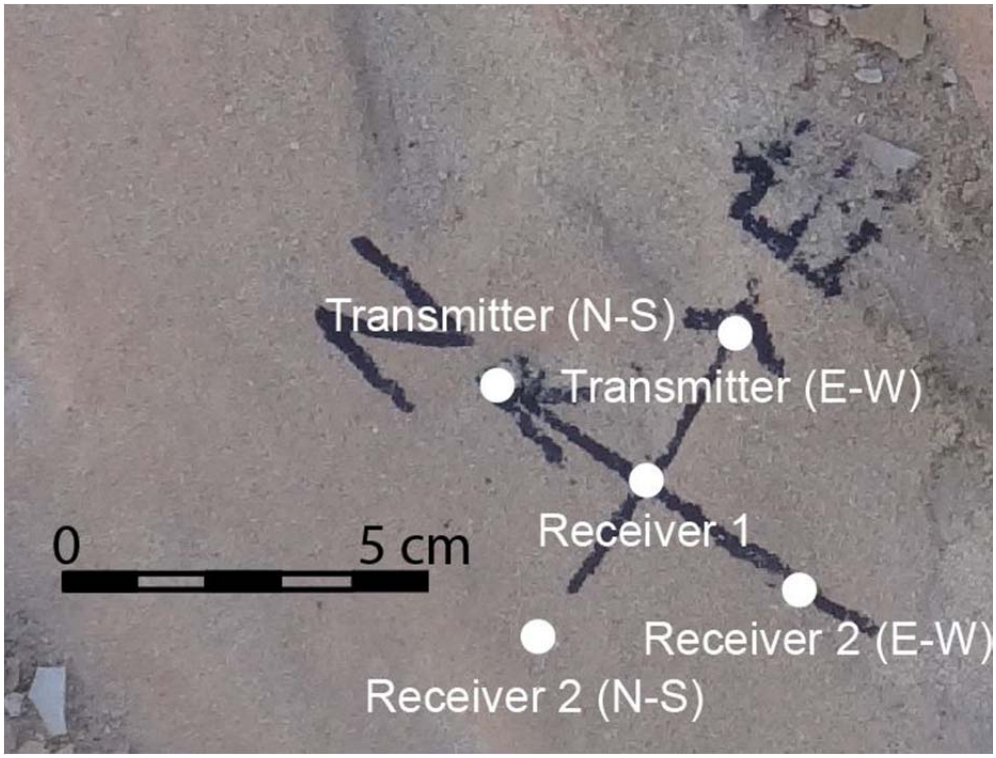

Figure B.20: Traverse 4, Station 3, Measurement 2.

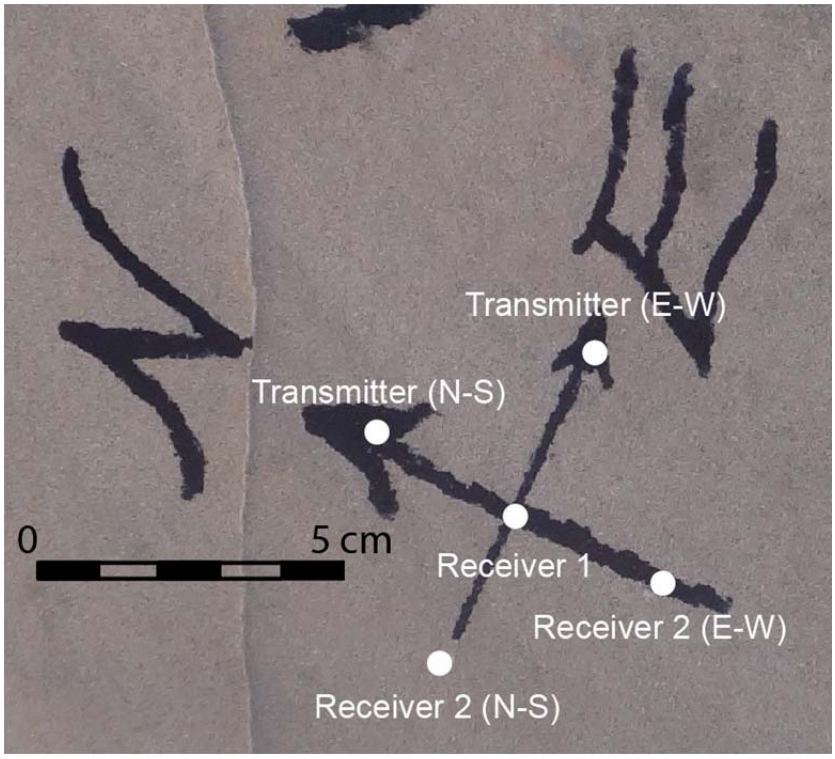

Figure B.21: Traverse 4, Station 4, Measurement 1.

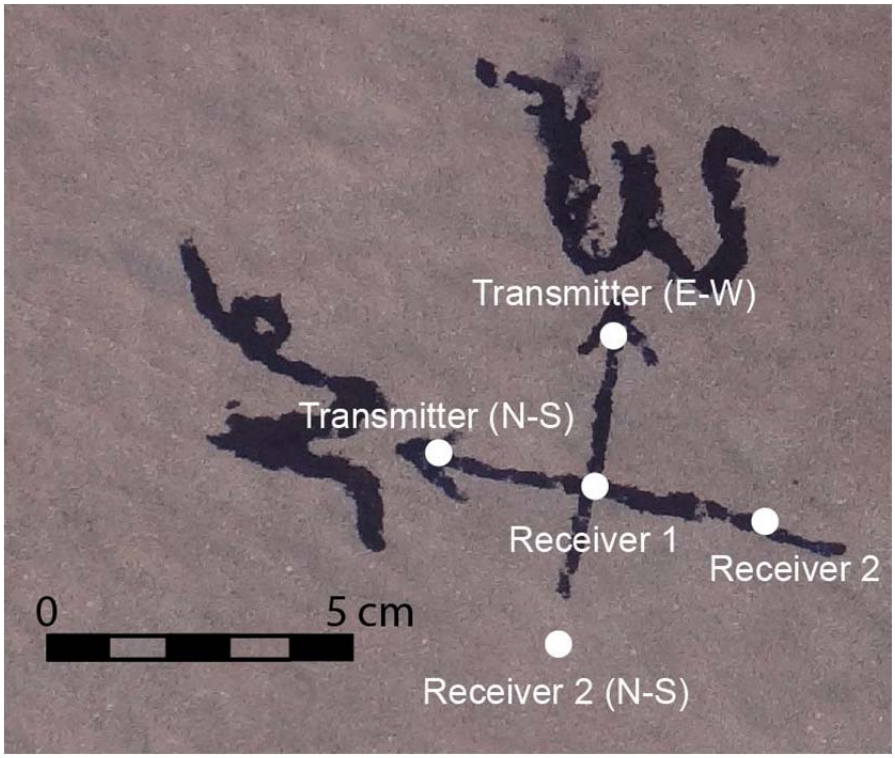

Figure B.22: Traverse 4, Station 4, Measurement 2.

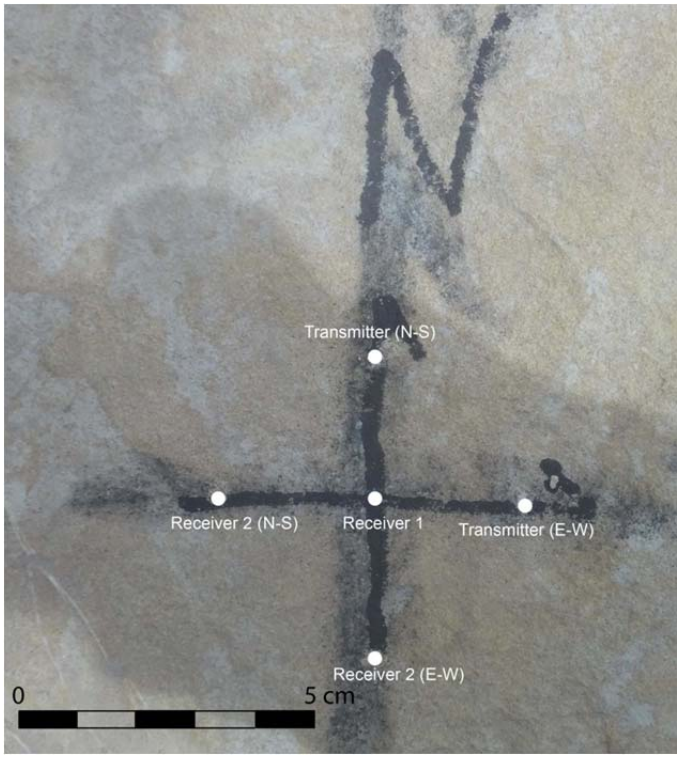

Figure B.23: Traverse 5, Station 1, Measurement 1.

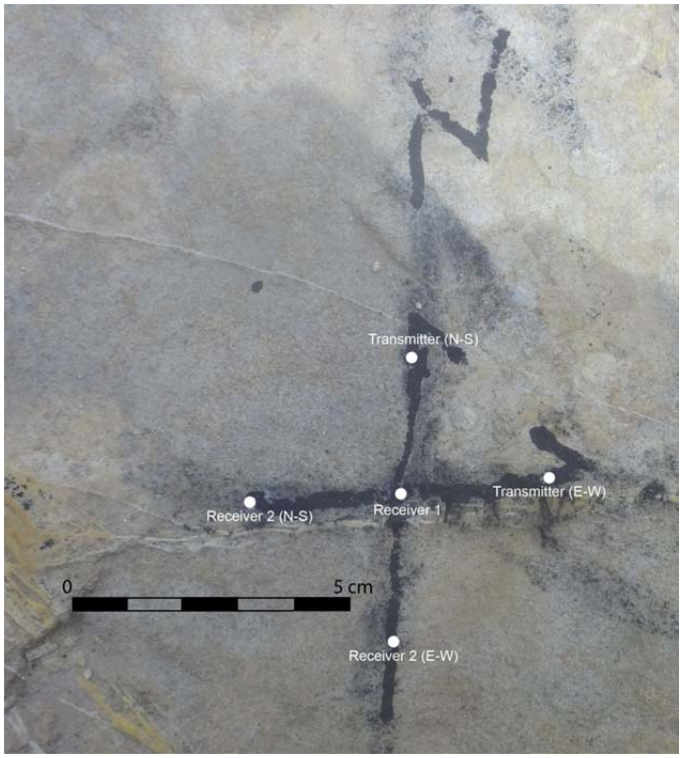

Figure B.24: Traverse 5, Station 1, Measurement 2.

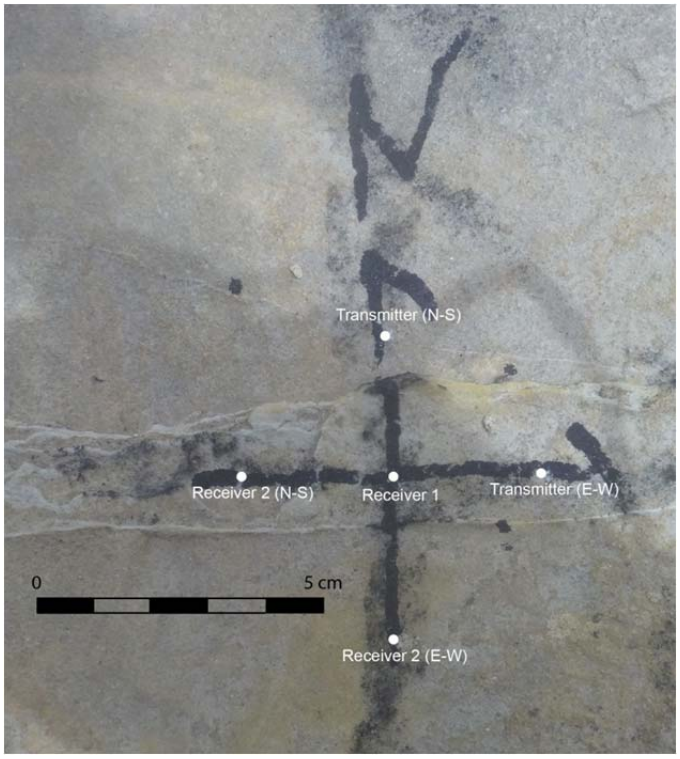

Figure B.25: Traverse 5, Station 2, Measurement 1.

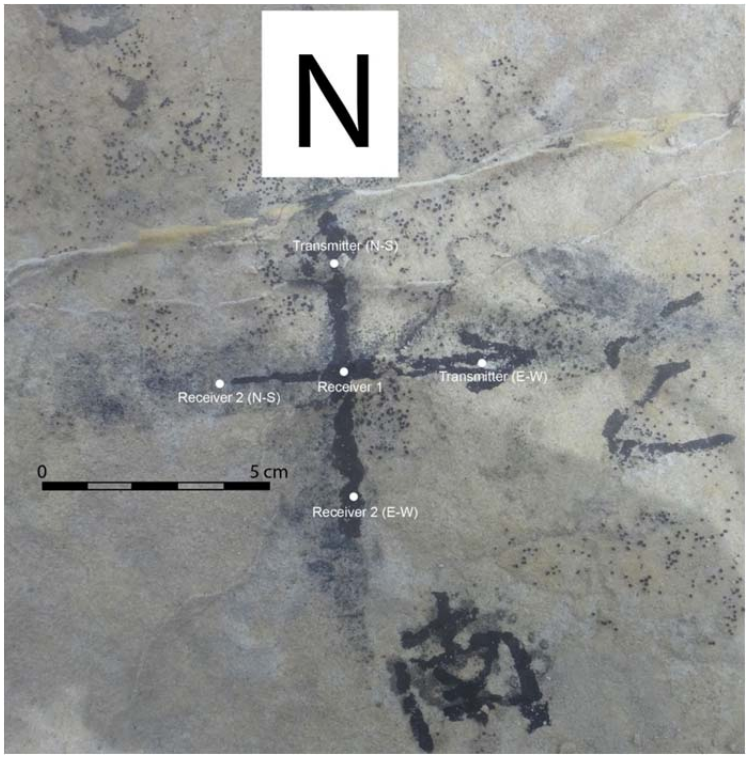

Figure B.26: Traverse 5, Station 2, Measurement 2.

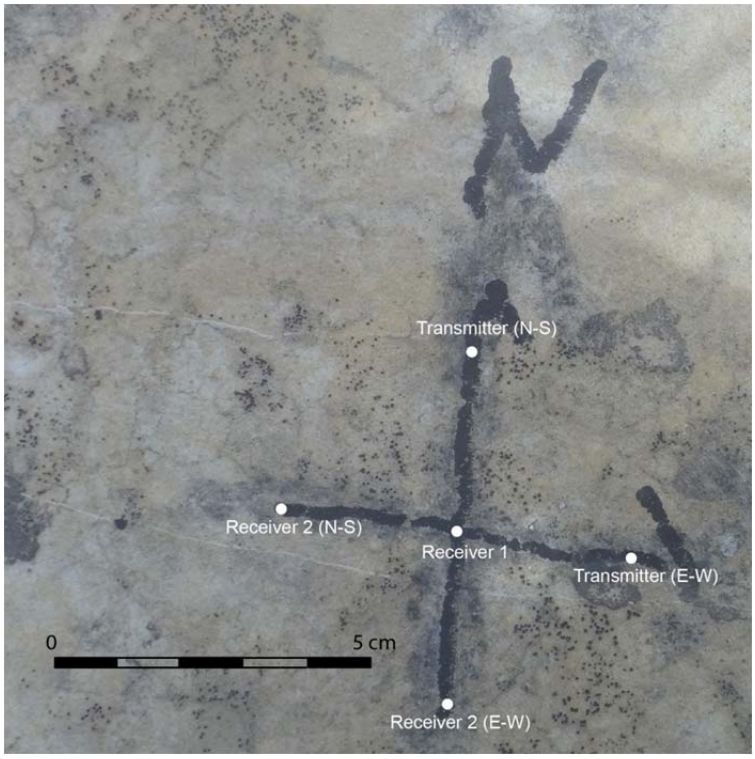

Figure B.27: Traverse 5, Station 3, Measurement 1.

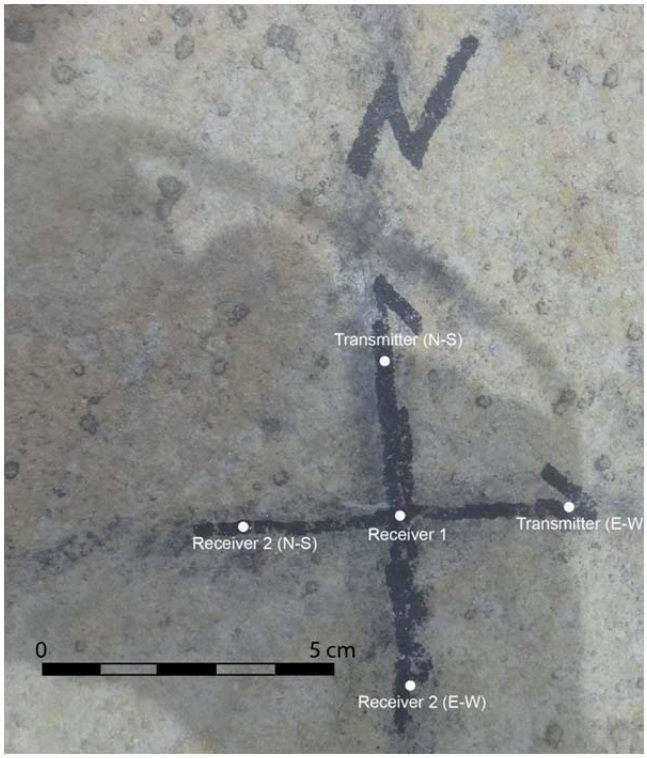

Figure B.28: Traverse 5, Station 3, Measurement 2.

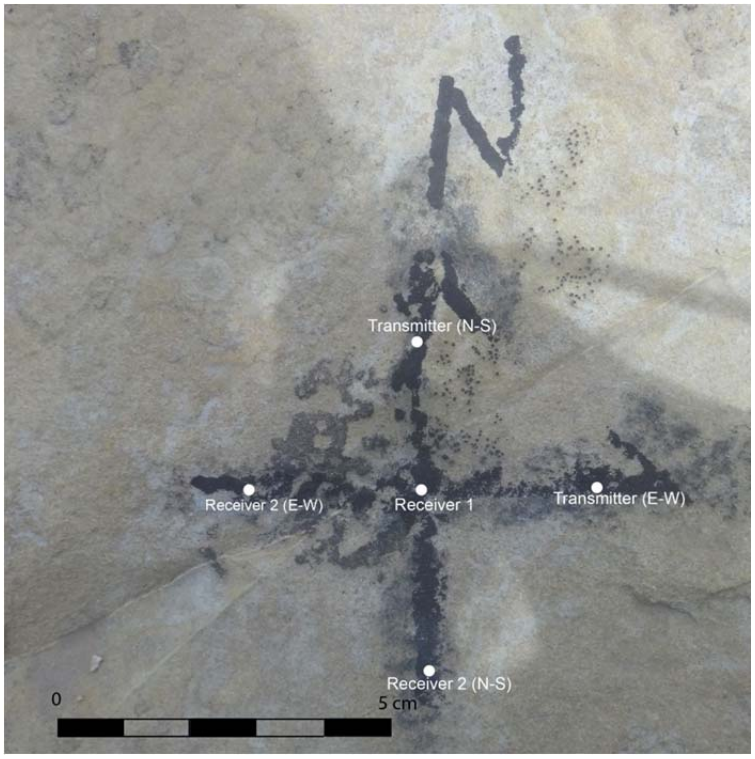

Figure B.29: Traverse 5, Station 4, Measurement 1.

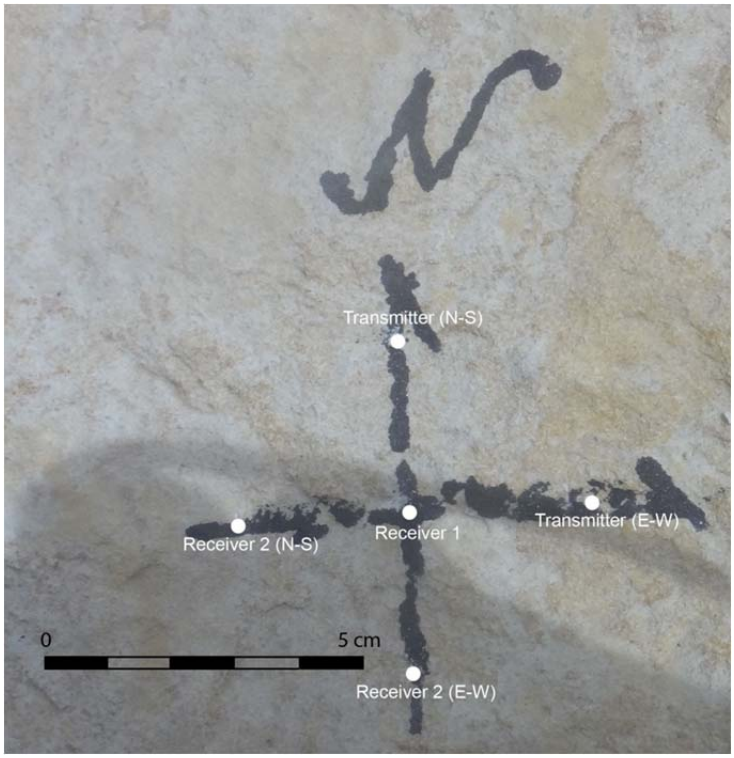

Figure B.30: Traverse 5, Station 4, Measurement 2.

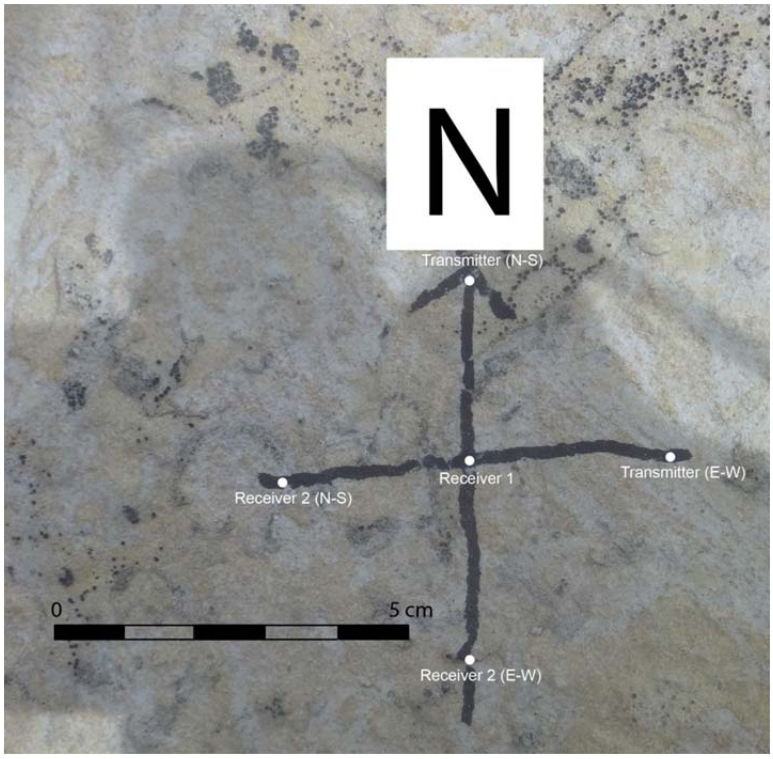

Figure B.31: Traverse 5, Station 5, Measurement 1.

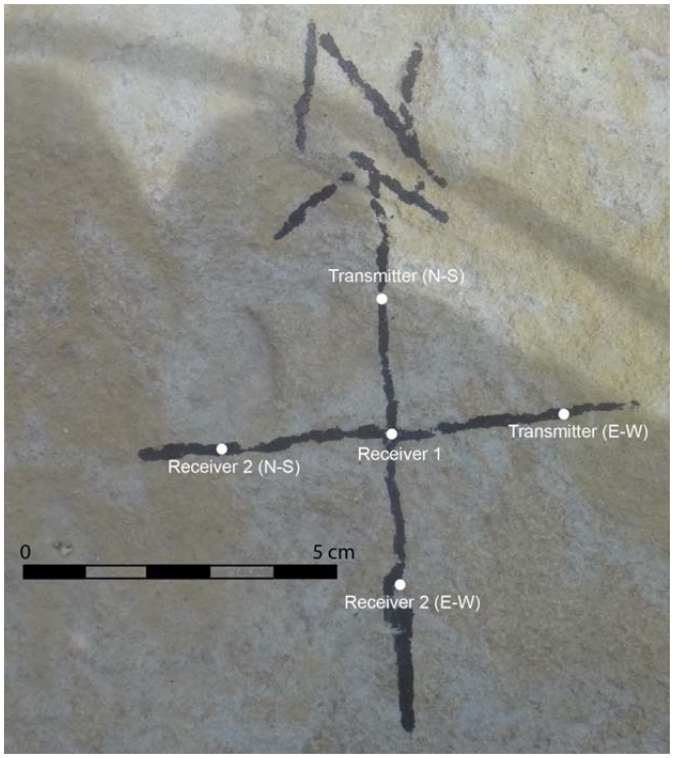

Figure B.32: Traverse 5, Station 5, Measurement 2.

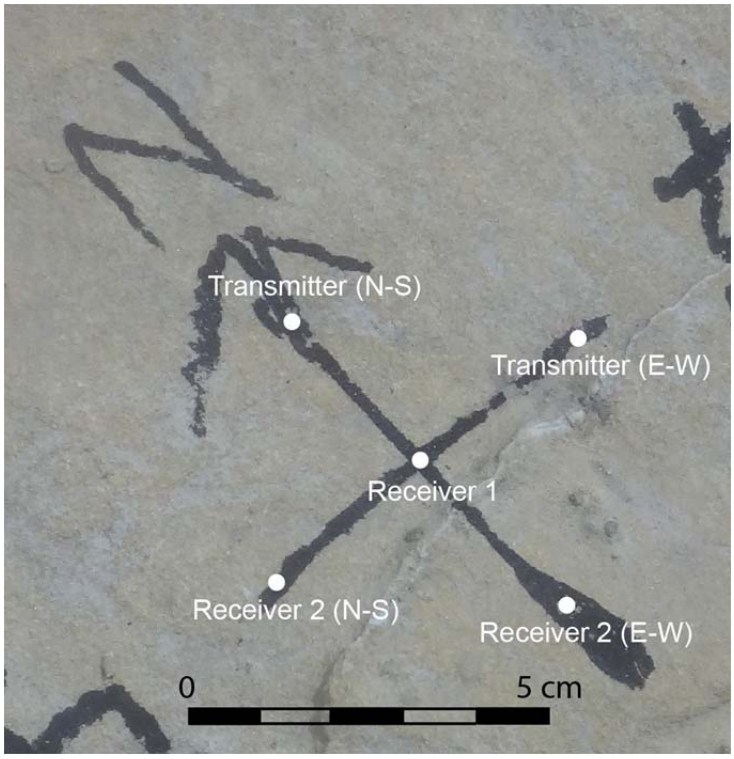

Figure B.33: Traverse 5, Station 6, Measurement 1.

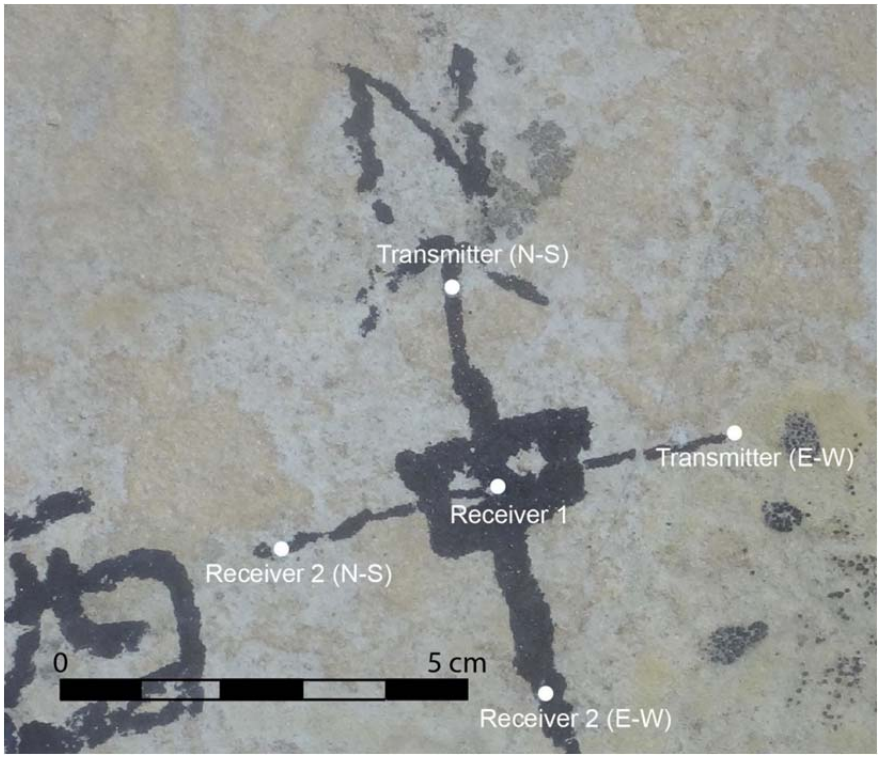

Figure B.34: Traverse 5, Station 6, Measurement 2.

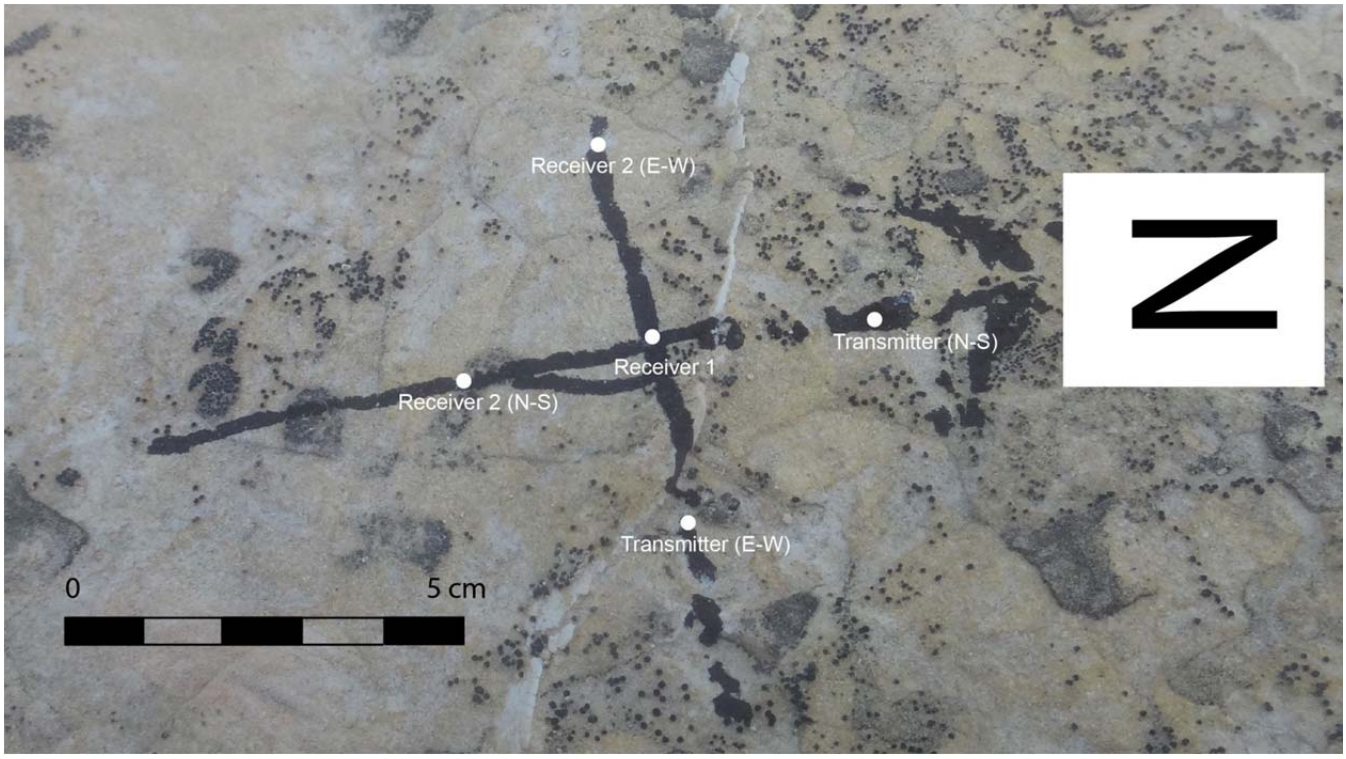

Figure B.35: Traverse 5, Station 7, Measurement 1.

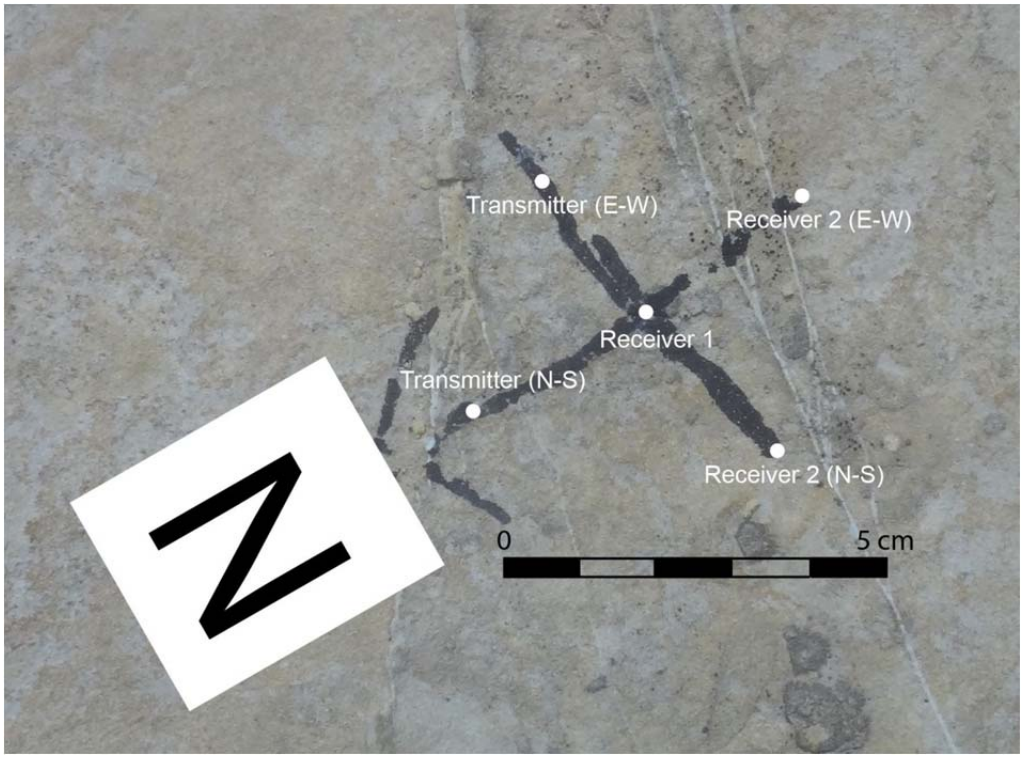

Figure B.36: Traverse 5, Station 7, Measurement 2.

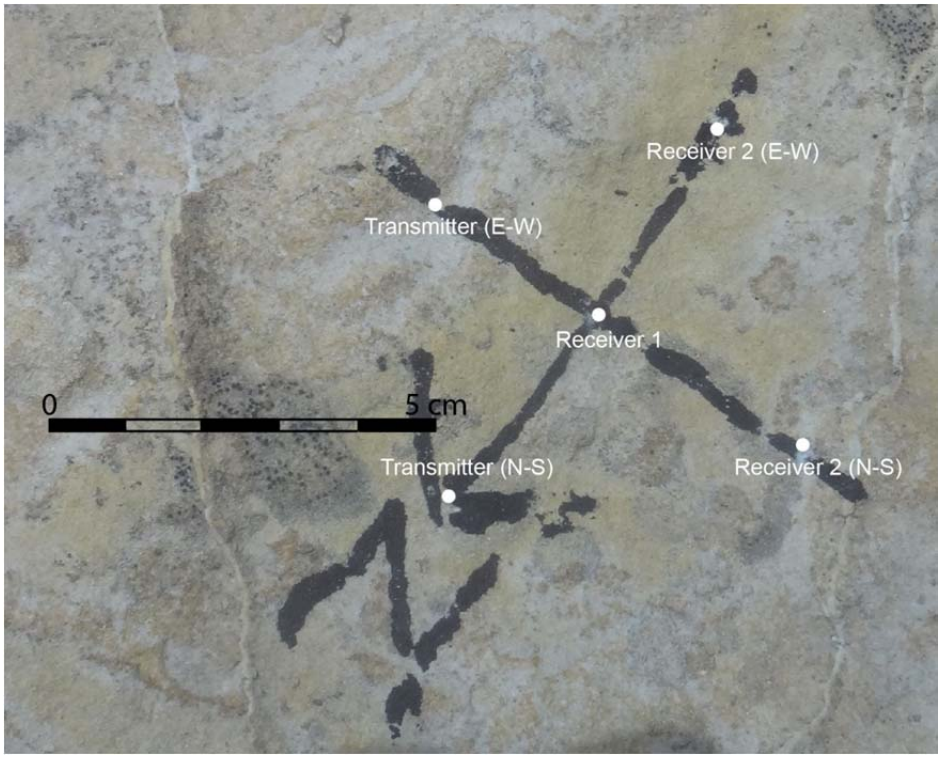

Figure B.37: Traverse 5, Station 8, Measurement 1.

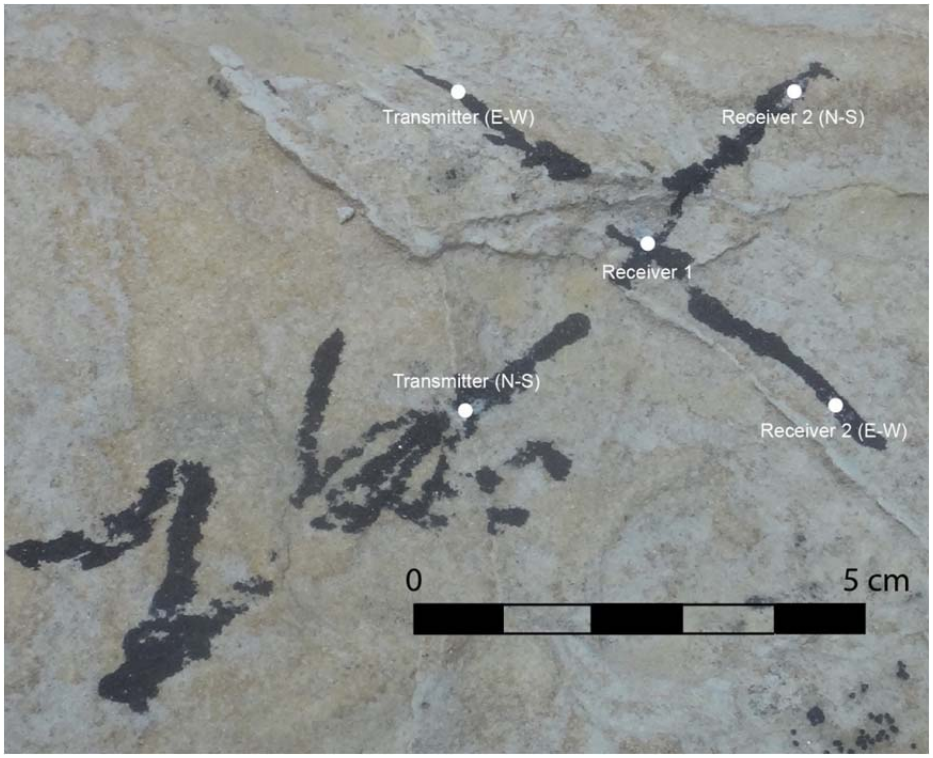

Figure B.38: Traverse 5, Station 8, Measurement 2.

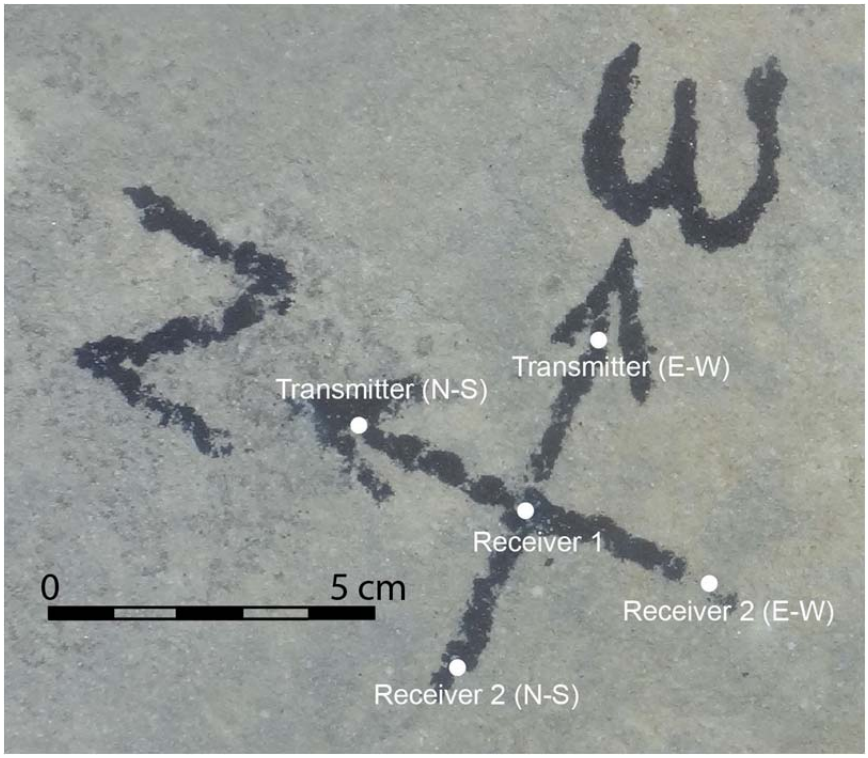

Figure B.39: Traverse 6, Station 1, Measurement 1.

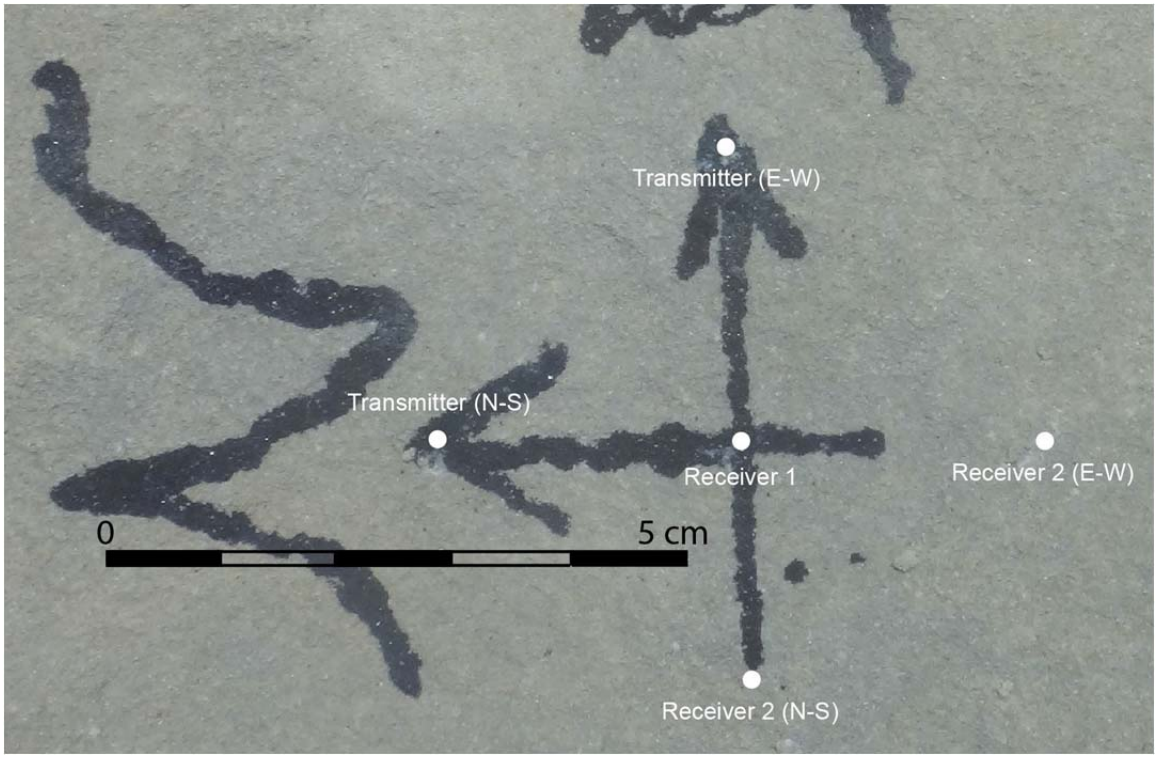

Figure B.40: Traverse 6, Station 1, Measurement 2.

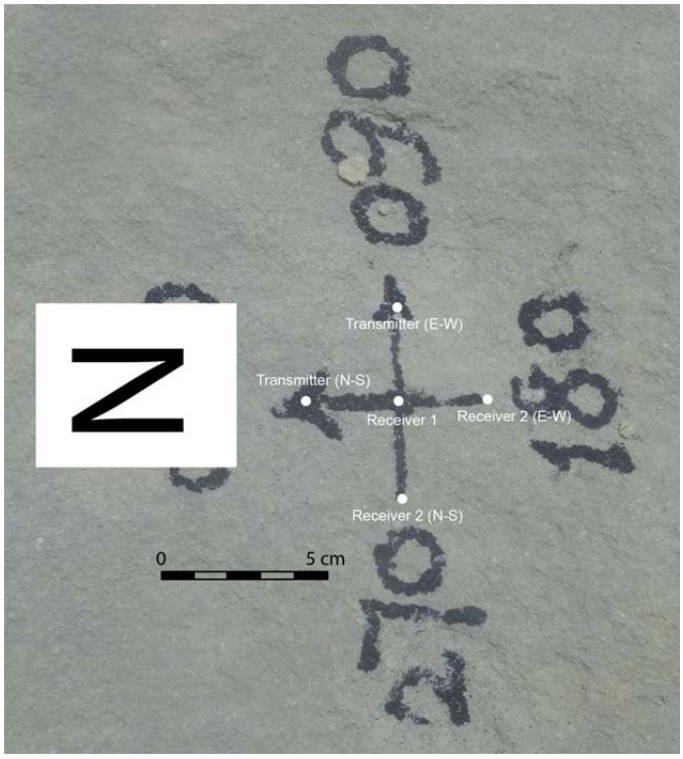

Figure B.41: Traverse 6, Station 2, Measurement 1.

Figure B.42: Traverse 6, Station 2, Measurement 2.

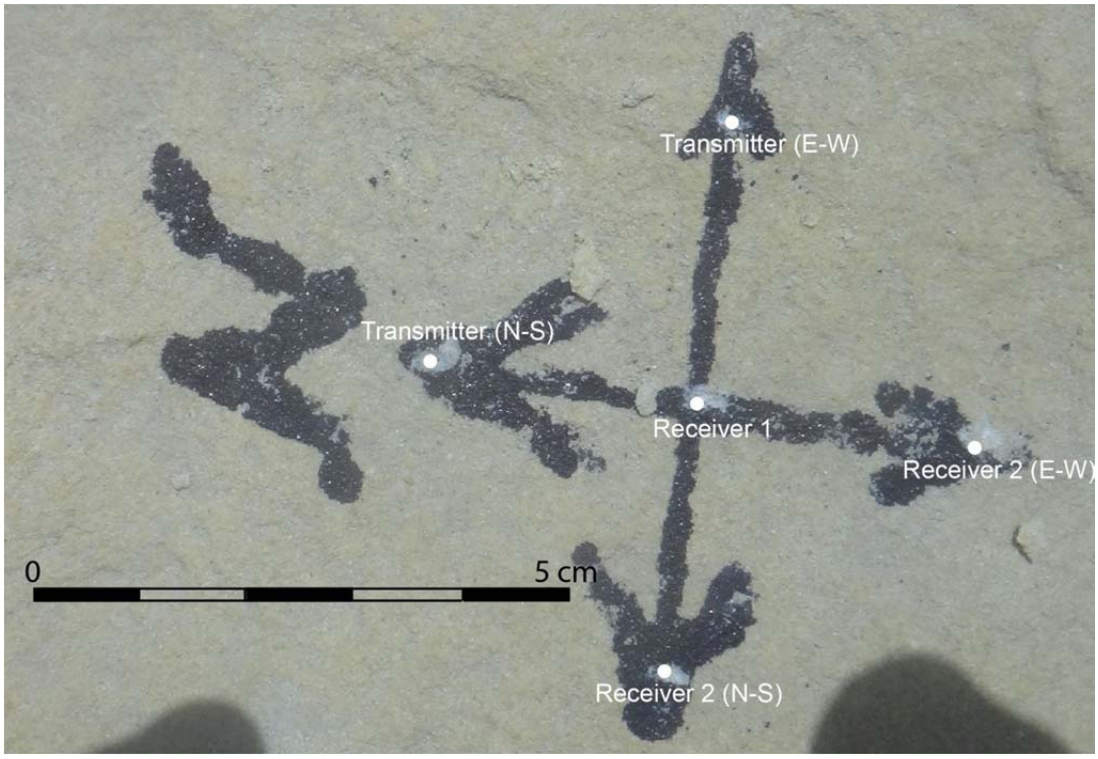

Figure B.43: Traverse 6, Station 3, Measurement 1.

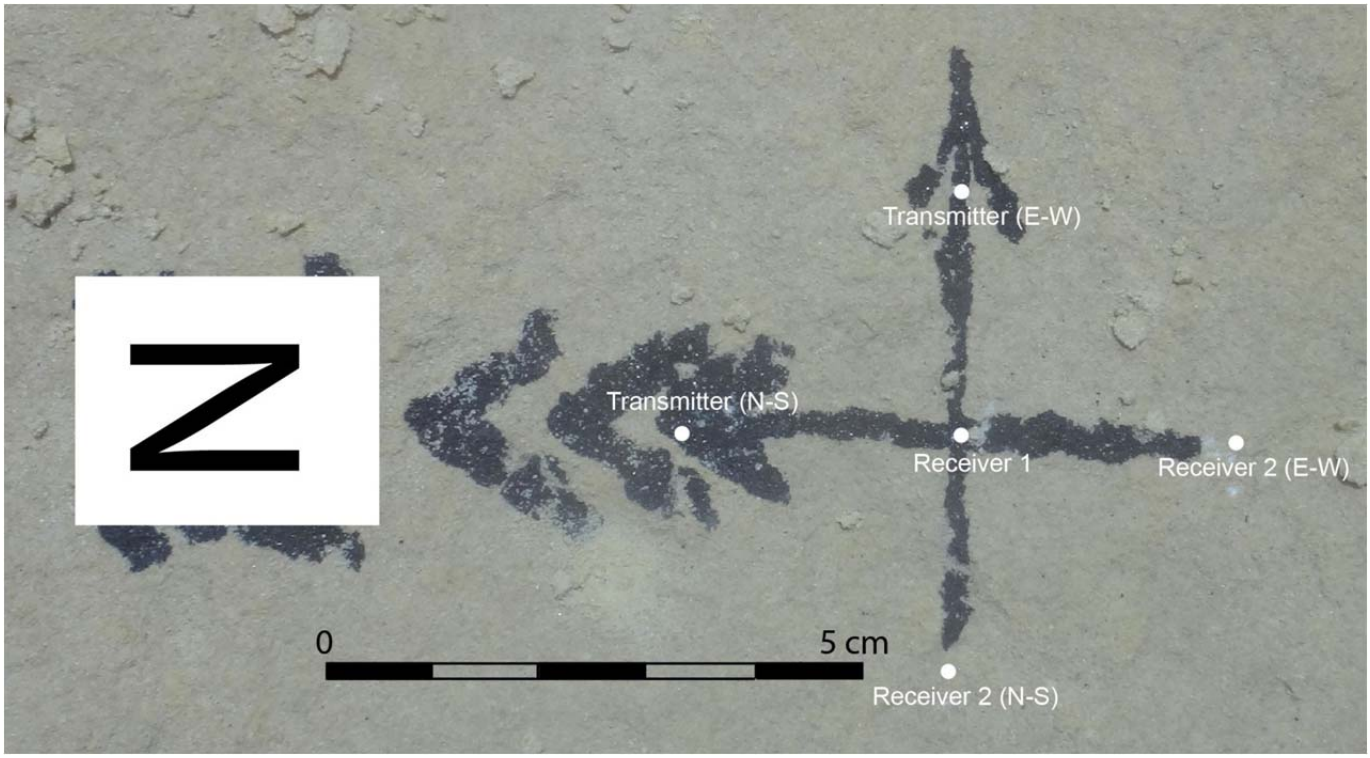

Figure B.44: Traverse 6, Station 3, Measurement 2

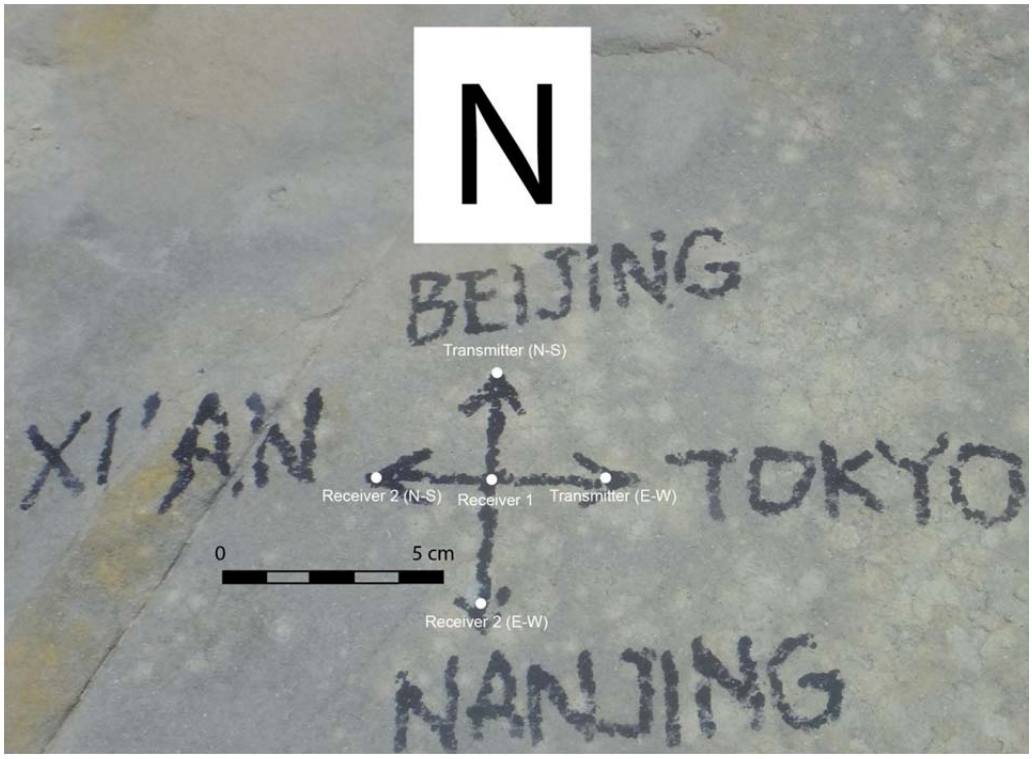

Figure B.45: Traverse 6, Station 4, Measurement 1.

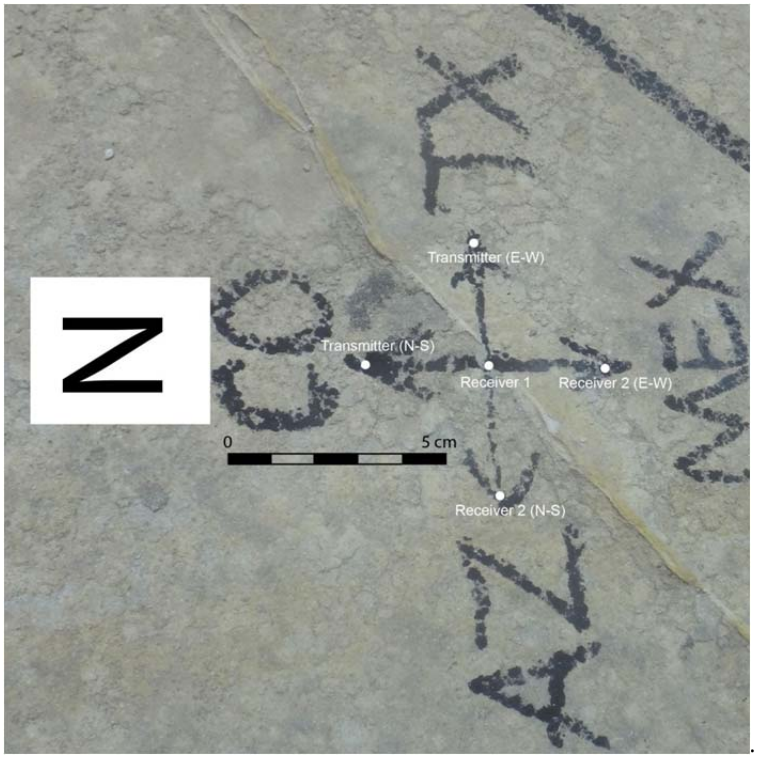

Figure B.46: Traverse 6, Station 4, Measurement 2.

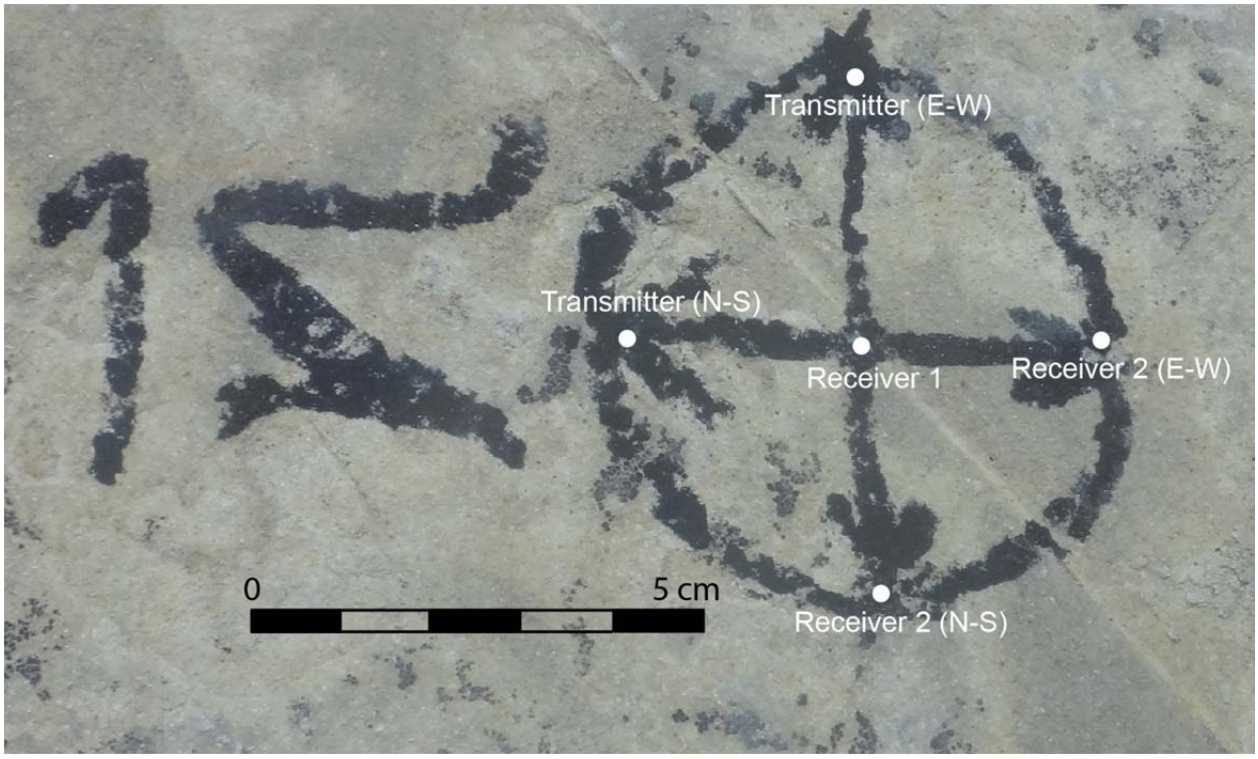

Figure B.47: Traverse 6, Station 5, Measurement 1.

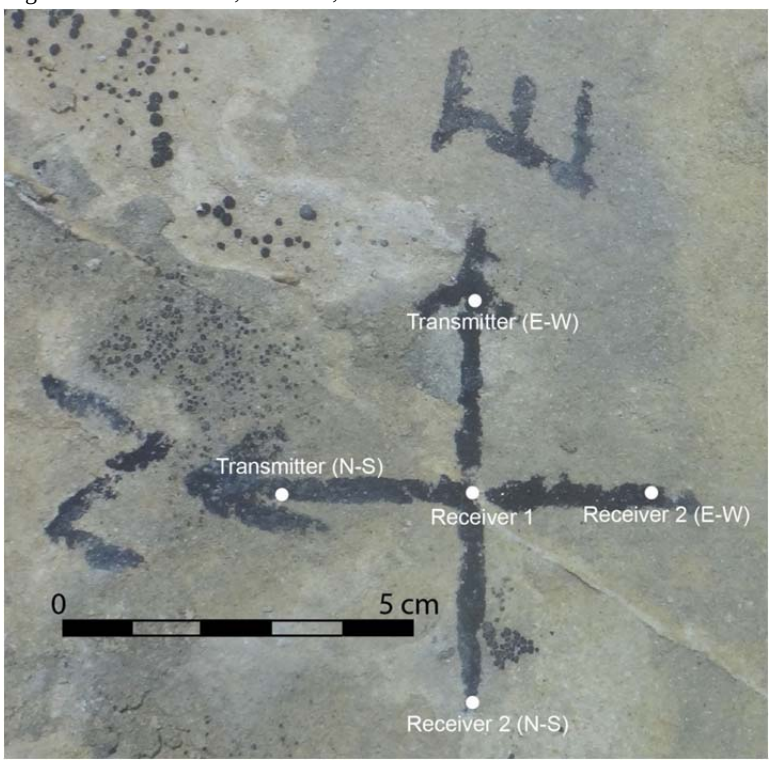

Figure B.48: Traverse 6, Station 5, Measurement 2.

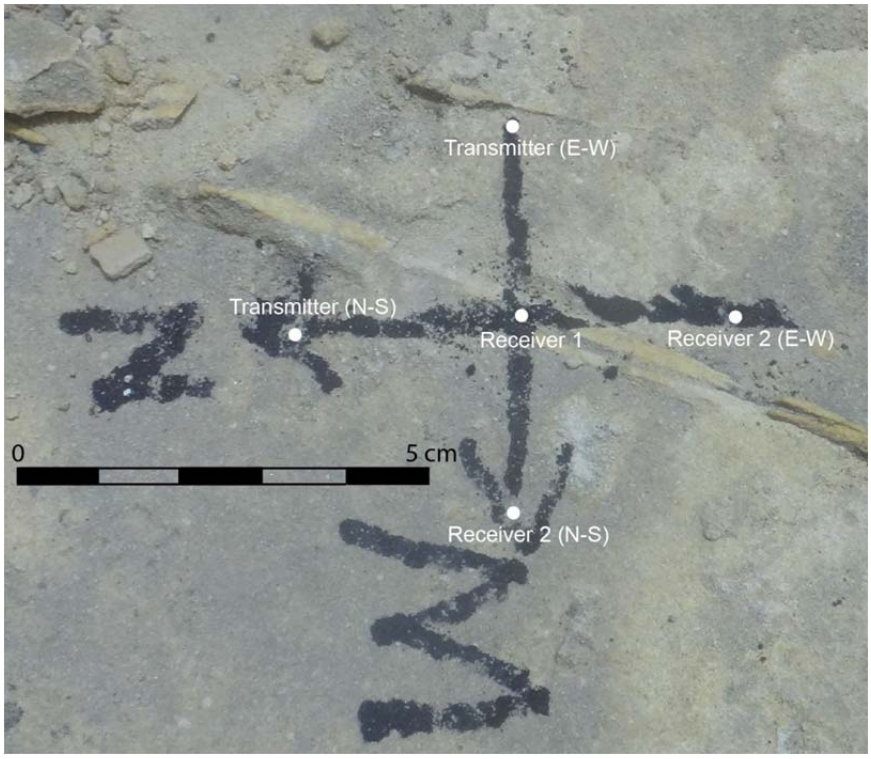

Figure B.49: Traverse 6, Station 6, Measurement 1.

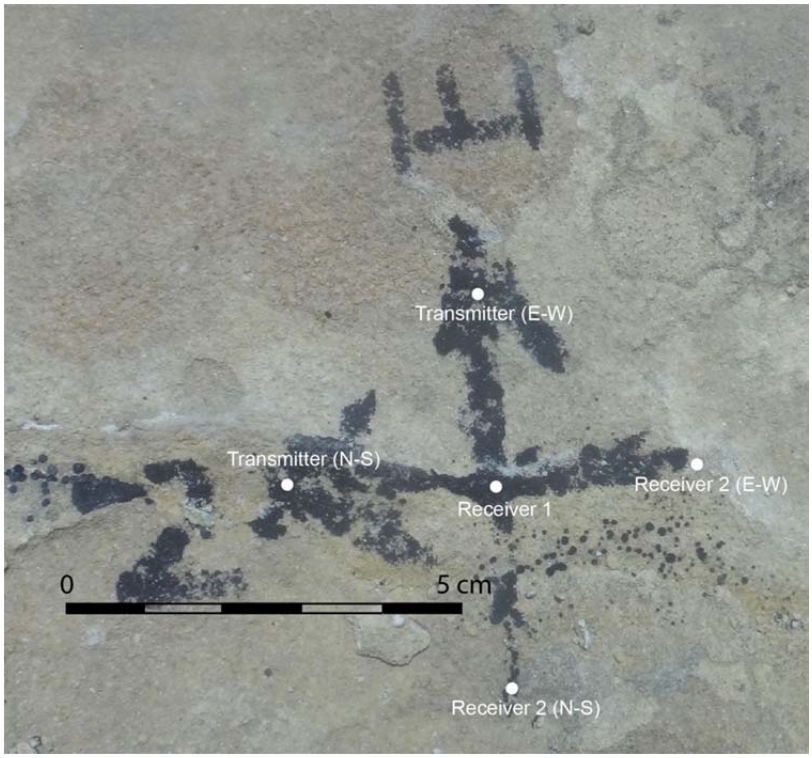

Figure B.50: Traverse 6, Station 6, Measurement 2.

Figure B.51: Traverse 6, Station 7, Measurement 1.

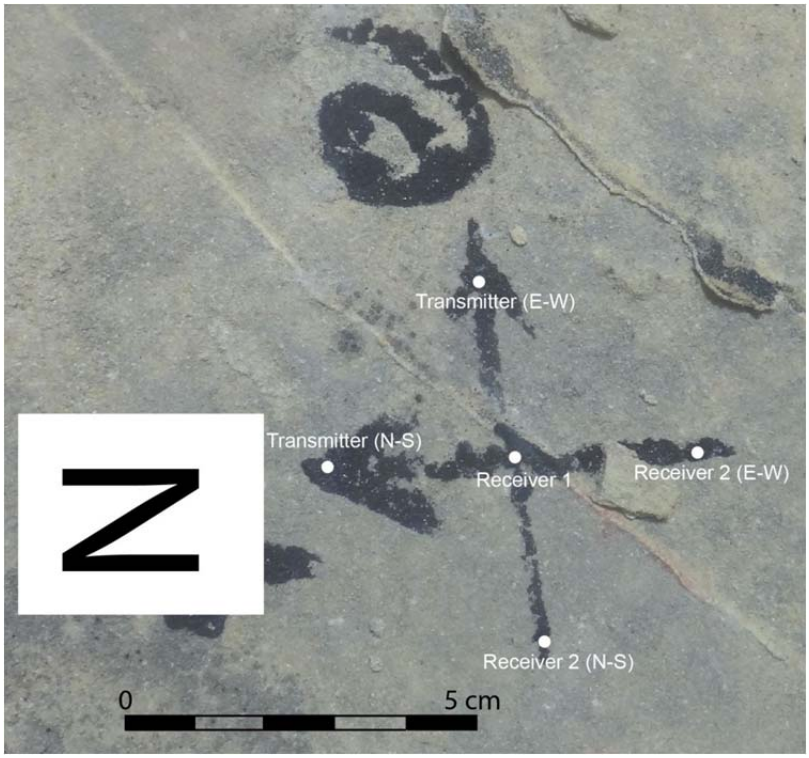

Figure B.52: Traverse 6, Station 7, Measurement 2.

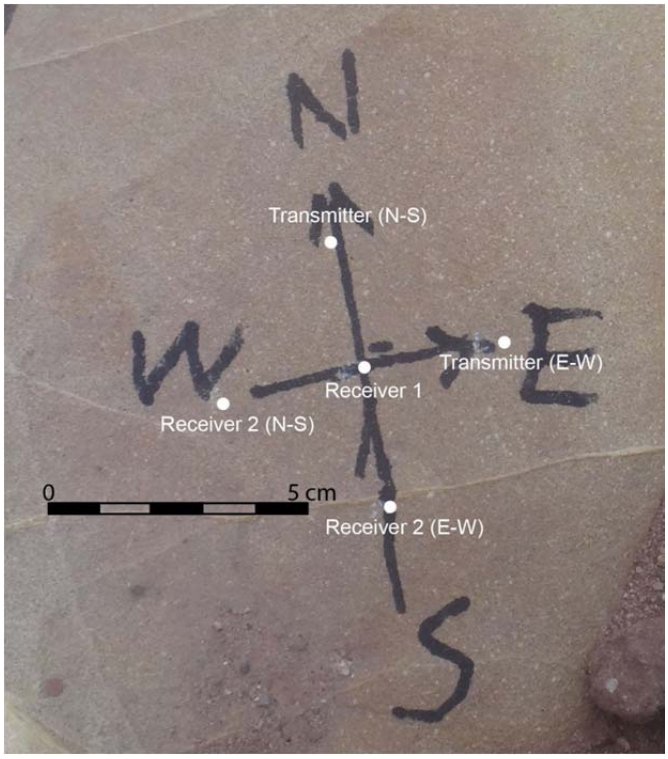

Figure B.53: Traverse 7, Station 1, Measurement 1.

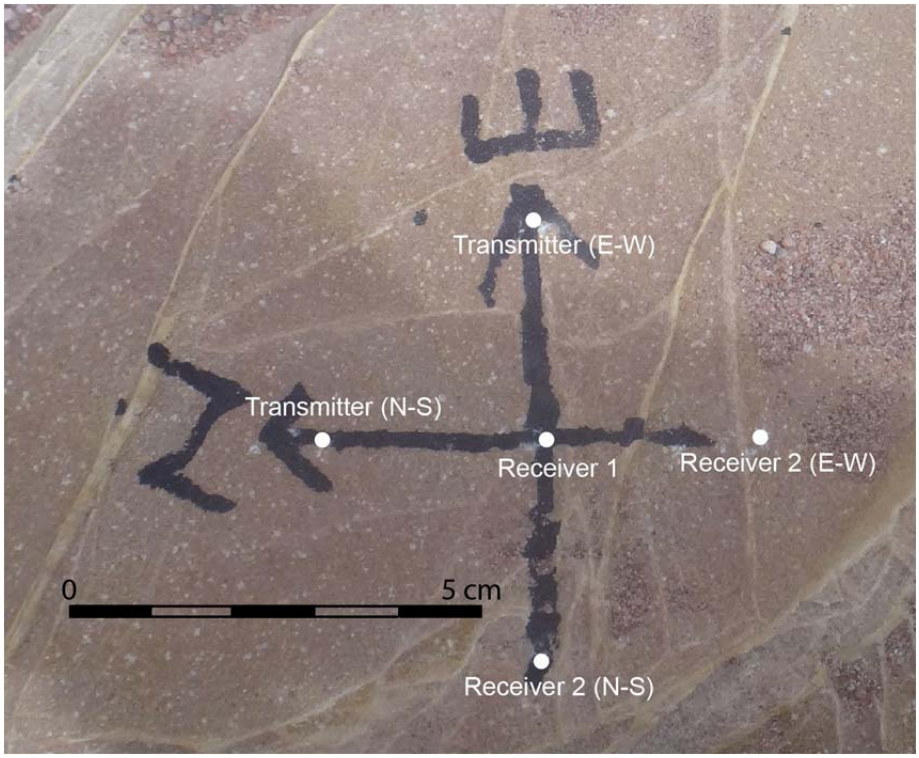

Figure B.54: Traverse 7, Station 1, Measurement 2.

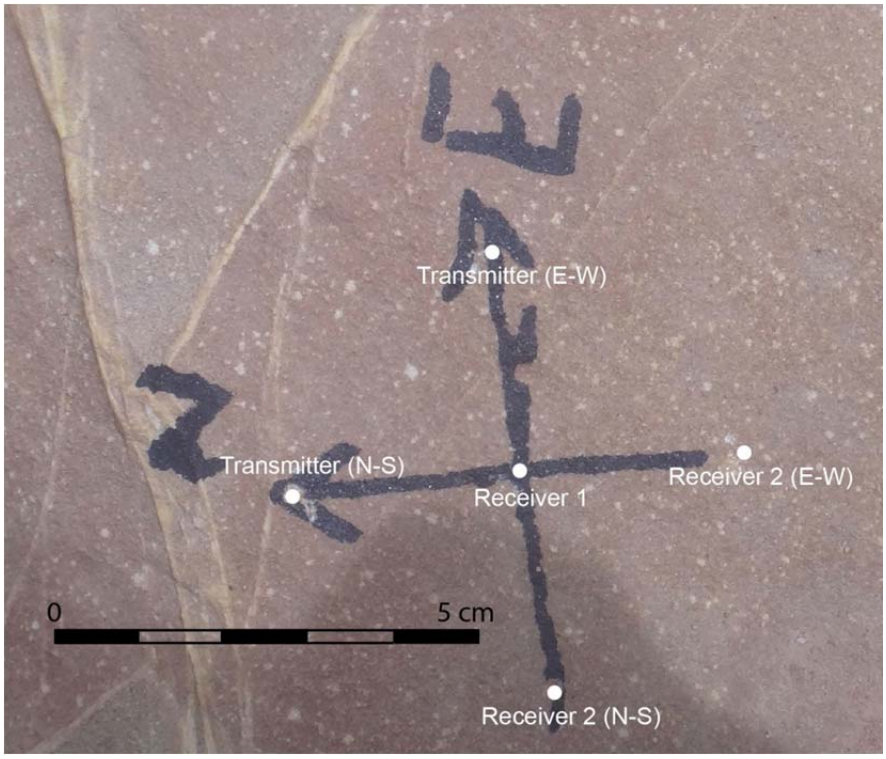

Figure B.55: Traverse 7, Station 2, Measurement 1.

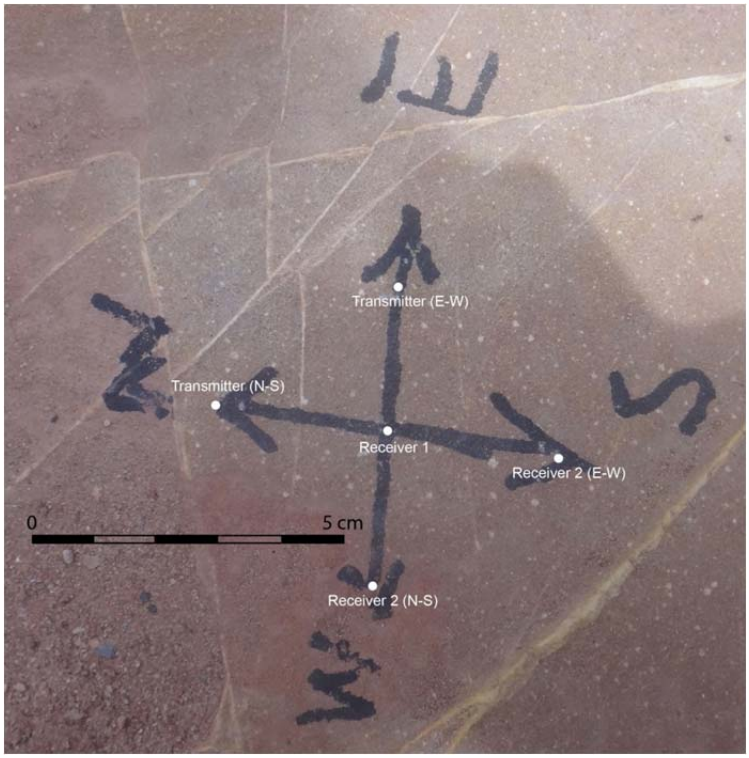

Figure B.56: Traverse 7, Station 2, Measurement 2.

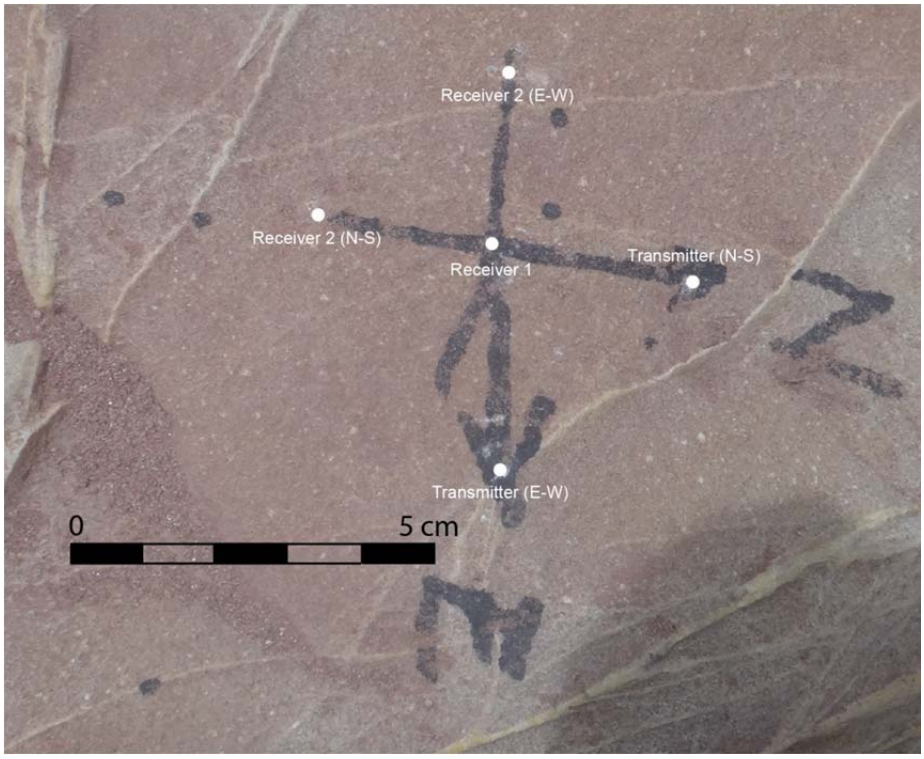

Figure B.57: Traverse 7, Station 3, Measurement 1.

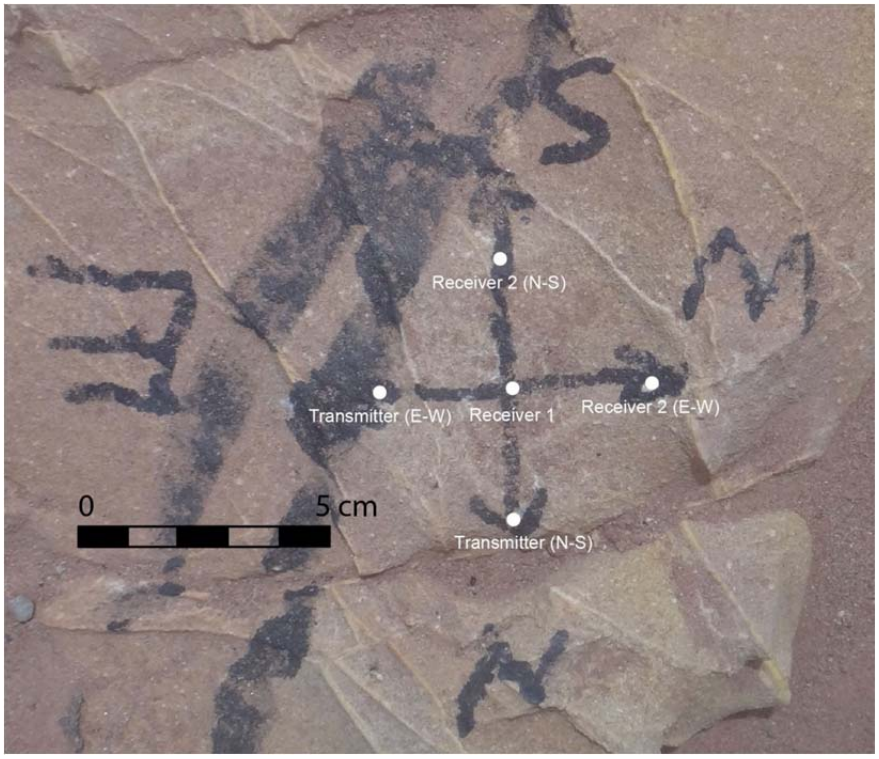

Figure B.58: Traverse 7, Station 3, Measurement 2.

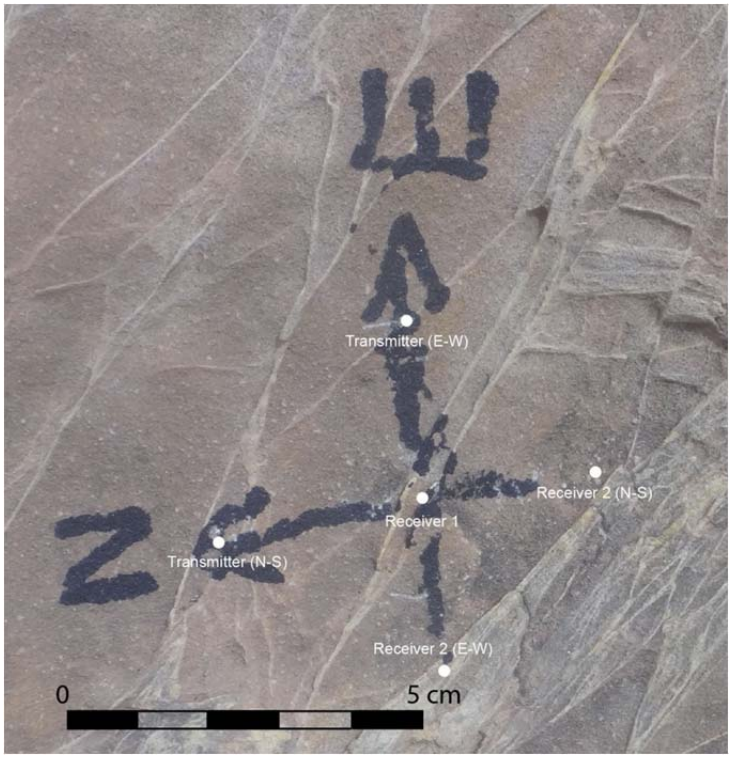

Figure B.59: Traverse 7, Station 4, Measurement 1.

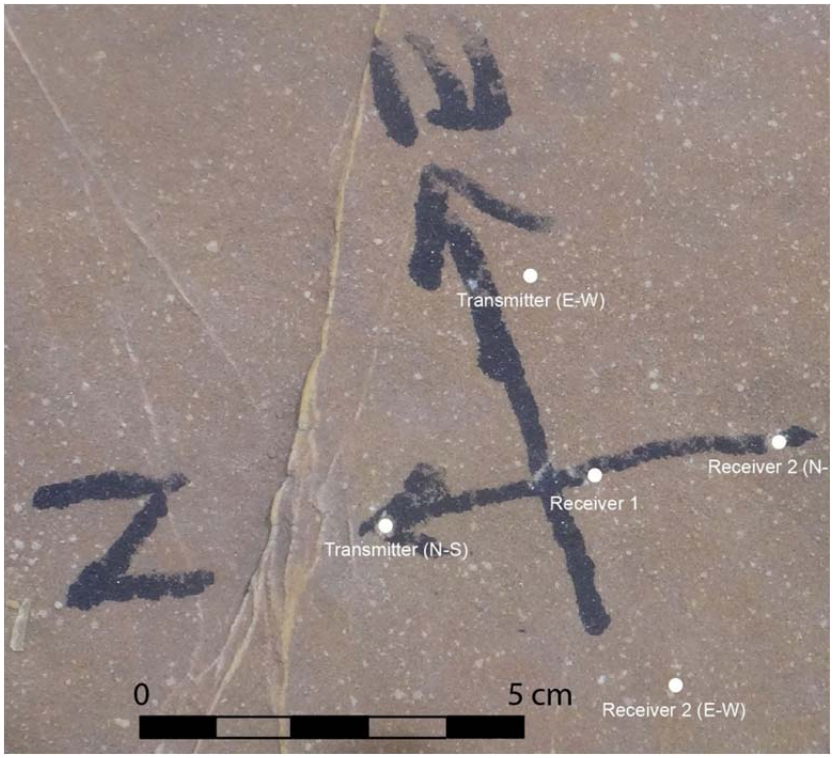

Figure B.60: Traverse 7, Station 4, Measurement 2.

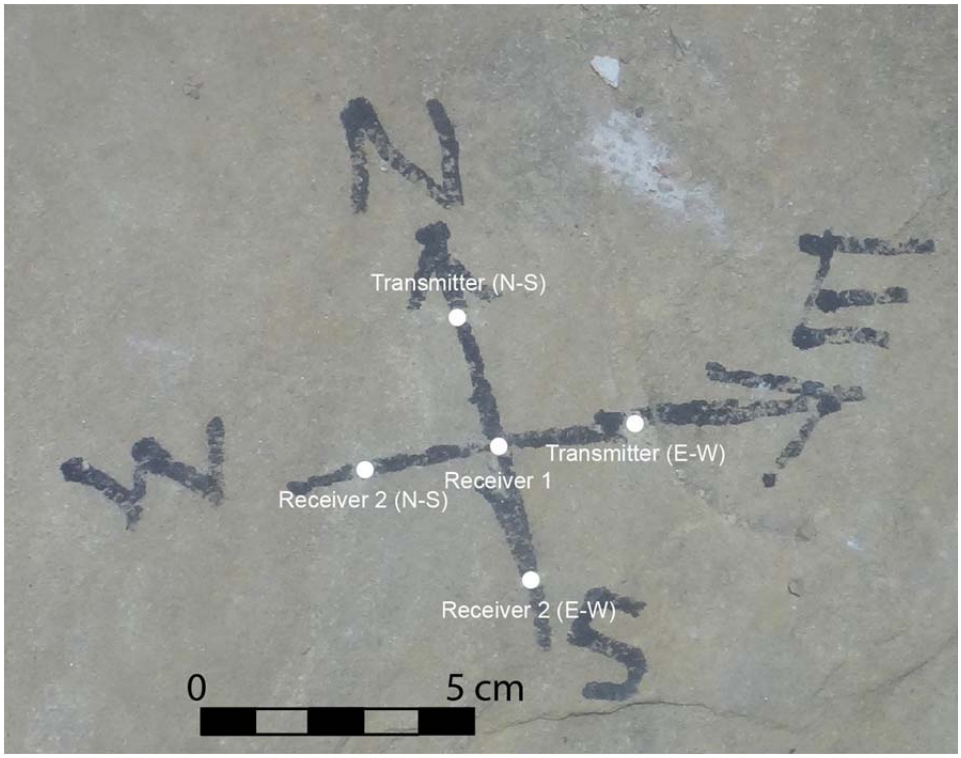

Figure B.61: Traverse 8, Station 1, Measurement 1.

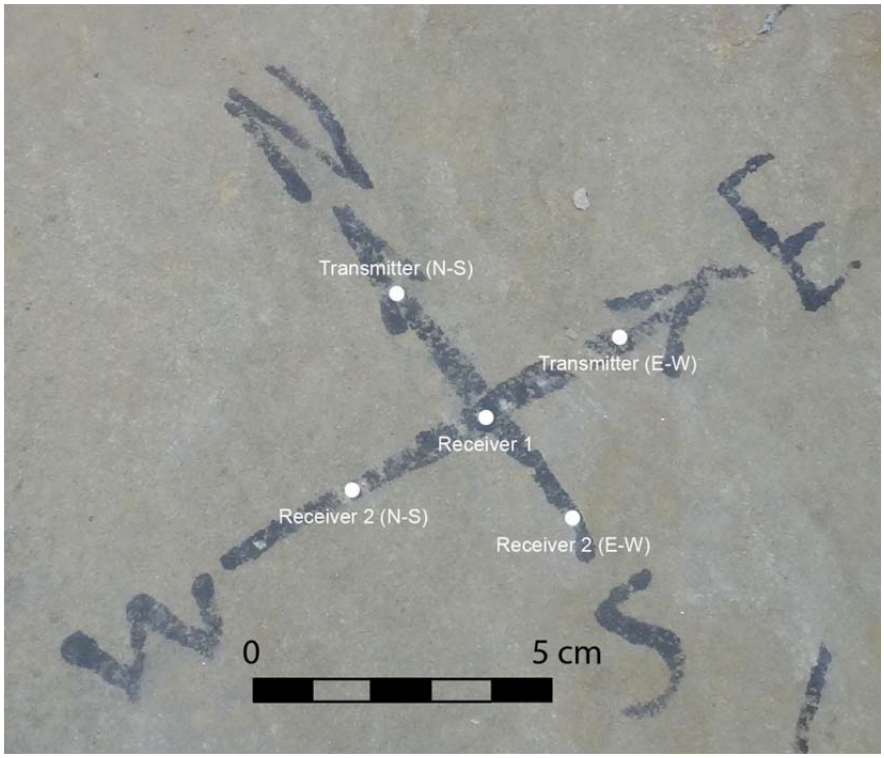

Figure B.62: Traverse 8, Station 1, Measurement 2.

Figure B.63: Traverse 8, Station 2, Measurement 1.

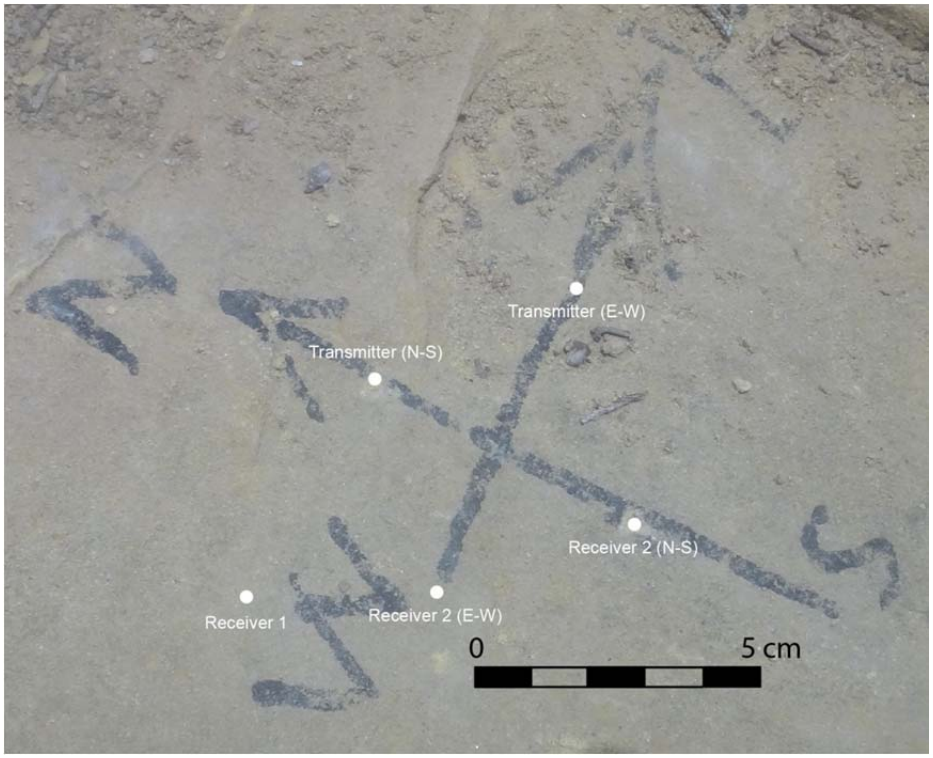

Figure B.64: Traverse 8, Station 2, Measurement 2.

Figure B.65: Traverse 8, Station 3, Measurement 1.

Figure B.66: Traverse 8, Station 3, Measurement 2.

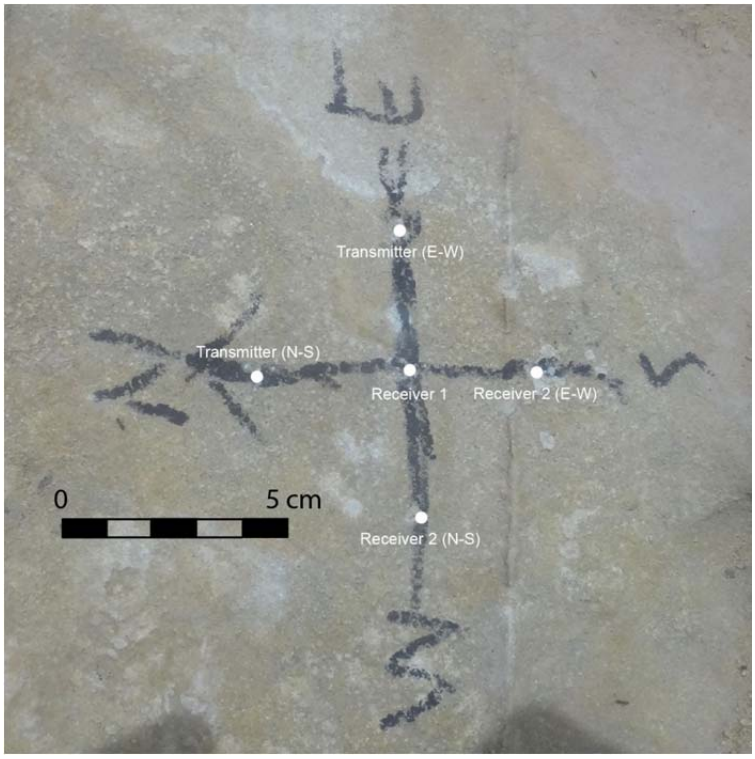

Figure B.67: Traverse 8, Station 4, Measurement 1.

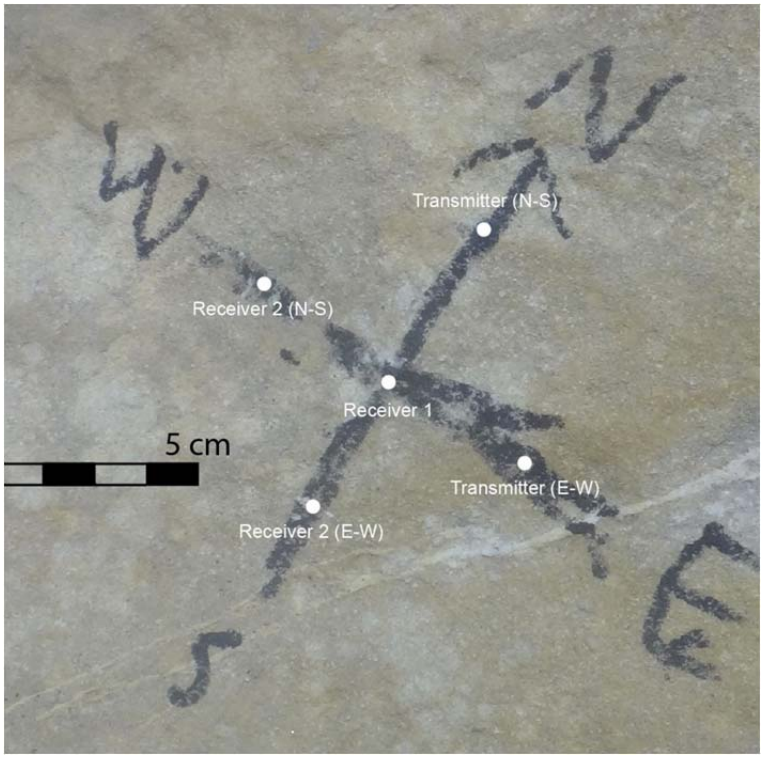

Figure B.68: Traverse 8, Station 4, Measurement 2.

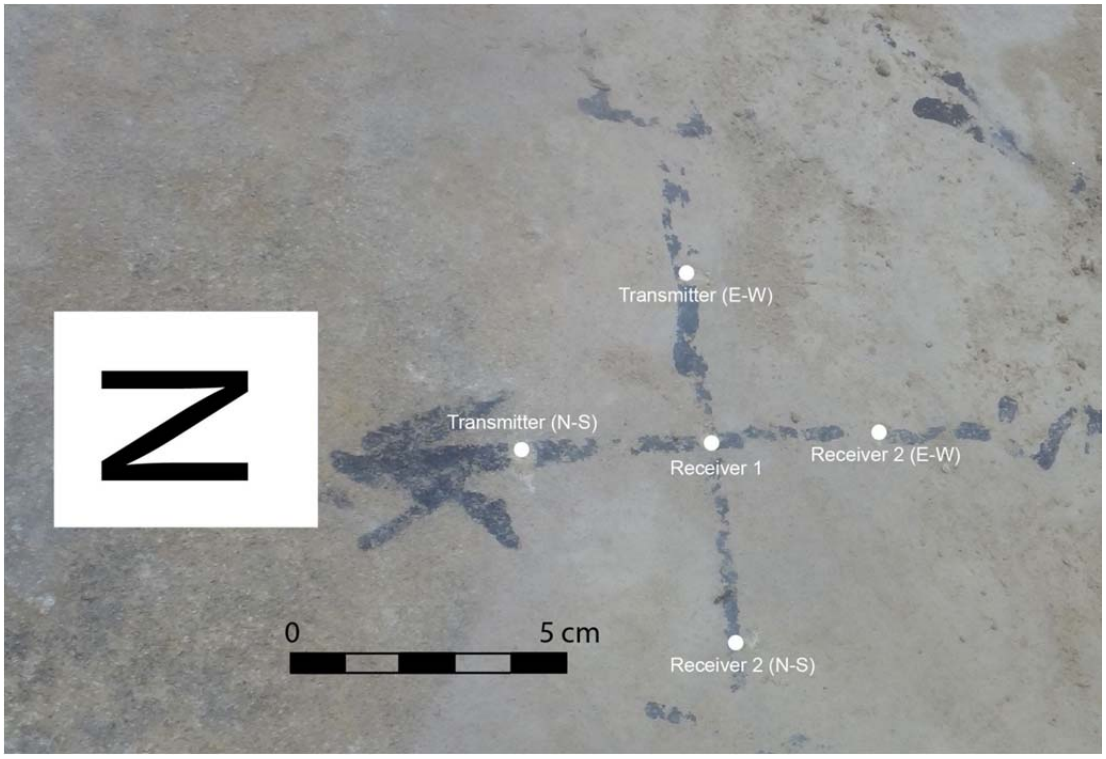

Figure B.69: Traverse 8, Station 5, Measurement 1.

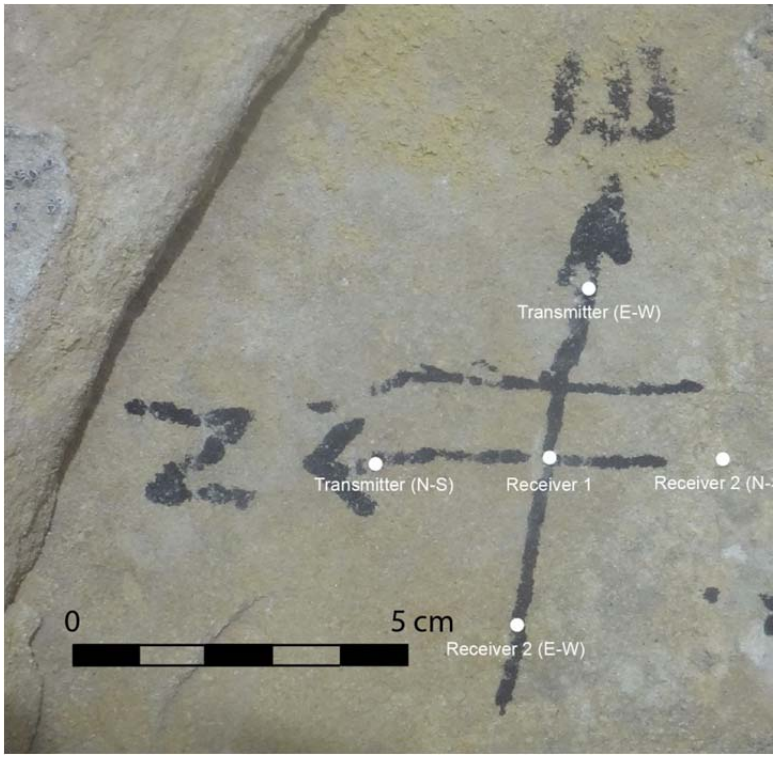

Figure B.70: Traverse 8, Station 5, Measurement 2.

C. APPENDIX: FIELD VELOCITIES AND POROSITY ESTIMATION RESULTS

Table C.1: Velocities acquired for each of the traverses.

Traverse #	Vp (N-S)m1 (m/s)	Vp (N-S)m2 (m/s)	Vp (E-W)m1 (m/s)	Vp (E-W)m2 (m/s)	Vs (N-S)m1 (m/s)	Vs (N-S)m2 (m/s)	Vs (E-W)m1 (m/s)	Vs (E-W)m2 (m/s)
1	2490	2396	2082		1460	1494	1460	1477
	2082		2048		1477	1984	1351	
	2153	2309	2016	2117	1366	1309	1380	
2	2761	2228	1984	2117	1671	1477	1323	
		2442	2153	1896	1443	1411	1443	1283
	2702	2442	2309	2153	1568	1549		1366
3	2822	2268	2540	2016	1740	1411	1716	1351
4	2702	3432	2761	3432		2228	1789	2228
	3432	2822	3528	3256	2048	1896	2228	2082
	3098		3175		2082		1896	1494
	3024	3175	3024	3175	2016	2117	2016	2048
5	2761	3342	2822	3024	1814	2117	1764	
	3528	3342		3432	2309	2190	2396	2153
	3175	3175	3175	3256	2117	2016	2082	2048
	3175	2886		2953	1868	1868	1716	1954
	2490	2396	2822	2540	1716	1588	1716	1549
	2646	2490	2886	2702	1693		1716	1814
	2352	2702	2540	2702		1868		1764
	2396	2646	2646	3175	1671	1716	1608	1814
6	2442	2352	2761	2490				
	2352	2646	2396	2822				
	2646		3024	2953		1841		1841
	2702		2822	2822	1764	1868	1789	1868
	2592	2646	2761	2702	1841	1764	1789	1693
	2953	2953	2953	2822	1868	1868	1693	1868
	2490	2442	2761	2702	1628	1649	1693	1568

Table C.2: Porosity estimations using sand diagenesis models

Traverse #	Por. Vp N-S m1 (v/v)	Por. Vs N-S m1 (v/v)	Por. Vp N-S m2 (v/v)	Por. Vs N-S m2 (v/v)	Por. Vp E-W m1 (v/v)	Por. Vs E-W m1 (v/v)	Por. Vp E-W m2 (v/v)	Por. Vs E-W m2 (v/v)
1	0.28	0.29	0.28	0.28	0.25	0.29		0.29
	0.29	0.29		0.25	0.25	0.29		
	0.29	0.29	0.28	0.30	0.25	0.29	0.25	
2	0.26	0.27	0.29	0.29	0.25	0.30	0.25	
		0.29	0.28	0.29	0.24	0.29	0.26	0.30
	0.27	0.28	0.28	0.28	0.24		0.24	0.29
3	0.26	0.27	0.29	0.29	0.22	0.27	0.25	0.29
4	0.27		0.24	0.24	0.21	0.27	0.18	0.24
	0.24	0.25	0.26	0.26	0.18	0.24	0.19	0.25
	0.25	0.25			0.19	0.26		0.28
	0.25	0.25	0.25	0.25	0.20	0.25	0.19	0.25
5	0.23	0.23	0.20	0.21	0.23	0.23	0.22	
	0.19	0.20	0.20	0.20		0.19	0.20	0.20
	0.21	0.21	0.21	0.21	0.21	0.21	0.21	0.21
	0.21	0.22	0.22	0.22		0.23	0.22	0.22
	0.24	0.23	0.25	0.24	0.23	0.23	0.24	0.25
	0.23	0.24	0.24		0.22	0.23	0.23	0.23
	0.25		0.23	0.22	0.24		0.23	0.23
	0.25	0.24	0.23	0.23	0.23	0.24	0.21	0.23
6	0.25		0.25		0.23		0.24	
	0.25		0.23		0.25		0.23	
	0.23			0.23	0.22		0.22	0.23
	0.23	0.23		0.22	0.23	0.23	0.23	0.22
	0.24	0.23	0.23	0.23	0.23	0.23	0.23	0.24
	0.22	0.22	0.22	0.22	0.22	0.24	0.23	0.22
	0.24	0.24	0.25	0.24	0.23	0.24	0.23	0.25

Table C.3: Porosity correction applied for E-W oriented measurements.

Traverse #	Por. Vs E-W m1 (v/v)	Por. Vp E-W m1 (v/v)	Por. Vp E-W m1 corrected (v/v)	Por. Vp E-W m2 (v/v)	Por. Vs E-W m2 (v/v)	Por. Vp E-W m2 corrected (v/v)
1	0.29	0.25	0.29		0.29	
	0.29	0.25	0.29			
	0.29	0.25	0.29	0.25		0.29
2	0.30	0.25	0.30	0.25		0.29
	0.29	0.24	0.29	0.26	0.30	0.30
		0.24	0.28	0.24	0.29	0.29
3	0.27	0.22	0.27	0.25	0.29	0.29
4	0.27	0.21	0.26	0.18	0.24	0.24
	0.24	0.18	0.24	0.19	0.25	0.25
	0.26	0.19	0.25		0.28	
	0.25	0.20	0.26	0.19	0.25	0.25